Mechanical Properties of the Surface of Enceladus

An experimental approach

MSc Thesis

Aïcha van Veen

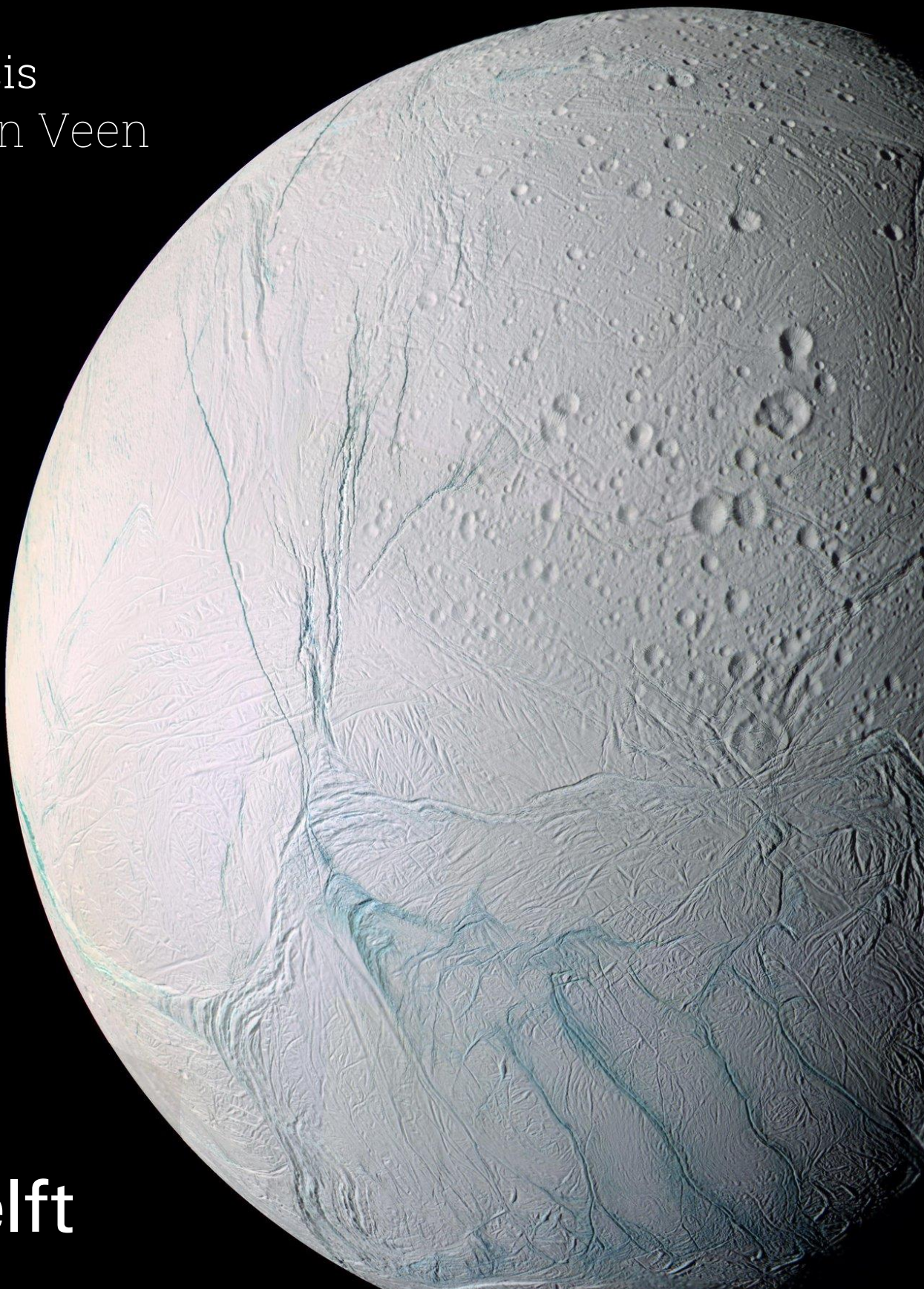

Delft University of Technology

TU Delft

This page was intentionally left blank

Mechanical Properties of the Surface of Enceladus

An experimental approach

by

Aïcha van Veen

to obtain the degree of Master of Science
at Delft University of Technology,
to be defended publicly on Monday December 15, 2025 at 10:00.

MSc:	Aerospace Engineering
Profile:	Planetary Exploration
Faculty:	Aerospace Engineering
Supervisor:	Dr. S.M. Cazaux

Cover: Image by NASA/ESA/JPL/SSI/CASSINI Imaging Team

TU Delft

This page was intentionally left blank

Abstract

This thesis investigates the mechanical strength properties of Enceladus' surface through laboratory experiments using ice analogues that simulate the moon's top layer with fine ice grains and plume deposits. Following the discoveries made by the Cassini mission, which revealed active geysers ejecting water vapour and ice particles from the South Polar Terrain (SPT), understanding the mechanical behaviour of Enceladus' surface is crucial for the design of future lander missions. The surface in the SPT is continuously modified by the plume deposits, resulting in a snow-like layer of ice grains between 20–75 μm in size, formed under low pressure, low temperature, and low gravity conditions.

To experimentally reproduce these conditions, fine ice grain analogues were produced by spraying water into a liquid nitrogen dewar, creating ice grains up to 250 μm. These grains were sieved and stored in –25 °C and –80 °C freezers to study the effects of temperature and freezer time on their strength. The analogues were then tested under both atmospheric and vacuum pressures (down to 0.1 mbar) to simulate the near-vacuum conditions present on Enceladus' surface. The mechanical strength of the ice analogues was determined using the self-developed and validated CONE method, which is based on existing cone penetration and indentation methods. This technique allowed for both shear and compressive strength to be derived from the same experimental setup.

In atmospheric pressure, shear strengths between 20–220 kPa and compressive strengths between 40–475 kPa were measured, depending on the freezer time and temperature of the samples. The results showed a clear trend: longer freezer times and warmer storage temperatures led to stronger analogues, confirming that sintering between the ice grains significantly increases both shear and compressive strength over time. The sintering process was observed to occur much faster in the –25 °C samples, reaching stage 1 sintering within a maximum of 4.5 hours, whereas at –80 °C it would take hundreds of days, well beyond the timescale of this study. Under vacuum conditions, however, the strengthening effect of sintering was largely suppressed. Both shear and compressive strengths were consistently around 10 kPa, nearly independent of origin temperature or freezer time. This reduction is attributed to sublimation, which increased the porosity of the analogues and caused partial reorganisation of the surface microstructure as the ice moved toward its equilibrium temperature. While the overall strength remained weak, a small difference persisted between the two origin temperatures, with the –25 °C analogues still slightly stronger and showing brittle failure after sufficient sintering. The –80 °C analogues, in contrast, remained more ductile even after an extended freezer time. This indicates that although vacuum conditions limit sintering, the microstructural state of the ice grains still influences its mechanical behaviour.

By translating these laboratory results to Enceladus' conditions, this study concludes that the moon's surface in the SPT is likely characterised by a weak, unconsolidated, snow-like top layer formed by constant plume deposition, underlain by a partially sintered and brittle ice layer in the warmer regions near the tiger stripes. The upper layer likely remains mechanically weak due to ongoing sublimation and continuous grain deposition, preventing significant sintering. These findings have direct implications for future lander missions. A lander is expected to encounter a weak and unconsolidated surface capable of localised failure under concentrated loads. Therefore, a distributed footpad design and shock-absorbing landing system are recommended to minimise surface stress. Additionally, sampling systems should also use low-force or thermal techniques to collect and seal material quickly, minimising potential sublimation losses and preserving sample integrity.

Overall, this thesis provides new experimental insights into the mechanical properties of fine ice grain samples under both atmospheric and near-vacuum conditions, filling an existing knowledge gap in the study of Enceladus' surface strength. The results support the conclusion that Enceladus' surface is mechanically weak but structurally complex, with strength and failure behaviour strongly influenced by sintering, temperature, and pressure. These are therefore critical factors to consider in the design and operation of future lander missions to Enceladus and other icy moons.

This page was intentionally left blank

Preface

After several months of playing around with ice grains in the lab, this work finally marks the end of my master's degree. It also marks the end of my time as a student, and I have to say that this is the best project to end that time with. I had an absolute amazing time researching Enceladus and its surface through the many ice analogues I produced. I hope that my results from this time will aid others in further understanding Enceladus' icy surface and that they may be inspired by my results.

Of course, this work could not have been done without the support, in many different forms, of the people around me. First of all, my biggest thank you goes out to my supervisor Stéphanie. You have made this project an educational and very fun time for me with our lovely weekly meetings, random other encounters, and Solar System necklace making. Thank you for the great support and supervision. I would also like to thank everyone else who helped with the technicalities of my work: Yaël, thank you for always helping me out when I had questions about PISCES or LabVIEW, and thank you to all the wonderful technicians of the Aircraft Hall, but especially to Mascha, Johan, Ramon, and Alexander for helping me with any problem or question.

I would also like to thank all my friends and family. Thank you to my parents, sister, and the rest of my family, who I know are very proud of me. Thank you Kristie, for being the best friend one could dream of, and thank you Jasmine, for being an amazing friend and the many fun 'working' and 'running' sessions together. Thank you to my long-lasting uni friends Filippo, Zach, Roosa, and Timo for all the fun times from the bachelor's all the way to the master's, and now after. Thank you Momo, Robbin, Markus, and Flavio, for all the tea sessions that were the perfect procrastination breaks. Thank you to my friends from my student communication job, especially Ana, for the fun additional adventures next to the master's programme. And last, but most definitely not least, thank you Quirijn. Thank you for always being there for me. From lending me your soup spoon to use for my ice grain production to being my fake supervisor over summer when the faculty was on holiday; you are my world.

Thank you to everyone who has helped me come so far, and thank you to everyone reading this work.

Aïcha van Veen
Delft, November 2025

Contents

List of Figures

List of Tables

Nomenclature

List of Abbreviations

Abbreviation	Definition
LN_2	Liquid Nitrogen
CDA	Cosmic Dust Analyser
CIRS	Composite Infrared Spectrometer
CONE	Manually Constructed Fall-Cone Device
INMS	Ion and Neutral Mass Spectrometer
ISS	Imaging Science Subsystem
RADAR	Radio Detection and Ranging
RPWS	Radio and Plasma Wave Spectrometer
RSS	Radio Science Subsystem
SPT	South Polar Terrain
UV	Ultraviolet
UVIS	Ultraviolet Imaging Spectograph
VIMS	Visible Infrared Mapping Spectrometer

List of Chemical Compounds

Abbreviation	Definition
N_2	Nitrogen
C_2H_2	Acetylene
C_3H_8	Propane
Ca	Calcium
CH_3OH	Methanol
CH_4	Methane
Cl	Chloride
CO	Carbon monoxide
CO_3	Carbonate
CO_2	Carbon dioxide
CsI	Cesium iodide
Fe	Iron
H_2	Hydrogen
H_2O	Water
H_2O^+	Oxoniumyl
H_3O^+	Hydronium
H_2S	Hydrogen sulfide
HCN	Hydrogen cyanide
LN_2	Liquid Nitrogen
Mg_2SiO_4	Forsterite
Na	Sodium
N_2	Nitrogen
NH_3	Ammonia
Mg	Magnesium
$MgSiO_3$	Enstatite

Abbreviation	Definition
Si	Silicon

List of Symbols

Symbol	Definition	Unit
a	Radius of contact at indentation depth	[m]
a	Neck radius	[m]
a_0	Initial contact radius	[m]
A	Surface area	[m^2]
c	Cohesion	[Pa]
d	Stopping distance	[m]
d_p	Penetration depth	[m]
D	Diameter	[m]
E_{kin}	Kinetic energy	[J]
f	Sintering power law parameter	[yr]
F	Force	[N]
g	Gravity	[m/s^2]
g	Sintering power law parameter	[-]
H / h	Height	[m]
J	Sublimation rate	[kg/m^2s]]
k_b	Boltzmann constant	[J/K]
K_{Kang}	Sintering rate constant	[m^3s^{-1}]
K_{vap}	Sintering rate constant	[m^3s^{-1}]
L	Latent heat of the phase change	[$J \cdot mol^{-1}$]
m	Mass	[kg]
M	Molar weight	[g/mol]
p	Pressure	[Pa]
p_{atm}	Atmospheric pressure	[Pa]
p_{vac}	Vacuum pressure	[Pa]
R	Universial gas constant	[$Jmol^{-1}K^{-1}$]
t	Time	[s]
t_f	Freezer time	[s]
t_s	Sintering timescale	[yr]
T	Temperature	[K]
T	Torque	[Nm]
T_{origin}	Origin temperature	[K]
$\overline{v}$	Mean velocity of vapour molecules	[m/s]
v_0	Launching speed [m/s]	
V_m	Molar volume	[m^3/mol]
W	Work	[J]
x	Neck radius	[m]
α	Cone angle	[°]
α	Sublimation coefficient	[-]
γ_s	Surface energy	[J/m^s]
ΔV	Change in specific volume	[$m^3 \cdot mol^{-1}$]
ΔM	Sublimated mass	[kg]
σ	Stress	[Pa]
σ_c	Compressive strength	[Pa]
τ	Shear strength	[Pa]
φ	Internal friction angle	[°]

1 Introduction

Enceladus, one of Saturn's icy moons, is an exciting target for scientific research. After the Cassini mission discovered that Enceladus spews water vapour and ice particles into space through its active geysers, the icy moon became a key point of interest for understanding some of the elements required for life on other planetary bodies in our Solar System Spilker, 2019. Adding more fly-by's of Cassini by Enceladus led to measurements that indicate a global subsurface ocean and geologically active area around its south pole terrain as well with four large fractures called the tiger stripes where the geysers originate (Spencer et al., 2006, Porco et al., 2006). These features combined make Enceladus a hot spot for space exploration research.

While a lot of work is done to better understand Enceladus' features using Cassini's data, many aspects still remain uncertain. To truly learn about Enceladus' subsurface ocean, crevasses, surface, and plume it is necessary to send a lander mission to Enceladus for which early plans are in the making (Helbert et al., 2025). In order to do that however, it is necessary to understand what to expect on Enceladus' surface in terms of mechanical strength properties and what this means for the design of lander mission. Enceladus' plume especially adds to the complexity of understanding the mechanical properties of its surface as plume deposits fall back creating a snow-like top layer (Martin et al., 2023). Together with the low pressure, low temperature, and low gravity environment of Enceladus, this creates quite a challenge to experimentally study the surface's strength.

Nevertheless, over the last years such experimental studies have started to come up. While most of these studies focus on one specific topic such as sintering (Gundlach et al., 2018, Molaro et al., 2019) or the adhesive strength of ice grains (Gundlach et al., 2011, Gundlach and Blum, 2014, Musiolik and Wurm, 2019), one study did look at at the compressive strength of fine ice grain samples. Choukroun et al. (2020) focused on the impact of sintering time on the compressive strength of bulk ice grain analogues. There are two aspects that have not been considered thus far in these experimental studies for Enceladus' surface: the shear strength of ice grain analogues and, more importantly, strength testing in a near-vacuum environment like on Enceladus. This work aims to resolve this knowledge gap by studying the compressive and shear strength of fine ice grain analogues in both atmospheric and vacuum pressure.

1.1. Research Questions

The research objective of this thesis is to study the mechanical properties of Enceladus' surface in a laboratory environment for the purpose of future landing missions. To do so, the following main research question is set up:

What are the mechanical properties of Enceladus' surface for the purpose of future landing missions studied through ice analogues?

This main research question is split up again into three research questions, which each have two sub-research questions as well:

1. How can Enceladus' surface be recreated in a laboratory?

   (a) What are the characteristics of Enceladus' environment and icy crust?
   (b) How can the ice analogues be made to resemble Enceladus' surface in terms of grain size, temperature, and pressure?

2. What are the mechanical strength properties of Enceladus' surface?

   (a) What is the shear and compressive strength of the surface analogues?
   (b) What is the effect of freezer time, pressure, and origin temperature on the strength of the ice analogues?

3. How does the strength of Enceladus' surface impact future landing missions?

   (a) How can the mechanical strength of the ice analogues be related to Enceladus' surface?
   (b) What does the strength of Enceladus' ice analogues imply for landing possibilities?

To address these questions, both a literature study and experimental work were done. Through the production of fine ice grains, the strength of ice analogues is tested under different pressure and temperature environments. The results from the experimental work are then related to the surface of Enceladus in order to understand better both what to expect upon arriving there as well as how to design the lander missions themselves.

1.2. Thesis Outline

The work in this thesis is described in eight chapters with this introduction being the first. Chapter 2 gives relevant scientific background knowledge about Enceladus, ice characteristics, ice sintering, strength testing, and a more detailed knowledge are given. This is followed by a description of the experimental set-up in Chapter 3 including the test method. This test method is then verified in Chapter 4 before diving into Chapter 5 where the mechanical properties of the ice analogues are given. These are the results of the analogue strength tests including an interpretation of those results as well. A discussion chapter follows in Chapter 6 where first the properties of the ice analogues are translated to Enceladus' surface before its implications for lander missions are given. The conclusion, answering the research questions stated in the prior section, is then given in Chapter 7. The final chapter is then Chapter 8 indicating the limitations of the experimental set-up and the recommendations for future work.

2

Scientific Background

In this chapter, relevant scientific background regarding the study of *'Mechanical Properties of the Surface of Enceladus'* is described. This starts off with a section on Enceladus in general, Section 2.1 *'Characteristics of Enceladus'*, describing its features and interesting characteristics. This is followed by Section 2.2 *'Ice Characteristics'* elaborating on the characteristics of ice and ice grains and Section 2.3 *'Sintering'*, which describes a specific process that can occur between ice grains. After describing all the ice characteristics, the scientific background continues with Section 2.4 *'Strength Testing for Granular Surfaces'*, which describes relevant strength parameters, methods to measure the strength of granular surfaces, and how to calculate them. This chapter is concluded with a knowledge gap in Section 2.5 *'Knowledge Gap'*.

2.1. Characteristics of Enceladus

Enceladus is an icy moon orbiting Saturn, on which intriguing features were discovered during the Cassini mission. Despite its small size with a diameter of 504 km, Enceladus stands out due to geysers erupting from its south pole terrain, spewing water vapor, ice particles, and other chemical compounds into space. The plume coming from Enceladus' surface and the subsurface ocean beneath its icy crust have become focal points for scientific exploration as the moon has these very unique features. These features: the icy crust, interior properties, and the plume are described here in further detail.

2.1.1. Icy Crust

The icy crust of Enceladus entails its outer surface layer, which has four fractures named 'tiger stripes' on its surface in the southern hemisphere. These tiger stripes, and Enceladus' general topography, gravity, and temperature are described in this section.

Tiger Stripes

Through the images taken by Casini's Imaging Science Subsystem (ISS), unique geological formations were discovered in the south polar terrain (SPT) of Enceladus in the form of four parallel cracked features, which are visualised in Figure 2.1. These fissures, informally named 'tiger stripes' are spaced 35 km apart and are about 130 km long each, 2 km wide, and 500 meters deep (Spencer et al., 2006). From left to right, the fractures in Figure 2.1 are named Damascus Sulcus, Baghdad Sulcus, Cairo Sulcus, and Alexandria Sulcus. In addition to that discovery, the ISS images showed visual evidence of geyser jets, consisting of fine particles, spreading from the tiger stripes region, resulting in the large plume over the moon's south pole (Porco et al., 2006). During the ninth flyby of Enceladus in November 2009, Cassini approached Enceladus' surface at a distance of 1,600 km with a speed of 7.7 km/s, allowing the ISS to take high-resolution images of the tiger stripes. Figure 2.2 clearly shows the ridges of the Baghdad Sulcus and the texture of the surface around it at a resolution of 12 to 30 meters. This image was produced using the ISS images and topographic map created by P. Schenk [1].

[1] https://science.nasa.gov/missions/cassini/enceladus-flyby-nov-21-2009/
[3] https://science.nasa.gov/missions/cassini/enceladus-flyby-nov-21-2009/

Figure 2.1: ISS Image of the Tiger Stripe Fractures [2]

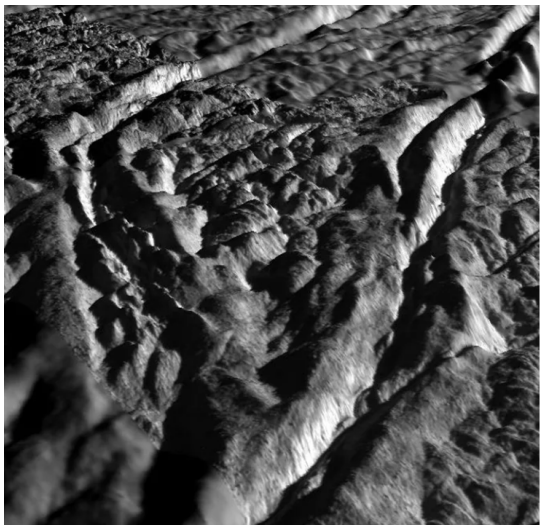

Figure 2.2: Close-up image of the Baghdad Sulcus [3]

The tiger stripes region showed elevated temperatures in comparison to its surrounding surface as Cassini's Composite Infrared Spectrometer (CIRS) measurements indicated high thermal emission of temperatures up to 200 K in the tiger stripe fractures (Spencer et al., 2006). Some mineralogical properties of Enceladus' surface around the tiger stripes could be identified as well through Cassini's Visible Infrared Mapping Spectrometer (VIMS) data, indicating the presence of water-ice, free and trapped CO_2, and light organics suggesting the presence of NH_3 or NH_3 hydrate (Brown et al., 2006). Nevertheless, the formation of the tiger stripes remains uncertain as its appearance suggests tectonic fractures, while its internal heat and emanating plume suggest fissures in the moon's lithosphere (Porco et al., 2006). Although, the origin of these tiger stripe fractures still remain uncertain, different theories for its formation are considered. Rhoden et al. (2020), theorise that the formation of the tiger stripes is due to eccentricity-driven tidal stresses, indicating that the tides are responsible for the erupting jets as well. While Yin and Pappalardo (2015) agree that the tidal stress may cause the flux in the jets, they theorise that the tiger stripes were formed due to a release of gravitational potential energy after transient thermal events weakened Enceladus' icy surface.

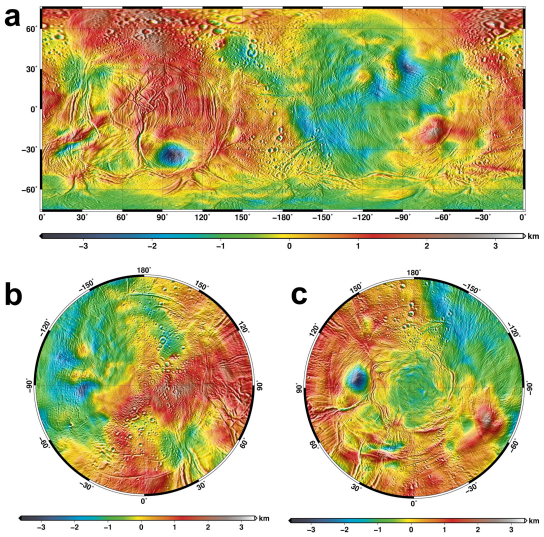

Figure 2.3: Enceladus' topography as modeled by Park et al. (2024) showing a) the cylindrical projection, b) the northern hemisphere, and c) the southern hemisphere

Topography, Gravity, and Temperature

From Cassini's measurements, the topography, temperature, and gravity of Enceladus could be mapped, each providing valuable information regarding Enceladus' interior and surface characteristics. Using Cassini's Radio Science Subsystem (RSS) and imaging data, Park et al. (2024) were able to map the topography of Enceladus as shown in Figure 2.3. This map indicates the height of Enceladus' surface relative to the (256.14, 251.16, 248.68)-km best-fit ellipsoid at a range between -3.6 and 3.4 km. An intriguing observation is that while the northern hemisphere has many crater impacts, the SPT is almost free of these impacts, indicating the occurrence of resurfacing events and a geologically young surface in the SPT (Spencer et al., 2009). Analysing the thickness and structure of the ice shell is important to understand Enceladus' formation, evolution, and activity. Based on maps like the topography presented in Figure 2.3 and gravity shown in Figure 2.4, interior properties of Enceladus can be better understood, which is described in more detail later in this chapter.

From the RSS data, Iess et al. (2014) were able to determine the moon's quadrupole gravity field as well as the degree-3 zonal harmonic coefficient J_3. To obtain a model of Enceladus' gravity field, shown in Figure 2.4, the data of three flybys was used and neutral particle drag was incorporated to ensure a 'faithful gravity solution' (Iess et al., 2014). The graph shows the gravity field of Enceladus mapped onto a reference ellipsoid from -2.5 mGal in dark blue to 2.5 mGal in dark red. The estimated J_3 value of $-115.3 \pm 22.9 \cdot 10^6$ suggests a negative gravity anomaly of 2.5 mGal, which is visualised in Figure 2.4 (Iess et al., 2014). This gravity anomaly corresponds with Enceladus' hot spot in the SPT. Another observation that can be made from Figure 2.4 is the almost opposite gravity between the northern and southern hemisphere of Enceladus. These gravity anomalies suggest that the mass distribution is not uniform, which could be due to differences in the thickness of the ice crust or variations in the density of materials beneath the surface.

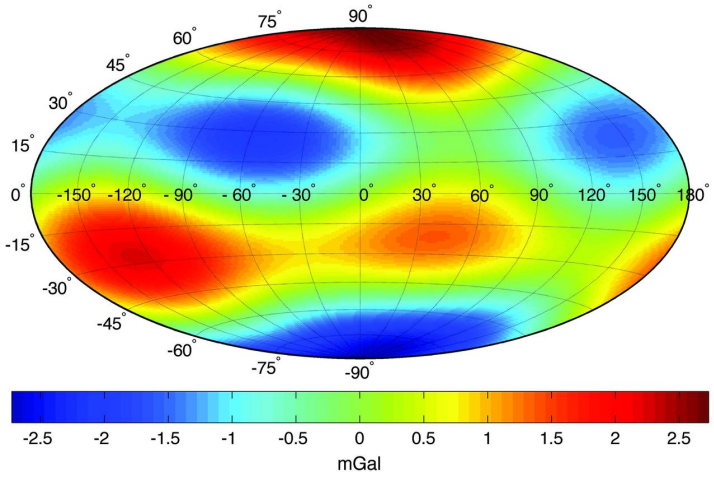

Figure 2.4: Enceladus' Gravity Field as Modeled by Iess et al. (2014)

The CIRS provided valuable data on Enceladus' surface temperature by conducting thermal mapping of the moon's surface. This showed great differences between the predicted and observed temperatures of the moon, as depicted in Figure 2.5, by Newman et al. (2008). Enceladus' high albedo, or reflectivity, of 0.85 suggested a cooler surface of the moon than predicted, but through the CIRS data, a high temperature was observed in the south pole region. The CIRS measured a 3-7 GWatt thermal emission from the southern region of the moon with temperatures between 114 and 157K (Spencer et al., 2006; Porco et al., 2006). The surface temperatures within the tiger stripe fractures are even higher at 180-200K (Spencer et al., 2009). This is significantly higher than the surface temperature outside of the tiger stripes, which is below 100K, and outside of the SPT, which is between 50 and 80K (Spencer et al., 2006; Howett et al., 2011). Combined with the ISS images, the correlation between the fractures at the south pole region and the high temperatures were discovered, suggesting that an internal heating mechanism is linked with the origin of the plume originating from the moon's fractures. The underlying source of this high endogenic power can be explained through heat generated by tidal interactions in combination with Enceladus' subsurface ocean leading to geothermal activity, including hydrothermal vents, releasing heat from Enceladus' interior (Choblet et al., 2017).

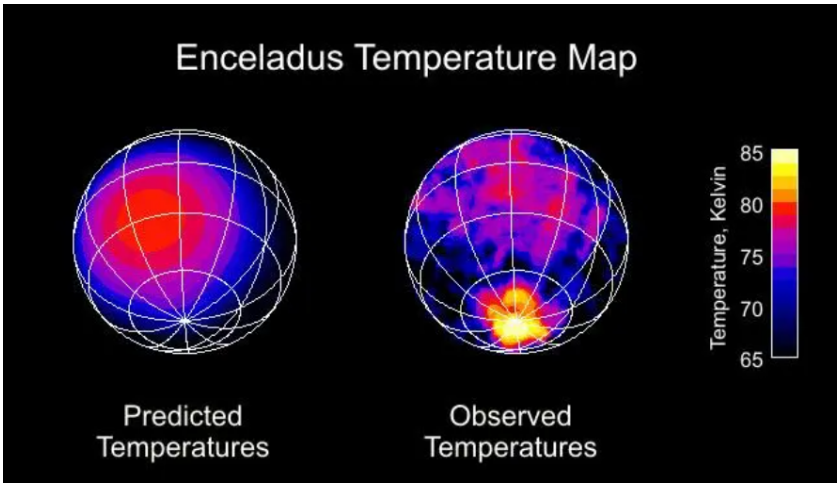

Figure 2.5: Predicted and Observed Temperature of Enceladus [4]

2.1.2. Interior Properties

From Cassini's measurements of the topography, gravity, and temperature certain interior properties of Enceladus can be deduced. This includes everything from its icy crust, to the subsurface ocean, to the rocky core. As the icy crust has been described in more detail already, this section focuses on Enceladus' core and subsurface ocean.

Core of Enceladus

The interior of Enceladus consists of an icy crust on the outside with a subsurface ocean underneath and a rocky core at its centre. The current configuration of Encelauds' ice shell structure of 20-30 km is a point of discussion as uncertainties about how it remains stable still stand. The ice layer at the equator is significantly thicker than at the south pole region as this ranges between 3 and 5 km. Lateral shell thickness variations create a stress that would reduce the thickness of the ice shell over time. The stability of this shell thickness variation is not well understood, but tidal dissipation taking a part in this equilibrium is most likely (Hemingway et al., 2018). In Figure 2.6 these layers and some interrelations are indicated. It is shown how the icy crust is thicker around the equator and thinning towards the poles with the thin icy crust correlating with localised heating mechanisms originating from the core and seafloor. The possible core interactions are indicated as well, showing a passive influx of water from the subsurface ocean into the porous rocky core which in turn is heated and interacts with the rocks. Choblet et al. (2017) showed that tidal friction inside a rocky core like in Enceladus can create 10 GW worth of heat. The jets resulting from these interactions are depicted in Figure 2.6 as well.

The interior properties, like the thickness and density of the core, ocean, and icy crust, can be determined through various methods leading to slightly varying results. The derived (or prescribed) values for these properties and method used by seven different papers are summarised in Table 2.1. These values have been determined using a combination of gravity, topography, physical libration amplitude, and librations, which are the slight oscillations that occur in the rotational motion of celestial bodies resulting from variations in the body's orbital and rotational dynamics. From the results in Table 2.1, an average core radius of 190 km with a density of 2400 kg m^{-3} can be determined. For the icy crust, Hemingway et al. (2018) indicate that around the south pole the thickness is around 16-18 km, whereas this is 30-40 km around the equator depending on the model considered. The thickness of the subsurface ocean depends on the thickness of the icy crust as well ranging between 10 and 60 km (Hemingway et al., 2018).

Subsurface Ocean

The existence of a liquid water ocean underneath the surface was indicated after the presence of ammonia NH_3 was detected at a ratio of 0.8% in the plume from Cassini's Ion and Neutral Mass Spectrometer (INMS) data. This is an important detection as NH_3 can lower the freezing point of water (Waite Jr et al., 2009; C. Hansen et al., 2020). From the flyby in October 2015, the presence of molecular

[4] https://science.nasa.gov/resource/enceladus-temperature-map/

Paper	Core	Ocean	Icy Crust	Method
Iess et al. (2014)	~190 km (~2400 kg m^{-3})	10-30 km (1000 kg m^{-3}*)	30-40 km (920 kg m^{-3}*)	Based on gravity and topography
W. McKinnon (2015)	190-195 km (~2450 kg m^{-3})	~10 km (1007 kg m^{-3}*)	~50 km (925 kg m^{-3}*)	Based on gravity and topography
Thomas et al. (2016)	~200 km (~2300 kg m^{-3})	26-31 km (1000 kg m^{-3}*)	21-26 km (~850 kg m^{-3})	Based on physical libration amplitude
Čadek et al. (2016)	180-185 km (~2450 kg m^{-3})	~50 km (~1030 kg m^{-3})	18-22 km (925 kg m^{-3}*)	Based on gravity, topography, and librations
Van Hoolst et al. (2016)	170-205 km (2158-2829 kg m^{-3})	21-67 km (950-1100 kg m^{-3})	14-26 km (900-1000 kg m^{-3})	Based on physical libration amplitude
Beuthe et al. (2016)	186-196 km (2350-2480 kg m^{-3})	34-42 km (1020 kg m^{-3}*)	19-27 km (925 kg m^{-3}*)	Based on gravity and topography
Hemingway et al. (2018)	188-205 km (2200-2450 kg m^{-3})	12-36 km (1000-1100 kg m^{-3})	22-41 km (850-950 kg m^{-3})	Based on gravity and topography

Table 2.1: Interior Properties of Enceladus (Hemingway et al., 2018)

hydrogen H_2 was detected in the plume as well, indicating the possibility that through hydrothermal processes the subsurface ocean is reacting with rocks as is visualised in Figure 2.6 (Waite et al., 2017). The formation and upkeep of such an ocean can be caused by subsurface dissipation of tidal heating, frictional heating, warm ice convection, and tidal dissipative heating (Yin and Pappalardo, 2015).

Regarding the composition and nature of the ocean liquid, chemical analysis has shown indications that the ocean is salty (Choblet et al., 2017). Data from Cassini's instruments have shown indications of the ocean being relatively alkaline and having a reduced solution of dissolved sodium, chloride, and bicarbonate or carbonate ions just under the freezing point of pure water (Glein et al., 2018). The model by Glein et al. (2015) indicates that the ocean has a Na-Cl-CO_3 solution with an alkaline pH of 11-12.

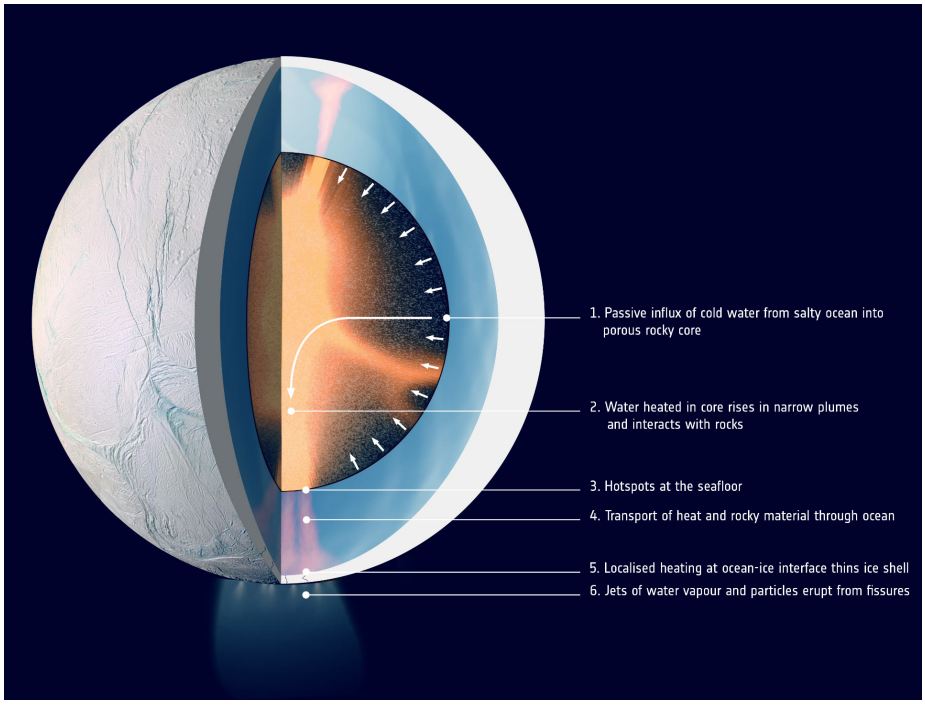

Figure 2.6: Core of Enceladus [5]

[5]https://www.sci.news/space/planetaryscience/enceladus-highly-porous-core-subsurface-ocean-warm-05409.html

2.1.3. Plume

The plume emanating from Enceladus' surface, as a result of many jets spewing water vapour from the tiger stripes, is a fascinating feature of the icy moon. At almost 10,000 km long, observed by the James Webb telescope in 2023, the plume is almost 20 times the size of the moon itself (diameter of 504km) (Villanueva et al., 2023). This section describes the composition of the plume, which is interesting for the study of Enceladus' surface properties as some of these plume particles fall back onto the surface.

Particles and Composition

On two flybys of Enceladus in 2005, Cassini's Ultraviolet Imaging Spectograph (UVIS) observed stellar occultations that confirmed the nature and composition of a water vapor plume in the SPT of Enceladus. UVIS observed that the gas composition of the plume primarily contains water (C. J. Hansen et al., 2006). These stellar occultations observed highly collimated supersonic gas jets within the plume as well. C. Hansen et al. (2020) notes that this means that all gas molecules are emitted with a thermal velocity higher than Enceladus' escape velocity. In addition to the UVIS observations, the VIMS also took measurements of the particles in Enceladus' plume. These were taken at an altitude between 50 and 300 km, measured from the surface. This showed that the primary component in the plume is fine-grained water-ice (Hedman et al., 2009). The band minimum position of these particles, as the VIMS data shows, indicates that these water-ice particles are primarily crystalline in the plume as well (Dhingra et al., 2017). From VIMS data of 2017, it is also speculated that the distribution of the particle size in the plume changes over time (Sharma et al., 2023). Besides changes in particle size distribution, a combination of ISS and VIMS data shows that the ice grain output of the plume varies systematically with the orbital phase of Enceladus. It is suggested that the cause of these variations are a consequence of the tidal stresses due to Enceladus moving in an eccentric orbit around Saturn (Sharma et al., 2023; Hedman et al., 2013). It is possible that these distribution differences reflect a variation in the conditions for particle formation or transportation within the tiger stripe cracks.

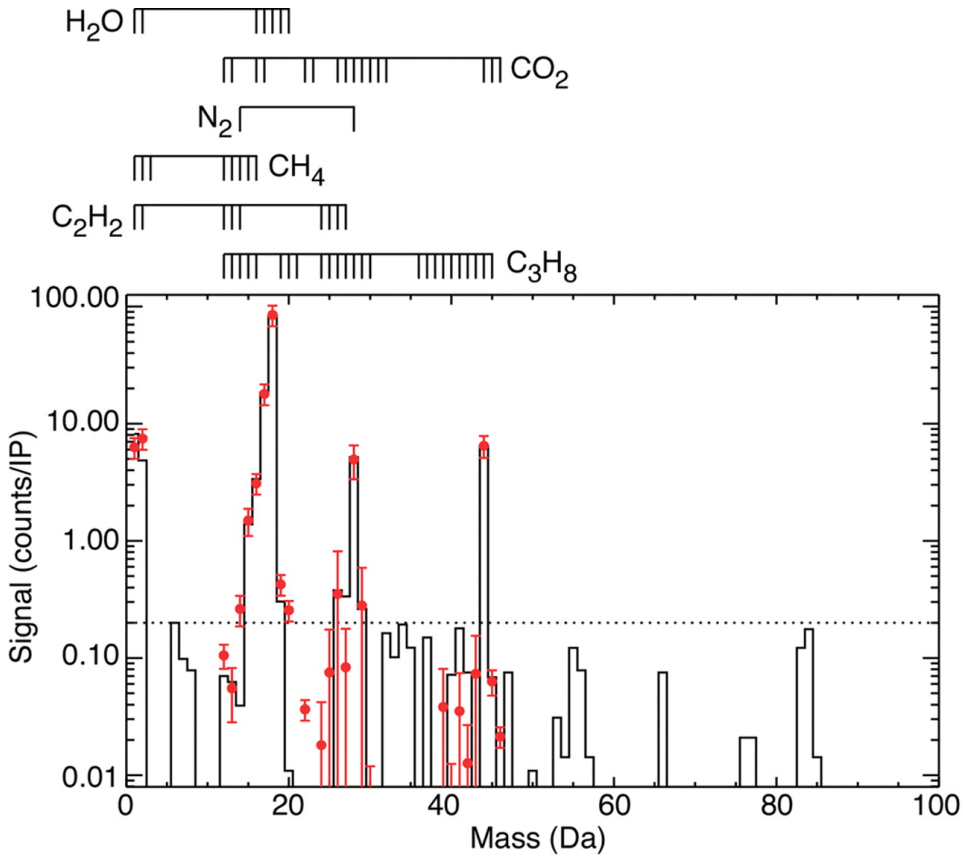

Figure 2.7: Average Mass Spectrum of Enceladus' Plume (Waite et al., 2006)

The volatile composition of Enceladus is mainly derived from the plume's composition as measured

by the INMS instrument. The source for these particles are assumed to come from Enceladus' probable subsurface ocean. During the flyby of Cassini in July 2005, the INMS instrument was able to measure mass spectra of the atmospheric plume and coma, which is the cloud of particles that surrounds the ejected materials. From the mass spectrum depicted in Figure 2.7, the presence of H_2O, CO_2, N_2 or CO, CH_4, C_2H_2, and C_3H_8 is indicated. It is also possible that NH_3 and HCN are present, but at a level of less than 0.5%. This gives an atmospheric composition of $91 \pm 3\%$ H_2O, $3.2 \pm 0.6\%CO_2$, $4 \pm 1\%N_2$ or CO, and $1.6 \pm 0.4\%CH_4$ (Waite et al., 2006). INMS also detected the presence of H_3O^+ cations in the plume, which is the result of a reaction between H_2O^+ and H_2O (Sakai et al., 2016). Together with H_2O^+ and water cluster ions, the H_3O^+ ion was detected in the downstream edge of the plume (Cravens et al., 2009). The flyby of Enceladus in 2008 provided data, as presented in Figure 2.8, that allowed the identification of higher-order hydrocarbons such as benzene and possibly methanol and formaldehyde.

	Type I	**Type II**	**Type III**	**Stream particle nano grains**
Number fraction	60 - 70 %	20 - 30 %	∼10%	-
Main non-water constituent (MNWC)	Na, K	Organic	Na and K salts	SiO_2
Typical MNWC concentration in individual grains	$< 0.0001\%$	0.000001-10%	0.5 - 2%	high

Table 2.2: Grain Type Composition in Saturn's E Ring (Postberg et al., 2018)

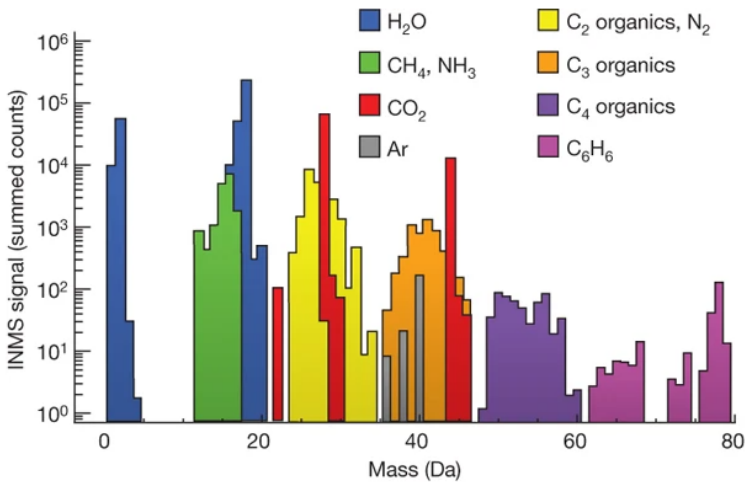

Figure 2.8: INMS Mass Spectrum October 2008 (Waite Jr et al., 2009)

The flyby in 2008, with new Cosmic Dust Analyser (CDA) modifications, resulted in the compositional plume profile in Figure 2.9. This graph shows the relative frequencies of the three types of compositional ice grains identified by CDA in Saturn's E ring. The composition of these three types are given in Table 2.2. Figure 2.9 shows a simultaneous increase in type III grains and decrease of type I grain just before the closest approach. Postberg et al. (2011a) provides the possible explanation that the salt-rich grains (type III) are ejected at lower velocities than type I salt-poor grains. This difference in size distribution could be responsible for the different ejection velocities (Postberg et al., 2011a). The type II grain proportion is slightly higher in the more dense part of the plume, implying that the ice grains with organic constituents are related to the high speed, collimated jets (Postberg et al., 2018, 2011a). It is likely that the small purest ice grain particles (< 0.4 μm) condense from the plume's gas and get into Saturn's E ring orbit. The type III salt-rich grain particles however, are suggested to come from liquid water, in the subsurface ocean, in combination with a rocky core that could be reacting with the liquid (C. Hansen et al., 2020).

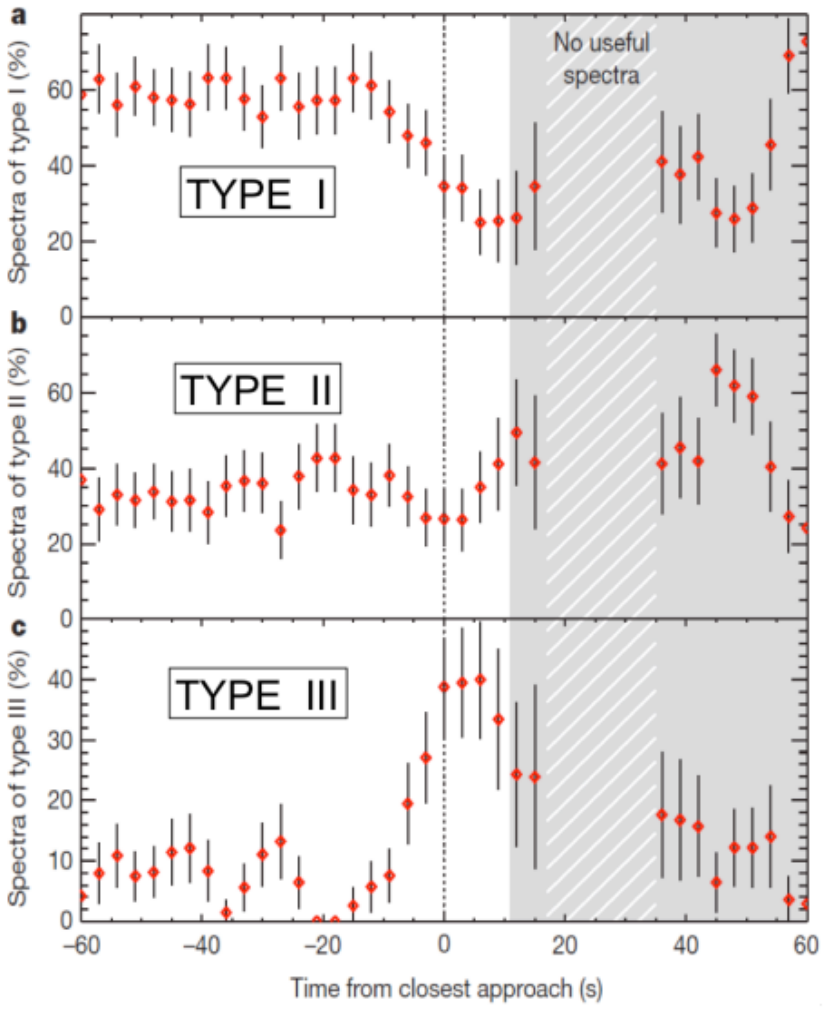

Figure 2.9: Compositional Plume Profile (October 2008) (Postberg et al., 2018)

Plume Deposition

Porco et al. (2017) state that 68 to 93% of the plume particles fall back on the surface based on their modelling. Some larger grain particles fall back to the surface of Enceladus for certain escape conditions. Figure 2.10 indicates the escape and non-escape conditions for these particles. Based on their size in radius (a) and launching speeds (v_0) at the vents, the impact or escape speed (on the left) and impact or escape time (on the right) is shown. This is done for both confined (bound), which impact Enceladus, and non-confined (unbound) particles, which escape Enceladus (Flandes et al., 2024). The figure shows how a smaller grain size needs a smaller launching speed to escape. To take the left figure of Figure 2.10 as an example, the impact speed and escape speed are given as a gradient, where a larger grain size (a) indicates that the impact or escape speed increases as well. Flandes et al. (2024) indicate how confined grains with a size larger than 0.3 µm and a launching speed below the escape velocity could travel up to seven hours before it impacts Enceladus' surface, with an impact speed in the same order of magnitude as the grain's launch speed. They specify how micron-sized particles with low launch speeds particularly impact Enceladus' surface a few minutes after ejection, landing close to the vents. In their study they left out the possibility that Enceladus recaptures particles that did escape the moon but could later collide again (Flandes et al., 2024). Larger grain sizes have been detected in the plume as well, with Cassini's Radio and Plasma Wave Spectrometer (RPWS) measuring grains up to 50 µm, which should fall back onto Enceladus' surface as well (Dong et al., 2015).

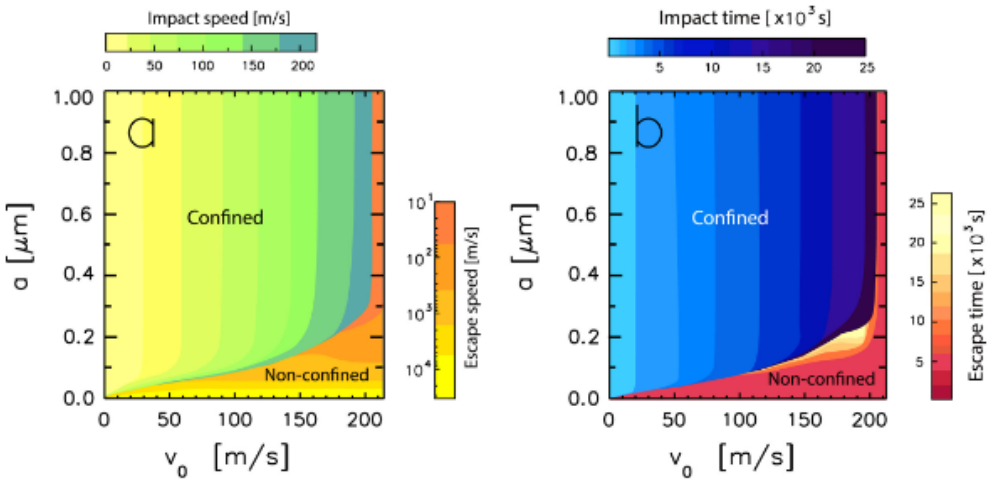

Figure 2.10: For bound and unbound particles, a) the impact and escape speed and b) impact and escape time (Flandes et al., 2024)

The plume deposition rate, as simulated by Kempf et al. (2010) and Southworth et al. (2018), was determined to be 0.5 mm per year at the surface near the vents, and 10 μm per year at regions in the northern hemisphere when the density of compact ice is assumed (ρ = 0.9 g cm^{-3}) (Postberg et al., 2018). Figure 2.11 indicates the deposition rate of the plume particles for sizes ranging from 0.6 to 15 μm, as modelled by Southworth et al. (2018) based on jet sources given by Spitale and Porco (2007). These calculations are done based on a mass production rate of 20 kg/s. Southworth et al. (2018) indicate that there is a linear relation between the mass deposition and mass production rate, meaning that the surface deposition structure is consistent with mass production rate changes. The structure is also minimally affected by changes in the size distribution slope as it always indicates an increased deposition close to the vents and decreased deposition further away (Southworth et al., 2018). In a continuation of their studies, Southworth et al. (2019) studied the effects of the zenith angle (or tilt) of the jets on the surface deposition of the plume, which is the angle between the surface and the jets. They found indications that most jets should be relatively orthogonal to Enceladus' surface and that it is unlikely for jets with a large zenith angle to be active for a long time (Southworth et al., 2019).

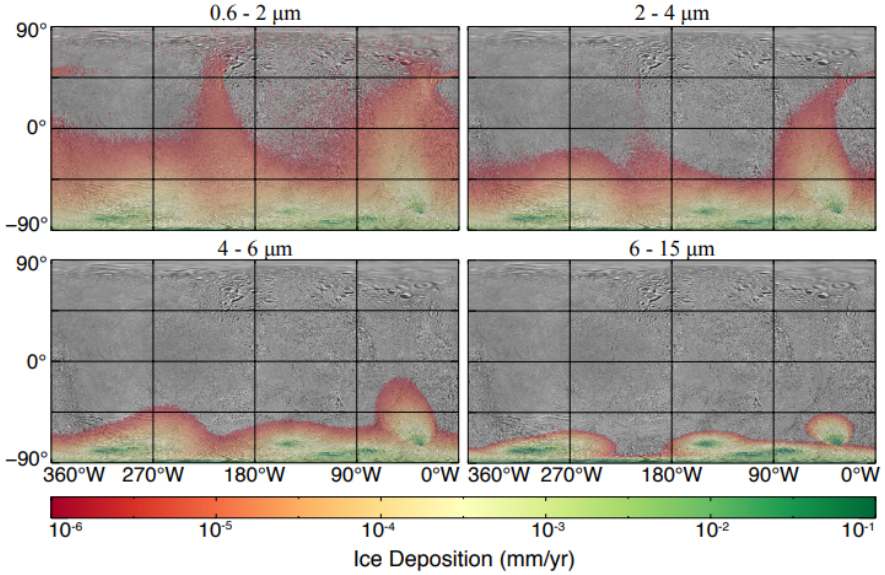

Figure 2.11: Plume particle deposition rate for particle sizes ranging from 0.6 to 15 μm (Southworth et al., 2018)

2.2. Ice Characteristics

Ice, the solid state of water, forms when water molecules freeze and can arrange into a crystalline or amorphous structure depending on the circumstances under which it forms. To understand these and other characteristics of ice, this section describes the morphology, material properties, and mechanical properties of ice. This section is concluded with a description of the current knowledge of the ice present on Enceladus.

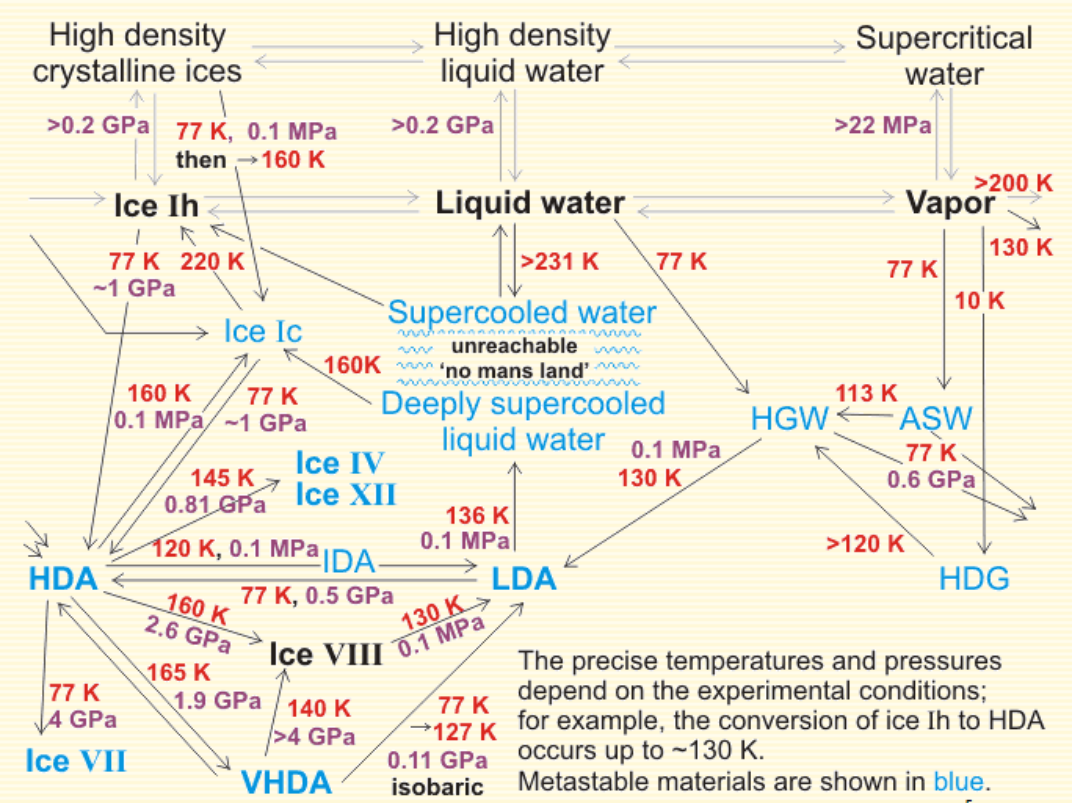

Figure 2.12: Relation between different ice forms[6]

2.2.1. Morphology

The morphology of ice describes the different forms and characteristics of the various existing ice types. The most common chemical compounds in the universe are hydrogen, helium, and to a lesser extent oxygen and carbon. Through the reaction of oxygen and hydrogen, the hydroxyl radical OH is formed, which gives the water molecule after another reaction with hydrogen. Water molecules form into an ice lattice by arranging themselves in a hexagonal pattern and bonding to neighboring molecules through hydrogen bonds during the freezing process. When ice is formed by the inclusion of molecules other than water within the ice lattice through hydrogen-bonds, this is called molecular ice. These ices can be present in various crystalline or amorphous phases. Amorphous ice is a disordered form of ice lacking long-range molecular order, resembling liquids, and is often formed by rapid cooling or deposition processes. Amorphous ice generally forms at a temperature below 130 K and is most common in space (Ehrenfreund et al., 2003). Crystalline ice is a structured form of ice characterised by a regular and repeating atomic arrangement. Crystal ice indicates that the ice was formed under a higher pressure and temperature than amorphous ice. This could be caused by external pressure, stress, or temperature on the ice (Ehrenfreund et al., 2003).

[6] https://water.lsbu.ac.uk/water/amorphous_ice.html#ida

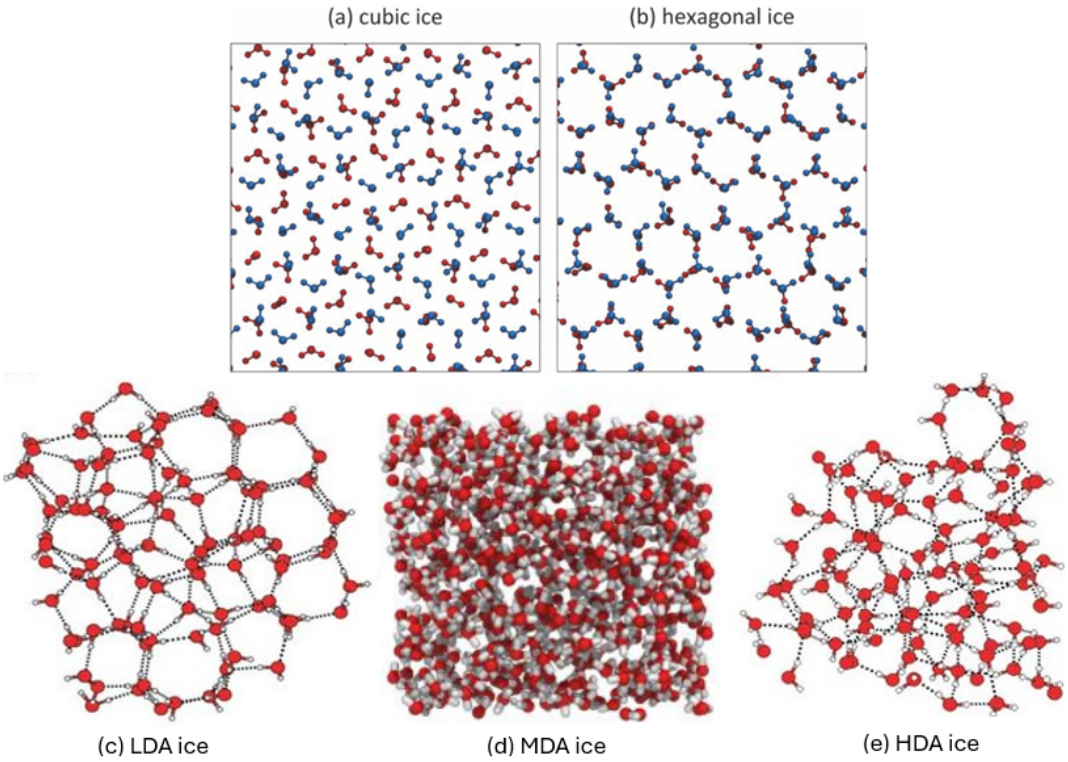

Figure 2.13: The structural arrangements for I_c, I_h, LDA, MDA, and HDA ice based on images by Seo et al. (2012), Belosludov et al. (2008), and Rosu-Finsen et al. (2023).

Within amorphous and crystalline ice, there are at least twenty phases in which that ice can present based on the temperature and pressure. Many different crystalline ice structures exist with ice phases up to Ice XIX, which are ice phases numbered in order of discovery. The most stable crystalline ice types are the normal hexagonal (I_h) and metastable cubic (I_c) crystalline ice, where I_h is more stable than I_c (Tanaka and Okabe, 1996). Ice types in other phases are less stable, which results in most ice types transforming into I_c and I_h at temperatures of 125-170K and 200K respectively (G. B. Hansen and McCord, 2004). At colder temperatures, amorphous ice generally forms due to the water molecules lacking the mobility to form a regular crystalline structure. Four forms of amorphous ice have been identified: low-density amorphous (LDA), medium-density amorphous (MDA), high-density amorphous (HDA), and very-high-density amorphous (VHDA). Figure 2.12 shows the relation between these amorphous and crystalline ices, including at what temperatures and pressures they transform. This section considers mostly the left side of the figure. The 'no mans land' indicated under liquid water is shown as the limit of homogeneous nucleation where liquid water does not exist.

LDA is often formed by depositing water vapor onto a cold substrate at low temperatures. It has a relatively open and disordered structure compared to high-density forms. The intrinsic density of LDA is 0.94 g/cm^3. HDA has a more compact structure and is typically formed by rapidly cooling liquid water or by compressing ice to high pressures. Its density starts at 1.13 g/cm^3 at an ambient pressure and temperature of 77K. Depending on the pressure and temperature, the density differs slightly. The characteristic of VHDA is that it has a density higher than HDA at 1.25 g/cm^3, formed at extremely high density or by compressing HDA to higher pressures. VHDA also has a more densely packed molecular arrangement compared to HDA. MDA, discovered recently, is an intermediate form of amorphous ice with a density between LDA and HDA of 1.02 - 1.06 g/cm^3 (Finney et al., 2002). It can be formed by annealing LDA, which is a heat treatment process that involves heating the material to a specific temperature and then cooling it slowly. MDA can also be formed by compressing ice I_h to intermediate pressures (Rosu-Finsen et al., 2023).

Figure 2.14 shows the phase diagram of the varying ice phases indicating the regions of liquid water, polymeric ice, and hydrogen ordered and disordered phases in terms of temperature and pressure. In this figure, the stable phases are indicated in bold, whereas the metastable phases are shown with a smaller font (Salzmann, 2019). In Figure 2.15 the amorphous ice phases are included as well with the

exception of MDA which should be indicated between LDA and HDA (Stern and Loerting, 2017). When pressurising I_h up to 1.5 GPa at a temperature of 77 K, the amorphous HDA is formed. Pressurising LDA at 0.6 GPa at the same temperature also results in HDA ice being formed. Once a temperature of 150 K is reached, LDA crystallises. Hemley et al. (1989) showed that HDA ice can suddenly transform into a crystalline phase (VII or VIII) at a pressure of 4 GPa and temperatures of 77K and higher. The formation of VHDA occurs in the sequence of LDA to HDA to VHDA at 125 K, whereas the VHDA transformation does not occur at all at temperatures below 100 K (Loerting et al., 2006). Compression of MDA at 77 K shows a transition to HDA starting at a pressure of 1.1 GPa (Rosu-Finsen et al., 2023). The transition of I_h to MDA could be facilitated by shear forces caused by the tidal forces in the interiors of icy moons when occurring at similar temperature and pressure ranges. Stacking disordered ice (I_{sd}) can be pressured to an amorphous phase at temperatures up to 174 K if the compression rate is close to 50 GPa/s (Salzmann, 2019).

2.2.2. Material Properties

In this section the material properties of ice are described, including the thermal conductivity, viscosity, and porosity of ice. These material properties of water ice are dependent on its crystalline or amorphous structure type. The formation of these ice phases are dependent on the temperature and pressure of its environment, as is visualised in Figure 2.12. Each phase has a different H_2O molecule arrangement and degree of proton disorder in its lattice (Ehrenfreund et al., 2003). The structure of crystalline water ice is H_2O molecules with the ability to donate two H-bonds and accept two other bonds as well. The I_h type is characterised by the hexagonal symmetry of the oxygen atoms and tetrahedrally H_2-bonded water molecules, while I_c shows oxygen atoms in a cubic structure. Besides the difference in atom arrangement, these two ice types have a similar density of 0.93 g/cm^{-3} and 0.94 g/cm^{-3} at a temperature of 80 K for I_h and I_c respectively (Loerting et al., 2011). The differences in structural arrangements for I_h, I_c, and amorphous ice are shown in Figure 2.13. A study by Jenniskens and Blake (1996) compared crystalline and amorphous ice warmed to varying temperatures up to 144K. They state that crystalline ices found in interstellar grains showed similar structural properties to the warmed amorphous ice in their study, which may have formed during heating events of the grains. These similar properties include the possible tendency to remove dust grain impurities and form droplets. They state that an effect like this, separating ice and dust grain impurities, can happen at temperatures below 70 K at which it is possible for UV photon irradiation to decrease the viscosity of HDA ice (Jenniskens and Blake, 1996).

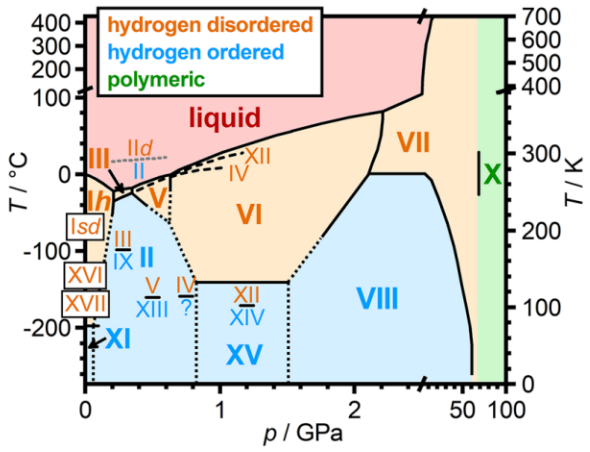

Figure 2.14: Regular phase diagram of ice (Salzmann, 2019)

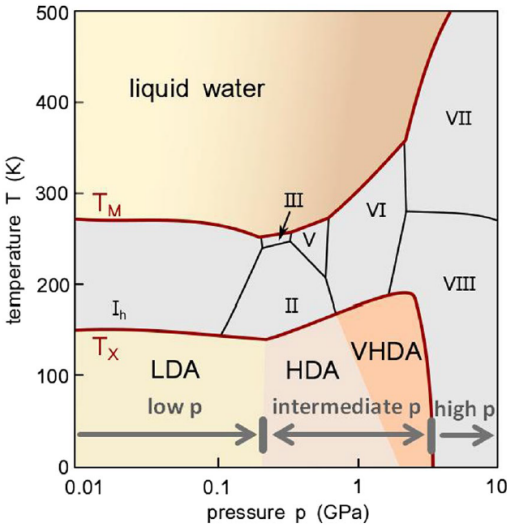

Figure 2.15: Phase diagram including amorphous ice (Stern and Loerting, 2017)

Viscosity is a measure of a fluid's resistance to flow, where a higher viscosity indicates that the substance flows more slowly. As temperature decreases, ice becomes more viscous having a relatively high viscosity compared to liquids. Amorphous ice can exhibit a wide range of viscosity properties depending on its formation process and temperature. HDA and VHDA behave more like a solid than

a liquid, and exhibit high viscosity and are relatively stable at low temperatures. LDA on the other hand behaves more like crystalline ice with a lower viscosity (Jenniskens and Blake, 1996). Another aspect that influences certain ice characteristics is its porosity. In ice, porosity refers to the presence of air, vacuum or other gases that are trapped within the ice structure, which is determined through the average and intrinsic density of the ice. At atmospheric pressure (1 atm), the average and intrinsic densities are 0.917 g/cm^3 and 0.934 g/cm^3 respectively. The amount of porosity can vary depending on factors such as the freezing process, temperature, and pressure conditions. Generally, amorphous ice can have a relatively high porosity compared to crystalline ice as its disordered structure can contain more void spaces (Gómez et al., 2020).

The thermal conductivity $\varkappa$ of water is very high relative to other liquids at >0.5 $\frac{\mathrm{mW}}{\mathrm{Km}}$. This anomalous behaviour is believed to be caused by the H_2-bond structure (Iriarte-Carretero et al., 2018). For I_h ice it was found that its thermal conductivity decreases with increasing pressure, which is unlike the behaviour of most solids. Figure 2.16 shows the thermal conductivity for crystalline and amorphous ices for several temperatures. LDA, HDA, I_h, and I_c are plotted for a temperature of 130 K, ice II at 240K, ices V, VI, and VIII at 246K, ice VII at 286K, ice XI at 58K, and metastable ice XII at 115K (Andersson and Inaba, 2005). Andersson and Inaba (2005) found that through isothermal pressurisation of I_h ice at 130 K, an implosive transition occurs between 0.8 and 1.0 GPa during the amorphisation causing a sudden pressure decrease of 0.1 GPa. A pressure induced decrease of thermal conductivity for I_h, I_c, and LDA ices is the result of decreasing phonon velocity. The thermal conductivity of LDA ice decreases with increasing temperatures, showing typical behaviour of crystal-like ice. This is probably caused by strong phonon-phonon scattering (Andersson and Inaba, 2005).

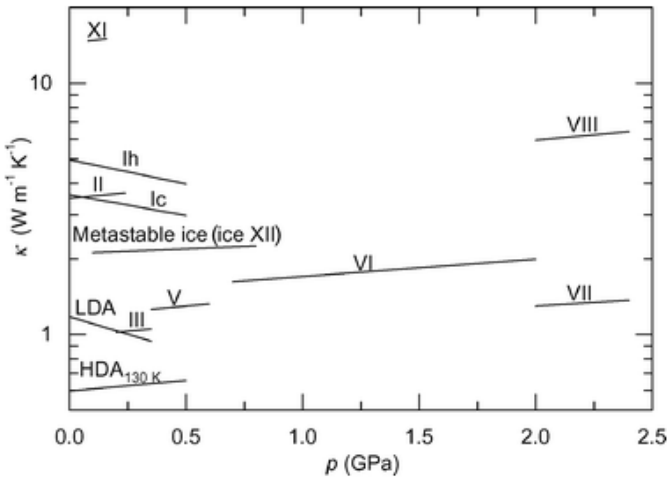

Figure 2.16: Thermal conductivity of crystalline and amorphous ices (Andersson and Inaba, 2005)

2.2.3. Mechanical Properties

The mechanical properties of ice describe its strength and deformation properties in the form of elasticity, brittleness, ductility, and creep. Understanding these properties is especially relevant for potential landing missions on icy surfaces as ice deformation properties are important for the bearing of ice.

The strength of a material indicates its resistance to deformation or fracture under applied stress, which can be described as tensile or compressive strength. For the strength of ice, this is influenced by the temperature, volume, ice grain size, and strain rate, which is the rate at which deformation occurs in a material over time. For ice I, a tensile strength from 0.7 MPa to 3.1 MPa was found with a compressive strength ranging from 5 to 25 MPa for temperatures between 250 and 260 K (Petrovic, 2003). At a temperature of 100 K, a compressive strength of 70 MPa shows that a decrease in temperature results in an increase in compressive strength (Arakawa and Maeno, 1997). These are strength indications for frozen solid ice, which will vary for smaller samples with fine ice grains freezing over a shorter amount of time. An increase in strain-rate and grain size also results in an increased compressive strength (Cao et al., 2018). An increased strain-rate indicates that the force is applied more rapidly, which tends to lock the molecules of the ice together more tightly, increasing its strength and resistance to compression. Bigger grain sizes result in increased compressive strength as there are fewer contact points between

the grains where deformation can occur. The tensile strength of ice is insensitive to the temperature and strain rate, but does decrease with an increasing volume and ice grain size (Petrovic, 2003).

The elasticity of a material indicates its ability to return to its original shape after deformation. Ice exhibits anisotropic elasticity, meaning its mechanical properties vary depending on the direction of the applied stress relative to its crystal structure. While crystalline ice displays elastic behavior up to a certain stress threshold, amorphous ice may behave more like a viscoelastic material, with properties intermediate between those of a solid and a liquid (Hessinger et al., 1996). The Young's modulus, also known as the modulus of elasticity, quantifies a material's ability to deform elastically under stress along its length, relative to its cross-sectional area. The Young's modulus E is calculated by dividing the stress σ, which is the amount of force over the area, by the strain ε, which is a measure of the deformation. The formula for calculating the Young's modulus is indicated in Equation 2.1.

$$\mathrm{E} = \frac{\sigma}{\varepsilon} = \frac{\mathrm{F/A}}{\Delta \mathrm{L/L}} \quad [\mathrm{Pa}] \quad (2.1)$$

For monocrystalline ice, the Young's modulus is around 9 GPa at a temperature close to the melting point, varying between 8.6 and 12 GPa depending on the direction the stress is placed. The Young's modulus of polycrystalline ice was found to be in the range of 6.0 to 12.0 GPa (Gold, 1988). Palanque et al. (2023) show however that there is a correlation between the Young's modulus of ice and its density. It was shown that an increased density also results in an increased ice stiffness. The Young's modulus and stress-strain curve show the deformation behaviour of a material, where different curves indicate different deformation styles. Figure 2.17 indicates the different points of interest that can be identified through a stress-strain curve. The proportional limit at point A indicates the maximum allowable stress of the material, with point B indicating when the deformation of the material becomes plastic (permanent). The steepness of the curve indicates the brittleness of the material, where a steep curve indicates a brittle material and a shallow curve a plastic material.

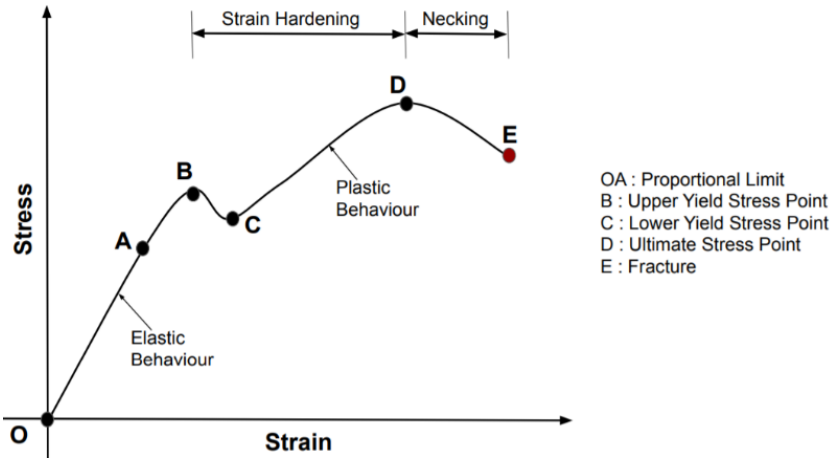

Figure 2.17: The different points of interest in a stress-strain curve [7]

The brittleness of a material shows its tendency to fracture under the applied stress instead of deforming. When rapid straining of ice occurs it undergoes brittle fracture. Crystalline ice is more brittle than amorphous ice as the molecules in amorphous ice can move more freely. Under tensile load, bicrystals exhibit either brittle or ductile fraction, while under compression it indicates a ductile fraction only (Cao et al., 2018). Ductile fraction indicates the ability of a material to deform plastically before fracture. Ductility is characterised by strain-rate hardening and thermal softening, while brittle behaviour occurs at higher strain rates (Schulson, 1999). Brittle failure due to compressive load is characterised by a sudden material collapse. Under tension, $\mathrm{I_h}$ ice fails through crack nucleation and propagation (Schulson and Renshaw, 2022). A systemic change from brittle fracture to ductile deformation was observed at a critical strain-rate and temperature (Arakawa and Maeno, 1997). The ductile-brittle transition resulting from a compressive load indicates a point of maximum compressive

[7] https://www.smlease.com/entries/mechanical-design-basics/stress-strain-curve-diagram/

strength of the ice (Schulson, 1999). Leonard et al. (2017) indicate that the brittle-ductile transition of the ice on Enceladus' surface is likely to happen when the viscosity of the ice is 10^{13}-10^{17} Pa s. This suggests that the ice at the surface is ductile with a high heat flow at the SPT (Leonard et al., 2017). The creep of a material indicates a slow, time-dependent deformation which occurs under constant stress. Typically for ice, this occurs close to its melting point. The ability of ice crystals to rearrange and slide past each other cause the ice to gradually deform even without melting completely. While crystalline ice deforms through the movement of crystal defects and grain boundaries, amorphous ice deforms through the rearrangement of its disordered molecular structure. Creep is more pronounced in ice under pressure, where the weight of the ice mass applies continuous stress, causing it to flow like a viscous fluid (Weertman, 1983).

2.2.4. Type of Ice on Enceladus

The surface of Enceladus contains mostly near pure water ice, except around the SPT. There, CO_2 and crystalline water ice are present (Brown et al., 2006). Figure 2.18 shows an infrared spectral map of Enceladus, which was obtained by combining Cassini's ISS images with VIMS data. In this map, the red indicates fresh crystalline ice with a brightness ratio observed at 3.1 μm over 1.65 μm, the green indicates brightness at 2.0 μm, and the blue indicates brightness at 1.18 μm. This map indicates a high degree of crystalline ice, shown as red, on the surface of Enceladus around the tiger stripes. Combined with disk-integrated spectra, it was found that the water-ice in the equatorial and mid- to high-latitude regions of Enceladus is mainly crystalline. The crystalline ice is indicative of thermal mechanisms, such as the geolocial activities at the tiger stripes, but also other geological activity as the northern hemisphere, without known fractures, shows the presence of crystalline ice as well. The presence of amorphous ice on Enceladus is uncertain. Newman et al. (2008) indicated a presence of amorphous ice between the tiger stripes, suggesting its presence is due to intense radiative bombardment, flash-freezing of cryovolcanic liquid, or rapid condensation of water vapour particles. Postberg et al. (2018) however indicate that the presence of amorphous ice on Enceladus' surface remains uncertain as the indicators for amorphous ice could also be explained by the effects of diffractions from sub-micrometer ice grains. The discovery of MDA ice in 2022 may provide different implications as the tidal forces on Enceladus could produce MDA ice through similar shearing processes that produced this ice in the laboratory (O'Callaghan, 2023).

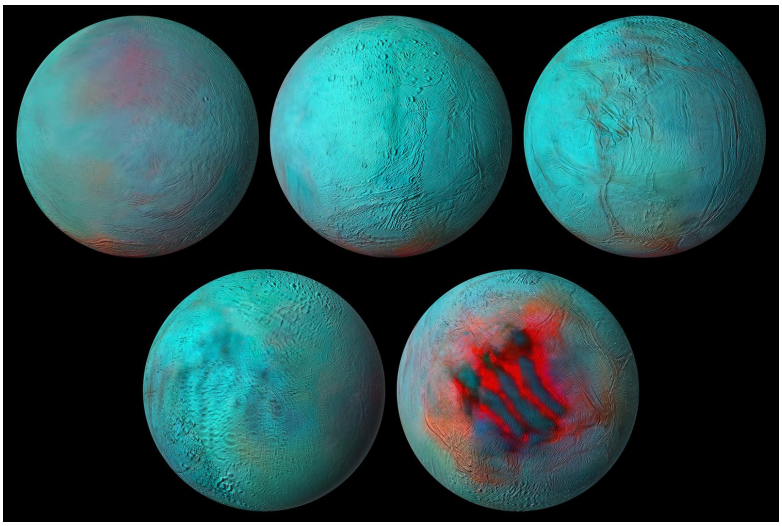

Figure 2.18: Infrared Spectral Map of Enceladus. The red indicates fresh crystalline ice with a brightness ratio observed at 3.1 μm over 1.65 μm, the green indicates brightness at 2.0 μm, and the blue indicates a brightness at 1.8 μm [8]

From Casini's Radio Detection and Ranging (RADAR) data it was found that Enceladus, together with another icy moon of Saturn named Tethys, has the highest SL (Synthetic Aperture Radar Long) radar albedo with two measurements for Enceladus of 1.53 ± 0.01 and 1.67 ± 0.12. This indicates that

[8] https://www.jpl.nasa.gov/images/pia24023-enceladus-in-the-infrared

several decimeters of the surface layer are probably extremely clean water-ice with a structural complexity that causes high-order multiple scattering inside (Ostro et al., 2006). The echo spectra obtained from RADAR measurements suggest this as well, showing broad shapes, which indicates diffuse scattering as a result from structural complexities (Ostro et al., 2006).

From spectral analysis, it was found that Enceladus' surface is dominated by water ice with the size of the water-ice grains typically being 50 - 150 μm, but having an increased size of 100 - 300 μm near the tiger stripes (Brown et al., 2006; Jaumann et al., 2008). In addition to water-ice, traces of free (absorbed) CO_2 and trapped (embedded) CO_2 molecules were found in the tiger stripes. W. B. McKinnon et al. (2018) make the conventional assumption that the icy volatiles that are likely accreted into Enceladus' surface are best represented by the composition of comets. Figure 2.19 shows the volatile abundances relate to water in comets with multiple aspects that are worth noting. It is clear that water ice is the dominant volatile, but the cometary volatiles indicated show a 'chemically unequilibrated mélange' rather than a simple compounds mixture composing of a consistent oxidation state and sulfur fugacity (a measure of the escaping tendency of molecules in a system) (W. B. McKinnon et al., 2018).

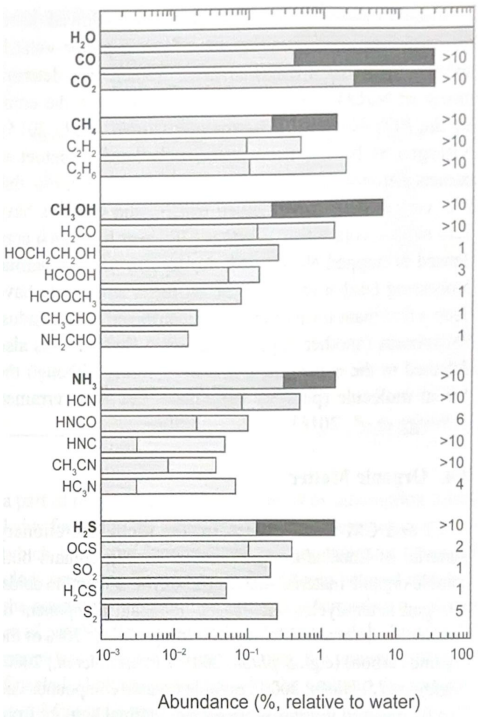

Figure 2.19: Volatile abundances relative to water in comets (W. B. McKinnon et al., 2018)

Additionally, both CO_2 and CO are relatively abundant and CH_4 , NH_3, and CH_3OH are indicated at an important percentage level as well. Finally, it is notable that H_2S is dominant at a percentage of water ice level, but it is not the only sulfur-bearing ice (W. B. McKinnon et al., 2018).

2.3. Ice Sintering

Ice sintering is the process by which individual ice grains bond and fuse together over time, leading to the gradual transformation of a loose, porous ice aggregate into a denser and mechanically stronger material. This process is a mass transport process, where molecules move from one part of the ice structure to another in order to reduce the system's overall surface energy (Blackford, 2007). When two ice grains come into contact, a neck forms between them. As the neck expands, the structure becomes more cohesive and stronger. This process can be driven by several mass transport processes and occurs in three stages, where environmental factors impact the sintering of ice as well.

2.3.1. Mass Transport Processes

There are various mass transport processes that enable the bonding and growth of contact areas, which are commonly called necks, between adjacent ice grains. These processes are driven by the system's tendency to reduce its surface free energy and includes vapour transport, surface diffusion, volume diffusion, grain boundary diffusion, and sometimes pressure-assisted plastic deformation (plastic flow). These can be divided into two categories: surface transport (vapour transport and surface diffusion) and bulk transport (grain boundary diffusion and plastic flow) (Blackford, 2007). Volume diffusion can be placed in both categories. The difference between the two categories is that for bulk transport the matter comes from the interior of the compact and leads to grain shrinkage, whereas for surface transport this comes from the surface and does not lead to grain shrinkage. Usually, one of these processes is dominant, although multiple can contribute. A schematic indicating the primary mass

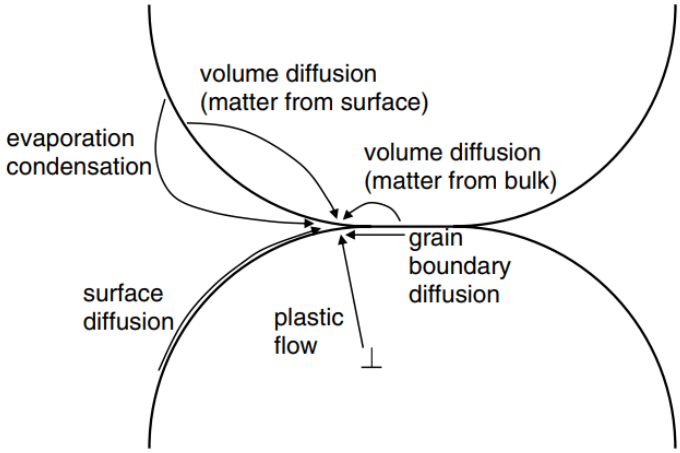

Figure 2.20: Indications of how the mass transport processes can occur in ice sintering between two particles (Blackford, 2007).

transport processes is shown in Figure 2.20. In a simple manner, Figure 2.20 indicates from where each process takes place. In this schematic the vapour transport mechanism is denoted as evaporation-condensation. More elaborate descriptions of each mass transport process is given in the following paragraphs.

Vapour Transport Sintering

Vapour transport sintering, also known as vapour diffusion, is one of the primary mechanisms of ice sintering, especially under conditions where the ice is exposed to air or vacuum. It operates based on the principle that water molecules will move from areas of higher vapour pressure to areas of lower vapour pressure in order to minimise the system's total surface energy (Blackford, 2007). This difference in vapour pressure arises due to the curvature of the ice grain surfaces. Convex regions, such as the rounded tips of the ice grains, have a higher equilibrium vapour pressure compared to concave regions, such as the formed necks. As a result, water molecules tend to sublimate from the convex surfaces and migrate through the vapour phase before condensing in the concave regions. This mass transfer causes the neck between grains to grow, enhancing structural cohesion and reducing porosity over time (Hobbs, 1974). This mass transport process, vapour transport sintering, is particularly significant in low-pressure environments as on Enceladus. Through this process, discrete ice grains gradually bond without requiring melting, leading to significant changes in the microstructure and mechanical properties of granular ice (Hobbs, 1974).

Surface Diffusion

Surface diffusion is a mass transport process in ice sintering where water molecules migrate along the surface of ice grains without undergoing a phase change, as indicated in Figure 2.20. Unlike vapour transport sintering, which involves sublimation and condensation, surface diffusion occurs entirely within the solid phase and involves the lateral movement of absorbed molecules from high-energy convex regions to lower-energy concave regions on the ice surface (Blackford, 2007). As the molecules accumulate at the neck, it grows in size, strengthening the bond between the grains. It is important to note that surface diffusion does not lead to a reduction in porosity or density of the overall system, as it is just existing surface material that is redistributed. In ice sintering, the process of surface diffusion is facilitated by the presence of a quasi-liquid layer, which is a thin film of disordered water molecules that exists below the freezing point, and enhances the molecular mobility along the surface (Hobbs, 1974). Surface diffusion is most active during the initial stage of sintering and is highly temperature-dependent, becoming significantly more efficient at warmer subzero temperatures.

Volume Diffusion

Volume diffusion, also referred to as lattice diffusion, is a mass transport process where water molecules move through the interior crystal lattice of the ice grains, as opposed to along surfaces or grain boundaries (Blackford, 2007). This internal molecular motion redistributes mass towards the neck region

between grains, leading to stronger bonds and more densification, especially in the intermediate to final stages of sintering. Here, individual water molecules migrate through the bulk solid phase of ice via vacancy-mediated processes. This indicates that molecules move by placing into adjacent vacant lattice sites or defects within the crystal structure (Blackford, 2007). The driving force for this diffusion is a gradient in chemical potential caused by differences in curvature and stress, where the neck has a lower chemical potential that the outer convex surfaces prompting net molecular movement towards the neck (Hobbs, 1974). Unlike vapour transport sintering or surface diffusion, volume diffusion leads to a true form of densification of the ice structure where it fills in pores and increases the overall density of the sintered system. However, volume diffusion is generally much slower than other mass transport processes due to the high activation energy that is required for the molecules to move through the crystalline interior. Volume diffusion thus becomes more relevant at higher subzero temperatures or during long sintering times when slower processes can begin to dominate (Blackford, 2007).

Grain Boundary Diffusion

Grain boundary diffusion is a process that occurs along the internal grain boundaries between the individual ice grains in a polycrystalline structure, as depicted in Figure 2.20. Within the context of ice sintering, this process plays a significant role in the intermediate stage of the process, and, unlike surface diffusion, leads to partial densification of the material. Grain boundary diffusion is driven by chemical potential gradients arising from differences in curvature and interfacial stress. Molecules migrate from areas of higher energy into the neck region via the grain boundary, contributing to neck growth and pore shrinkage (Blackford, 2007). In detail, this process works on the narrow boundary that is formed between two grains when they come into contact during sintering, where the crystalline lattices meet but are misaligned (Hobbs, 1974). This boundary is a region of atomic disorder, higher energy, and increased molecular mobility compared to the bulk crystal lattice. Water molecules within this boundary can diffuse more easily due to the looser molecular structure, allowing material to flow toward the growing neck between grains. Grain boundary diffusion is generally faster than volume diffusion, but slower than surface diffusion or vapour transport sintering.

Plastic Flow and Pressure Sintering

While the prior four described mass transport processes are diffusion based, plastic flow is a mechanically driven mass transport process. This is a process by which ice deforms permanently under sustained mechanical stress without fracturing. It is driven by the mechanical process of creep, which is the slow and permanent deformation under stress. In crystalline solids like ice, plastic flow occurs when applied stresses exceed a certain threshold and cause the internal rearrangement of atoms and dislocations within the crystal lattice. These applied stresses can also come from layers of ice, or ice grains, on top of each causing stress to the layers below (Blackford, 2007).

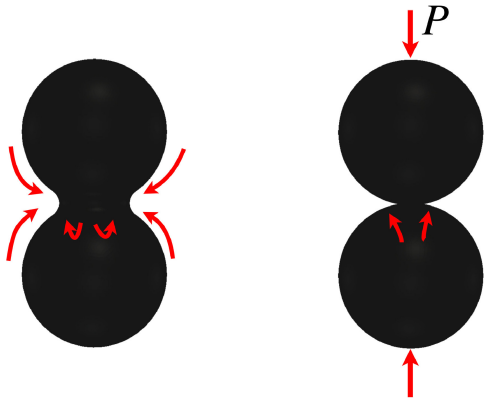

Figure 2.21: The geometry and mass changes ice grains undergo during diffusion sintering (left) and pressure sintering (right) (Kabore and Peters, 2020)

Pressure sintering is closely related to the plastic flow process, as the mechanism of plastic flow contributes to pressure sintering. Pressure sintering is the formation and strengthening of bonds between ice grains due to the application of external mechanical pressure. It involves the creation of grain-to-grain bonds through localised melting, creep deformation (from plastic flow), or otherwise enhanced

mass transport at points of contact (Kabore and Peters, 2020). The difference between plastic flow and pressure sintering can be described as one mechanism that bonds (pressure sintering) as the ice grains are squeezed together, and the other that flows (plastic flow) as it reshapes the ice system due to that squeezing. Pressure sintering works differently than the prior described diffusion sintering mechanisms, which is shown in Figure 2.21. Here, the geometry and mass changes that ice grains undergo during these two types of sintering is indicated, with the main difference being that pressure sintering occurs from external pressure. This pressure, as with the plastic flow, may come from layers of ice on top of each other as well.

2.3.2. Sintering Stages

Sintering of ice proceeds through three stages: the initial, intermediate, and final stage. This sintering stage process is visualised in Figure 2.22 where the relative density of an ice sample is plotted against the sintering time. These stages are each defined by the evolution of the contact geometry between the ice grains and associated mass transport processes (Blackford, 2007). In the initial stage, necks form between adjacent grains due to mass movements through sintering processes such as vapour transport, surface diffusion, or grain boundary diffusion. This stage primarily increases the contact area without significant densification, and it determines the cohesion of a surface made out of ice grains. The intermediate stage begins when the neck radius becomes a significant fraction of the grain size. During this phase, pore spaces start to shrink and grains rearrange, causing moderate densification. Grain boundary and volume diffusion may become more prominent, especially in warmer regions or under localised pressure. The final stage is characterised by the closure of most pores and significant densification, approaching the behaviour of solid ice. At this stage, plastic deformation processes such as creep or grain boundary sliding may dominate, and the surface transitions from a porous aggregate to a more cohesive and structurally sound surface. Although these three stages have their distinct features, they often overlap in natural settings where temperature gradients and local mechanical stresses affect their progression (Blackford, 2007).

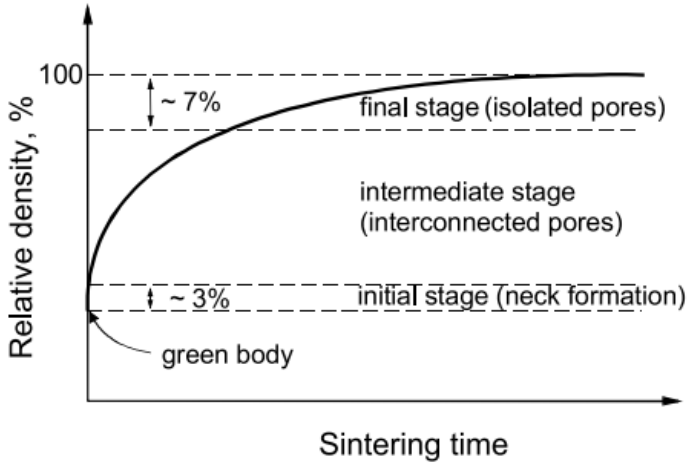

Figure 2.22: The evolution of the three sintering stages in terms of relative density against sintering time (Kang, 2004)

2.3.3. Ice Sintering on Enceladus

Having explored different types of ice sintering and in what environments they occur, this is still research that is mostly performed on ice sintering on Earth. Although sintering timescales in planetary environments has been researched already, planetary ice sintering is still unclear with its research being in the early stages (Dhaouadi et al., 2022). Based on the theoretical knowledge of ice sintering, although in Earth conditions, estimations can be done on expected sintering types on Enceladus based on its surface conditions. The current basic understanding of Enceladus surface includes the following aspects: cold temperatures on the surface and around 170 K to 220 K around the Tiger Stripes, low surface pressures, and geological activities such as cryovolcanism, tectonics, and tidal heating. From these conditions, several mass transport processes can be determined as most likely to occur on Enceladus' surface. The mass transport process of vapour transport is dominant for water ice at low temperatures

and pressures, and thus highly relevant for sintering on Enceladus (Blackford, 2007, Gundlach et al., 2018). Surface diffusion is thermally activated even at temperatures around 70K to 80K, although likely to proceed very slowly for a low activation energy (Blackford, 2007. Although possibly limited on Enceladus, grain boundary diffusion occurs at higher temperatures, which could be the case around the vents on Enceladus' surface where localised heating above 130K occurs. It is clear that vapour transport sintering would be the dominant type of ice sintering occuring on Enceladus, which is also the type of sintering that has been included in the few current studies regarding sintering and mechanical strength of icy moon surfaces (Gundlach et al., 2018, Choukroun et al., 2020).

2.3.4. Sintering Calculations

Calculating sintering timescales depends on the dominant mechanism and the sintering stage of the sample (Kang, 2004). In some cases it is possible to use a simple relation given by Molaro et al. (2019). This relation, given in Equation 2.2, is only valid for the first sintering stage. It is based on two power law parameters f and g, and the temperature of the ice. The power law parameters vary based on the size of the ice grains and can be found in the paper by Molaro et al. (2019). While Molaro et al. (2019) note the sintering timescale as τ, here t_s will be used instead as τ is already used to define the shear strength. It should also be noted that Equation 2.2 can only be used for temperatures below 205K for accurate results. Nevertheless, Equation 2.2 can be used as a ball-park for the sintering timescale of ice analogues.

$$t_s = fT^g \quad [\text{yr}] \quad (2.2)$$

More complex sintering calculations can be done based on the principles given by Kang (2004). Considering the most dominant sintering mechanism for ice in the first stage is vapour transport, or vapour diffusion, the sintering timescale calculation for vapour diffusion in the first stage will be described here based on the principles by Kang (2004), Hobbs (1974), and Swinkels and Ashby (1981). The neck growth between two ice grains due to vapour diffusion can be expressed as Equation 2.3 given by Kang (2004).

$$x^3 = \sqrt{\frac{18}{\pi}} \frac{p_\infty \gamma_s}{d^2} \left(\frac{M}{RT}\right)^{3/2} at = K_{Kang} t \quad [\text{m}^3] \quad (2.3)$$

In Equation 2.3, γ_s is the ice-vapour surface energy, d the molar density given by the molar weight M over the molar volume of ice V_m, R the universal gas constant (8.314 $\text{Jmol}^{-1}\text{K}^{-1}$), p_∞ the saturated vapour pressure (Pa) and T the temperature (K).

The sintering time for stage 1 can then be calculated by reshuffling Equation 2.3 to express t in terms of neck radius a and K_{Kang}. Calculations for stage 2 sintering become more complex and are left outside the scope of this thesis (Kang, 2004, Hobbs, 1974).

$$t_s = \frac{(a^3 - a_0^3)}{K_{vap}} \quad [\text{s}] \quad (2.4)$$

2.4. Strength Testing for Granular Surfaces

The type of strength testing that is done on a surface depends on the composition of the surface. In this section, strength testing of grainy or snowy surfaces are explored. The strength of a grainy surface is determined by evaluating how well the grains resist displacement under load. This is best determined in terms of shear and compressive strength for an ice grain surface. This is because these stress modes dominate how ice deforms and fails at a microscale, which is the case for the fine ice grain analogues that will be created.

2.4.1. Shear Strength

For both sand and ice grain surfaces, the shear strength is the most critical mechanical property. Shear strength is a key mechanical property that characterises a material's resistance to deformation or failure when subjected to shear stress, which acts parallel to the plane of interest. Generally, the shear stress can be calculated using the Mohr-Coulomb failure criterion for shear strength indicated in Equation 2.5, where τ is the shear strength, c the cohesion, σ the normal stress, and φ the internal friction angle (Labuz and Zang, 2012). The cohesive strength described here is the internal force that holds the

material together, resisting seperation under stress. The normal stress is the normal force (F) applied perpendicular to the surface divided by the area (A). This equation highlights that shear strength comes from both cohesive forces between particles and their frictional resistance.

$$\tau = c + \sigma \tan(\varphi) = c + \frac{F}{A}\tan(\varphi) \quad [\text{Pa}] \quad (2.5)$$

Although most commonly used for shear strength calculations, Equation 2.5 is not the only method to determine a material's shear strength. Empirical and experimental methods are often used as well, which use different procedures to get the shear strength of a material. A few experimental methods will be further explored in this section as experimental testing will be done in this thesis.

Shear Vane Test

To test the shear strength of an icy (mixture) analog surface a shear vane test can be done. Shear vane testing is a method used to determine the undrained shear strength of cohesive soils. It involves inserting a cylindrical vane with horizontal blades into the soil, then rotating it until the soil shears. The torque required for rotation is measured and used to calculate the soil's shear strength. This torque can be measured using either a torque sensor or a different measurement device that can measure the resistance encountered during rotation. While this method of shear strength testing is not found in many literature icy moon analogue applications, it has been used for some ice or snow surfaces on Earth or icy lunar regolith. The shear strength τ of the soil can then be determined using Equation 2.6, where the torque T is divided over the surface area. To calculate the surface area the diameter D and height H of the vane are used (Watson et al., 2000).

$$\tau = \frac{T}{\pi(\frac{D^2H}{2} + \frac{D^3}{6})} \quad [\text{kPa}] \quad (2.6)$$

Fall Cone Device

Another instrument that can be used to test the shear strength of fine-grained soils is the fall cone device, which is visualised in Figure 2.23. The device operates on the principle that the penetration depth of a cone into a soil sample under the influence of gravity is related to the material's resistance to deformation, or in other words, its shear strength. While the prior method, the shear vane test, makes use of torque to determine the shear strength, this method uses the soil's deformation upon impact. The device has a cone that is released instantaneously and follows a straight free fall into the soil (Verwaal and Mulder, 2017). The shear strength of the surface is then calculated using a constant c, gravity, the cone's mass, and the average cone penetration i which is measured by the device. This relation is indicated in Equation 2.7.

$$C_u = cg\frac{m}{i^2} \quad [\text{kPa}] \quad (2.7)$$

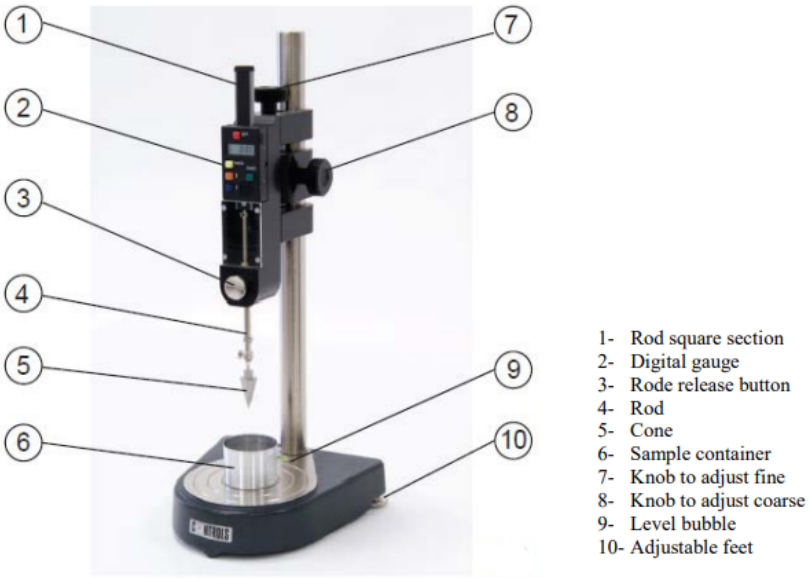

Figure 2.23: Fall-cone device including description of its parts (Verwaal and Mulder, 2017)

2.4.2. Compressive Strength

Just like shear strength, the compressive strength is a fundamental mechanic property that quantifies a material's ability to resist axial compressive loads without failure. It is defined as the maxmimum compressive stress a material can sustain before it yields or fails. Mathematically, the compressive strength σ_c is expressed as given in Equation 2.8, where F is the maximum applied load at failure and A is the original cross-sectional area of the specimen. This simple equation is usually expressed in further details depending on how the load or cross-sectional area are calculated. A common method to determine the compressive strength of a grainy surface in an experimental way is through some type of compression or penetration tests.

$$\sigma_c = \frac{F}{A} \quad [kPa] \quad (2.8)$$

Penetrometer

The compressive strength of a (granular) material can be tested using a penetrometer. This is a measuring instrument that detects the resistance of the material by breaking up the ice which can be translated to its compressive strength (Mantovani et al., 2016). Mantovani et al. (2016) performed penetration tests using a percussive cone penetrometer which allows for low reaction forces required to push the one into the surface in a low gravity environment. The strength of the soil (soil resistance R_s in kPa) can be determined using the percussive energy (E_{per} in Joules) and rate of penetration (R in m/s) of the cone penetrometer as indicated in Equation 2.10 (Zacny et al., 2010). The percussive energy, Equation 2.9, can be calculated using the kinetic energy (E_{kin}) and penetration work (W). The kinetic energy uses the mass of the impactor (m) and penetration velocity (v) and the penetration work (W) is the resistance force (F_{res}) multiplied by the penetration depth (d). The determined soil resistance can in turn be correlated with other strength parameters such as cohesion and friction angle.

$$E_{per} = E_{kin} + W = \frac{1}{2}mv^2 + F_{res}d \quad [J] \quad (2.9)$$

$$R_s = \frac{E}{R} \quad [kPa] \quad (2.10)$$

There are multiple factors to penetration testing in general that can affect the test results such as its size and shape, speed, and behaviour of the material prior to the penetration test (McCallum, 2014a). Whiteley and Dexter (1981) determined that the size of the penetrometer affects the stress results of the specimen. Although their tests were conducted on polar snow, the fundamental principles

of penetration resistance and stress distribution in materials under load apply across different types of material, including icy surfaces. This applies to scaling effects and the influence of penetrometer size, and can be used to assess compressive strength in icy materials.

2.5. Knowledge Gap

The study of the mechanical strength properties of Enceladus' surface due to the ice grain deposits from its plume has started to be of great interest because of future lander missions. Experimental studies are difficult to set-up however, both due to the low temperature and low pressure environment that is found on Enceladus as well as the unknown behaviour of the deposited ice particles from the plume. Strength testing for Enceladus' surface incorporates is both inter-particle strength and overall surface strength, which each have multiple complex aspects that need to be considered. Over the last several years, there are a few studies that have started to tackle these challenges.

The reason why it is crucial to understand and study the possible strength implications on Enceladus' surface is for future landing missions. Harmon et al. (2023) studied the possible effects of Enceladus' surface properties for future landing missions, including several optimal lander geometry designs. Landing is considered to take place in the SPT, close to the highest plume deposition, as this is the most valuable spot for the science objective of studying the plume material or subsurface ocean. This brings additional difficulties however, as it is uncertain what type of mechanical properties the surface may have due to the plume deposition. For that purpose, three lander footpad geometries (cone, disk, and hemisphere) were considered for varying sintering amount, grain size distribution, and surface slopes. From their tests, it was concluded that a hemisphere footpad geometry is best as it minimises slipping downhill on the expected slopes on Enceladus. Regarding landing location, Harmon et al. (2023) recommend to land in an area where stage 2 sintering occurs with a slope of maximum 15 °.

As of this moment, the focus of experimental studies of Encealdus' surface lies with the (strength of the) interaction of ice grains, which considers sintering and/or frictional contact as these are the most important factors for inter-particle cohesive strength. Multiple studies are researching the impact of sintering on Enceladus' surface strength, which includes studying the sintering (and sublimation) processes of small ice grains and their structural evolution through sintering (Gundlach et al., 2018, Molaro et al., 2019). The effect of sintering on the adhesive and resistance strength of these ice grains is studied as well (Gundlach et al., 2011, Gundlach and Blum, 2014, Musiolik and Wurm, 2019, Choukroun et al., 2020). The strength of fine ice grains is determined as well using the frictional contact between the grains. Gundlach et al. (2011) and Musiolik and Wurm (2019) study the collision properties and adhesive bonding of fine ice grains by investigating the critical rolling friction force of the particles.

Studies looking at a more macro-level scale, considering the overall surface strength rather than inter-particle strength, are still lacking. Choukroun et al. (2020) does perform strength tests on fine-grain porous ice analogues, studying the compressive strength of fine-grained crystalline ice with varying sintering times. Their focus is on the impact of sintering time on the strength of bulk ice grain analogues. Another important parameter for surface strength or resistance is the shear strength. Experiments measuring these parameters for an ice surface analogue have not yet been performed to a full extend. More importantly, all these tests have been done at atmospheric pressure. Under such conditions, gas accretes on the icy grains which could dramatically influence the strength of the material. The effect of vacuum on the strength of fine ice grain analogues has not been addresses before. This thesis will thus test the compressive and shear strength of an ice surface analogue considering a more macro-level rather than inter-particle strength in both atmospheric and vacuum pressure.

3

Experimental Set-up

This chapter describes the experimental set-up of all experiments that are done. This begins with determining the production method of ice grains in Section 3.1 and is followed by a brief explanation of the sample container used with its cooling mechanism. In Section 3.3, the test method used to test the mechanical strength of the ice analogues is described in detail from deciding the method to the physical experimental set-up in atmospheric and vacuum pressure.

3.1. Production of Ice Grains

The purpose of creating ice grains is to imitate the water-ice grains that fall back from Enceladus' plume onto its surface. It is therefore important to create water-ice grains that have a similar shape and size as to those found in the plume. It is likely that the ice grains produced on Enceladus are spherical, as the water droplets freeze when exiting the vents (Jabaud et al., 2024). A typical grain size for the slower particles that deposit close to the fractures is in the order of magnitude of tens to hundred micrometers (Jaumann et al., 2008). To create ice grains that resemble those depositing on Enceladus, liquid nitrogen is commonly used (Poch et al., 2016, Choukroun et al., 2020). The production set-up, production variables, and settings for creating the optimal grains that imitate the water-ice grains that fall back from the plume onto Enceladus are described in this section.

3.1.1. Production Set-Up

To produce the small ice grains, the set-up depicted in Figure 3.1 is used. Small spherical water-ice grains can be produced by spraying water into a dewar filled with liquid nitrogen (LN_2), where a dewar is a container which has a vacuum space between the outer wall and the inner container where cold liquids can be placed to remain cold. A close-up of how the water is sprayed into the liquid nitrogen is shown in Figure 3.2. The frozen water particles are then scooped out with a large spoon and loosely sifted in a sieve. Afterwards, the grains are measured for size (diameter) and amount of clumping that can be observed using both a regular and micro-camera. In this case, clumping indicates the icy grains freezing together before, or while, scooping out of the dewar. Through this method, the finest ice grains that can be produced have a diameter of up to 250 μm. Most grains probably have a smaller diameter, however, grain clumping and the micro-camera zoom level prevent this from being detectable.

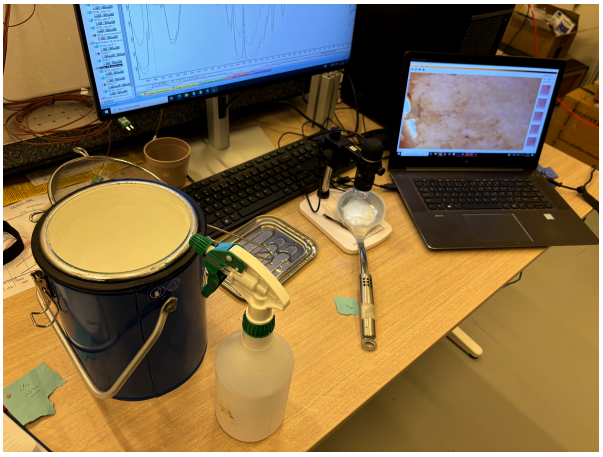

Figure 3.1: Production set-up for creating small icy grains using liquid nitrogen

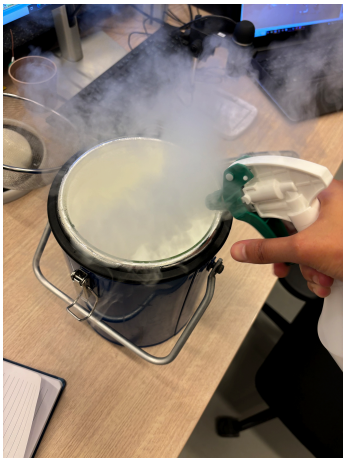

Figure 3.2: Close-up of the process of spraying water into the dewar

To measure the diameter of the grains, a digital USB microscope camera is used, which has a focus range between 0 and 40 mm. As can be seen on the right of Figure 3.1, this camera is attached to the computer. The images caught with the camera are visualised and treated with the MicroCapture Plus software. This software allows for clear images where the diameter of the grains can be measured inside the programme. The amount of clumping is estimated by visually analysing the produced grains both by the naked eye and through the microscope images.

3.1.2. Production Variables

There are three key variables that affect the size and clumping of icy grains during production: the spraying method, the spraying speed, and the frequency of scooping the grains from the dewar. Testing the effects of the spraying method, speed, and scooping intervals individually helps to find the optimal method of producing icy grains that imitate the grains in Enceladus' plume. Measuring these aspects also helps in ensuring the production of grains with consistent shapes and sizes, which is essential for creating reproducible results. The impact of each variable has been tested by varying its input while keeping the other two variables constant. The test specifics, results, and optimal outcome for each variable is stated in the following paragraphs.

Spraying Method

The spraying method used to spray water into the dewar mostly has an impact on the size of the produced grains. At this stage, only simple water spray bottles have been used at two opposite settings. Two water spray bottles were used; one with a smaller nozzle (green) and one with a larger nozzle (white). This was done to test if there is a difference between different nozzle sizes. The nozzle of the water spray bottle determined the setting that was used; either a loose nozzle setting with a direct spray or a tight nozzle setting resulting in a misty spray. The tests with the tight nozzle setting resulted in smaller grains than the tests with the loose nozzle setting with an average grain diameter of ∼0.2-1mm and ∼4-6mm respectively. The grains produced with the loose nozzle settings also resulted in more clumping compared to the tight nozzle setting. These differences in grain size and clumping between the two nozzle settings can be seen in Figure 3.3.

From the results in grain size, and the goal to obtain grains as small as possible, it was clear that the tightest nozzle setting is optimal. As the green bottle had a slightly tighter nozzle and was more comfortable to handle, this is the bottle that was used for all further tests. Additionally, it is important to note that the spraying should be done at an angle rather than straight from above the dewar, which causes the bottle to block after just a few sprays.

Scooping Intervals

Another variable to consider for grain production is the scooping intervals. To determine the effect of solely the scooping interval, a constant spraying speed of 10 times in 20 seconds was chosen. The scooping intervals were then tested at 0, 10, 20, and 30s. It was found that the longer the grains remain

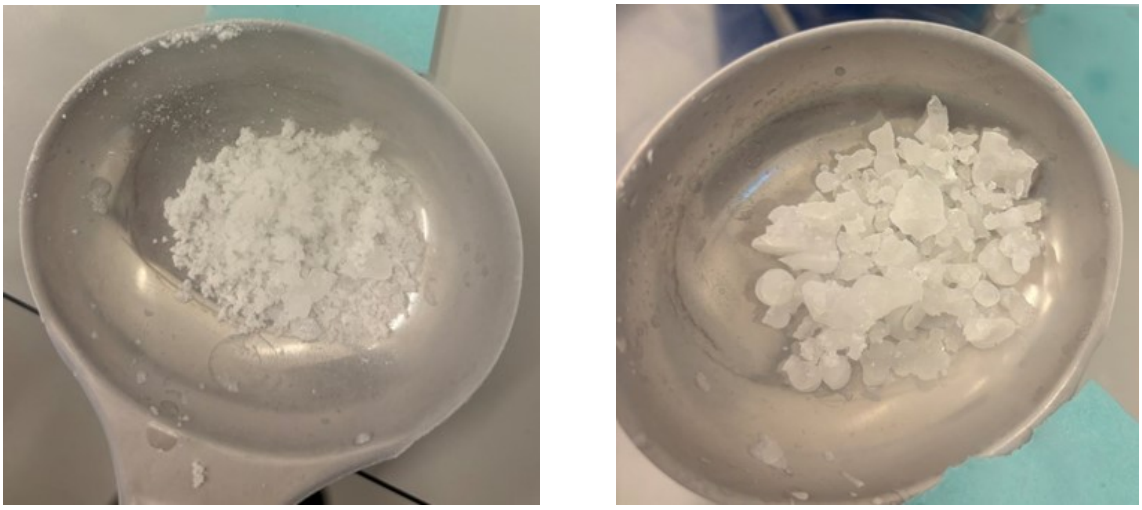

(a) Grains produced with tight nozzle setting

(b) Grains produced with loose nozzle setting

Figure 3.3: Grain size results for spraying with the tight nozzle setting (a) and loose nozzle setting (b) using the green water spray bottle

in the liquid nitrogen before being scooped out, the more clumping occurs. This was initially written down as bigger grains, but from later tests with images taken with the digital microscope it became clear that many of these 'bigger grains' were in fact smaller grains clumping together. As can be seen from the results in Table 3.1, it is best to scoop the grains out of the dewar immediately after finishing spraying.

Table 3.1: Grain size results from test with varying scooping intervals

Test #	Spraying speed	Scooping interval	Grain size
2_1	10x in 20s	0s	0.1-0.3 to 1mm for smaller grains, only few bigger grains of ∼2mm
2_2	10x in 20s	10s	0.1 to 1mm for smaller grains, 2/3mm for bigger grains
2_3	10x in 20s	20s	0.3-0.5mm for smaller grains, ∼3mm for bigger grains
2_4	10x in 20s	30s	0.3-0.5 to 1mm for smaller grains, ∼4-4.5mm for bigger grains

Spraying Speed

The third variable to consider for grain production is the spraying speed, which entails the number of sprays into the dewar within a given time frame. Therefore, within this one variable, there are two aspects being tested: the longest time during which can be sprayed before too much clumping occurs and how often can be sprayed within that time. For the first aspect, tests were done for a time frame of 10, 15, and 20s. When spraying for less than 10 seconds, the amount of produced ice grains was low, which would increase the overall production time significantly. It was therefore chosen to start this series of tests from 10 s onward. It was found that a longer time has a negligible effect on the grain size and that the amount of clumping can be controlled with the number of sprays that are done within that time frame. It was therefore chosen to do the tests within a time frame of 15s as this is the maximum at which spraying can be done easily without straining the hands. It is best to pick the maximum time frame at which this can be done to increase the number of particles that can be created in one go.

The second aspect, so how often to spray within 15s, was tested by spraying 10, 15, and 20 times within 15s. These tests were done twice, once scooping the grains immediately and once scooping the grains after 15s. It was found that spraying 20 times within 15s is almost impossible to do by hand. The difference in produced grain size and clumping was minimal between spraying 10 and 15 times, it is therefore best to spray 15 times in 15s for faster particle production.

3.1.3. Optimal Settings for Grain Production

Once all three variables of producing the icy grains had been tested for their optimal outcomes separately, a final test was done with these settings; to spray water 15 times in 15s into the liquid nitrogen using

the tightest nozzle setting and scooping the formed ice grains out immediately after those 15s. This final test was repeated five times and resulted each time in grains with a diameter of ∼0.1 to 2mm for the gross of the grains with a few bigger grains of up to ∼3mm. Some of these bigger grains were actually smaller grains clumping together, as can be seen in Figure 3.4, which shows some of the grains produced in the second test including measurements taken by the digital microscope.

After this procedure, using the optimal setting for grain production, another step can be taken to create even finer ice grains. This is done by putting the grains, created using the previously described method, into a sieve. Using a cooled pestle, the grains can then be crushed through the sieve to produce even finer grains. Since the grains are created using liquid nitrogen, they are cold enough to not melt during this process. This process results in finer ice grains with a diameter of ∼0.1 to 0.4mm. No grains bigger than this size are present due to the sieve. An image of these finer ice grains and their size is depicted in Figure 3.5. This process, including the sieve, is used for the creation of all ice analogues.

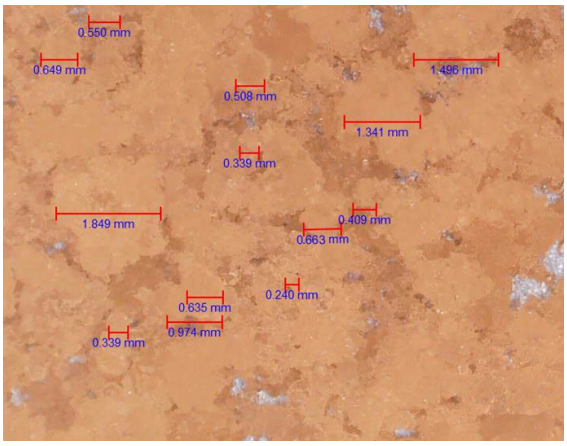

Figure 3.4: Grain size of ice grains produced using the optimal settings for grain production.

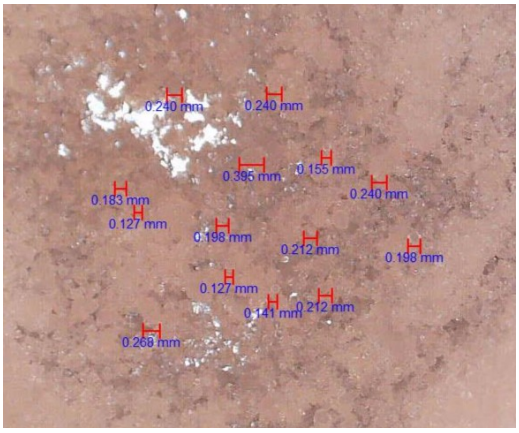

Figure 3.5: Grain size of the finer ice grains produced using the sieve and pestle.

3.2. Temperature Containment

The container with the icy grains needs to be insulated and kept as cold as possible for an extended period of time to ensure that the icy grains do not warm up significantly while strength testing takes place. This is especially important for the atmospheric strength tests that will occur, but is also relevant for the vacuum strength tests. It is therefore required to have a cooling mechanism that is sufficient to use inside of the vacuum chamber as well. The solution is relatively simple: a silicone layer with solid ice around the container, as depicted in Figure 3.6. The silicone layer allows the ice to expand as it freezes without destroying the container. This set-up with the silicone layer can be used in the vacuum chamber as well.

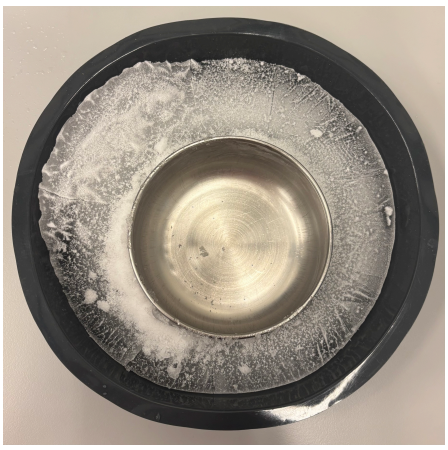

Figure 3.6: Cooling mechanism of the container by using a silicone layer with solid ice around.

3.3. Explanation of Test Method

The strength of the surface analogues can be both determined and expressed in different ways. As explained in Section 2.4, the most relevant parameters in terms of expressing the strength of a surface, are the shear and compressive strength. In this section, first several strength testing methods to determine the surface shear and compressive strength are evaluated, after which one is chosen to continue with. This is followed by a detailed description of the chosen method, both the physics behind the calculations and the experimental set-up. The verification and validation of the chosen method can be found in Chapter 4 *'Verification and Validation'*.

3.3.1. Trade-Off on Test Method

There are a few methods that can be used to determine the shear and compressive strength of an ice analogue. One major constraint however is that the method can be done inside a vacuum chamber. This means that it has to be relatively lightweight with a process that is near automatic or can be done manually from outside the vacuum chamber. Therefore, only methods suitable for use inside a vacuum chamber are considered. This results in the following methods:

- **Miniature direct shear box**
  A miniature direct shear box entails a small shear box that splits into two halves. This measures the shear strength by sliding one half of a sample sideways over the other while applying a known downward load.
- **Shear Vane**
  A shear vane test measures shear strength by rotating a small four-bladed vane inserted into the sample until it fails.
- **Penetrometer**
  A penetrometer measures strength by pressing a pointed or flat tip into the sample and measuring the resistance. This is used mostly to measure the compressive strength of a sample.
- **Manual fall-cone device**
  A manual fall-cone device is based on the fall-cone instrument. In this case, a weighted cone is dropped onto the sample through a tube and estimates the shear and compressive strength from how far the cone penetrates.

To decide between these methods, a trade-off table, Table 3.2, is made with the following parameters: instrument complexity, vacuum compatibility, suitability for fine ice grains, cost, and whether it measures shear strength, compressive strength, or both. From this trade-off, the manual fall-cone device comes out as the clear option to choose with a simple, suitable, and low cost design. It also allows for a measurement of both shear and compressive strength at the same time. This is a manually constructed instrument, however, which means that there are no prior results with this exact method to compare the results to. The method still comes out higher than the others due to its compatibility with the requirements of the vacuum chamber. To make sure the method is still valid, a few verification and validation tests have been done, which can be found in Chapter 4 *'Verification and Validation'*. For simplicity, the manual fall-cone device will be called CONE from here onward.

Method	Instrument complexity	Vacuum compatibility	Sample suitability	Strength measurement	Cost
Direct shear box	Medium	Low	High	Shear	Medium
Vane shear	Medium	Low	Medium	Shear	Medium
Penetrometer	Low	Medium	High	Compressive	Medium
Manual fall-cone	Low	High	High	Shear and compressive	Low

Table 3.2: Trade-off between test methods for ice analogue strength measurements

3.3.2. Physics behind CONE

This section describes the physics behind the CONE set-up. The CONE set-up itself is based on the combination of two concepts: the cone indentation method and the impact force of the cone. These two principles are used to derive the equations to go from the diameters measured during the test, indicated in Figure 3.7, to the shear and compressive strength of the samples. The next section will show the physical set-up of CONE and how the tests should be performed.

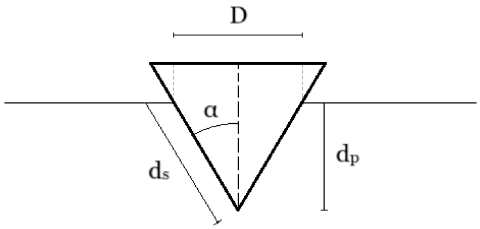

Figure 3.7: Schematic of cone indentation method including parameter indications.

Determination of Shear Strength

The cone indentation method provides an estimate of the shear strength of the sample (Ganneau et al., 2006, Zein, 2017). It involves inserting an inverted cone with an angle of 2α and mass m into the soil and measuring the resulting penetration depth h, hereafter renamed to d_p. When the angle α is small, the normal stress along the cone's surface becomes negligible relative to the shear stress. As a result, this method provides an estimate of the material's shear strength at failure. This can be calculated using Equation 3.1.

$$\tau = \frac{mg \cdot \cot(\alpha)}{\pi d_p^2} \quad [kPa] \quad (3.1)$$

To find the shear strength using Equation 3.1, the parameters α and d_p need to be determined first. Using the schematic for the cone indentation method depicted in Figure 3.7, the equations for α and d_p are formulated as given in Equation 3.2 and Equation 3.3 respectively. The parameters that need to be measured during the tests to calculate the shear strength are thus the side penetration depth d_s and diameter D of the indent.

$$\alpha = \arcsin\left(\frac{D}{2d_s}\right) \quad [°] \quad (3.2)$$

$$d_p = d_s \cdot \cos(\alpha) \quad [m] \quad (3.3)$$

Since the weight cannot be placed gently onto the surface once the vacuum chamber is turned on, a drop tower principle is used for the test. Another reasoning for using this principle is to increase the weight impacting the surface. The impact force with which the falling cone impacts the surface can be calculated using the work-energy principle, where the net work (W) done on an object is equal to its change in kinetic energy (E_{kin}), or $W = \Delta E_{kin}$. With $E_k$in known as $\frac{1}{2}mv^2$ and W defined as $F \cdot d$, the work-energy principle can be rewritten to give the impact force on the surface as shown in Equation 3.4 to Equation 3.6.

$$W = \Delta K = \frac{1}{2}mv_f^2 - \frac{1}{2}mv_i^2 \quad [J] \quad (3.4)$$

With the cone starting at zero velocity and undergoing a free fall under gravity, Equation 3.4 simply becomes:

$$W = \frac{1}{2}mv^2 = Fd \quad [J] \quad (3.5)$$

Here, F is the impact force in N and d the stopping distance in m. Using the relation for velocity from a certain height h, $v = \sqrt{2gh}$, Equation 3.5 can be rewritten and simplified to:

$$F = \frac{mv^2}{2d} = \frac{m(2gh)}{2d} = \frac{mgh}{d} \quad [N] \quad (3.6)$$

Substituting the impact force for the mg term in Equation 3.1 results in Equation 3.7, which gives the shear strength of the frozen samples using the CONE test set-up.

$$\tau = \frac{mgh \cdot \cot(\alpha)}{\pi d_p^3} \quad [kPa] \quad (3.7)$$

Determination of Compressive Strength

Continuing with the cone indentation with impact force method, a form of the surface's compressive strength can be determined as well. Through this method, it is possible to determine the local compressive stress at failure which is an estimate of the compressive strength of the surface under the cone indenter. This method is valid under the following assumptions, which is the case for the CONE set-up:

1. The cone is rigid compared to the surface sample.
2. Failure is dominated by compressive stresses under the cone.
3. The peak impact force F and maximum indentation depth d_p can be measured or calculated.
4. The contact area used in calculations come from the cone geometry.

At the moment of peak force, the mean contact pressure can be calculated, which is the compressive stress at failure if the sample indeed fails at that moment. From this moment onward this mean contact pressure will thus be named the compressive strength of the sample σ_c. The basic principle for calculation the compressive strength is given in Equation 3.8, where the impact force F is given already in Equation 3.6 and A is the contact or load-bearing area at failure.

$$\sigma_c = \frac{F}{A} \quad [\text{Pa}] \quad (3.8)$$

To determine the equation for A, the radius of contact at indentation depth a needs to be determined. This can be done easily using the schematic in Figure 3.7, giving the relation for a in Equation 3.9 using the cone indentation parameters already described in the shear strength section.

$$a(d_p) = d_p \tan(\alpha) = \frac{1}{2}D \quad [\text{m}] \quad (3.9)$$

Using Equation 3.9, the contact area A can be determined as written out in Equation 3.10.

$$A(d_p) = \pi a^2 = \pi d_p^2 \cdot \tan(\alpha)^2 = \frac{\pi}{4}D^2 \quad [\text{m}^2] \quad (3.10)$$

Using the relations for A and F given in Equation 3.10 and Equation 3.6 respectively, the compressive strength equation becomes Equation 3.11.

$$\sigma_c = \frac{F}{A(d_p)} = \frac{4F}{\pi D^2} = \frac{4mgh}{\pi d_p D^2} \quad [\text{Pa}] \quad (3.11)$$

3.3.3. Experimental Set-Up of CONE

The CONE instrument consists of a tube through which a cone is dropped onto the sample, as has been described already. The details of this method, how it is set-up and what principles it is based on are described in the prior section. The purpose of this section is to show the physical set-up. This is done first by determining the specifications of the test parts and followed by the experimental set-up of the CONE test for atmospheric and vacuum pressure.

Determining Test Parts

In order to do all the required strength tests, it is necessary to first determine the right test parts. Therefore, a comparison is done between different tube heights of 10 cm and 15 cm and cone weights of 0.0837 kg and 0.268 kg to see if this impacts the results. These tubes and cones are depicted in Figure 3.8.

A series of three tests is done at -5, -10 and -15 ° C with all four tubes. These tests are done to determine if there are differences in results between the two cones as well as using different heights. The results from these tests are given in Table 3.3 with the measured parameters d_s and D and the calculated yield strength τ. It can be seen that two results are given with no yield strength. This is due to the fact that the equation to calculate the yield strength is invalid for $2d_s \leq D$. It is preferred to use a cone with a sharper tip, as is the rule with a regular fall-cone-device (Verwaal and Mulder, 2017), which means that cone 1 is preferred over cone 2 for this requirement. This could also explain the small variation in results between tube # 2 and tube #4.

Looking at the tests with cone #1, the results between tube #1 and tube #2 are different. It shows that the obtained shear strength from the 10 cm tube is higher than that of the 15 cm tube. This shows

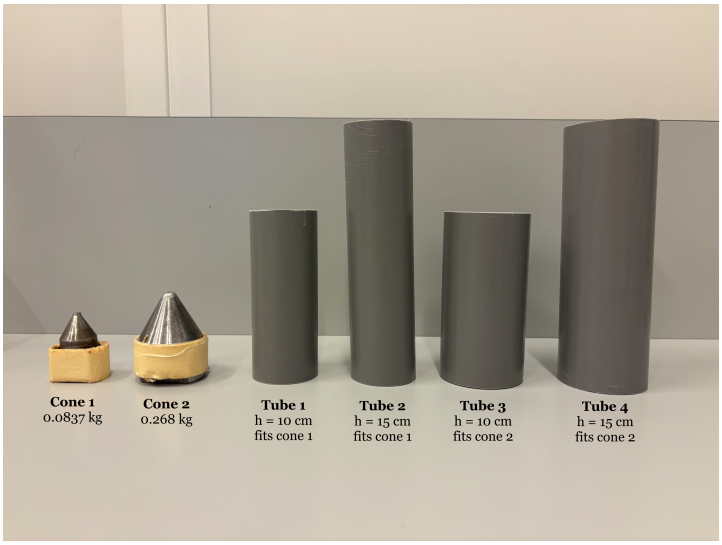

Figure 3.8: The cones and tubes used to set-up the manually constructed fall cone test.

that the impact from the cone at a height of 15 cm is too much. The higher impact energy can crush or fracture the ice bonds between the sand, damaging the surface rather than shearing it (Ma et al., 2018). This results in the calculated shear strength being lower than the actual shear strength. The 10 cm tube, combined with cone #1, is thus most accurate to use. After these results, this test was briefly repeated with a 5 cm tube. This showed that with a 5 cm tube no true indent was made, so the decision was made to continue the tests with the 10 cm tube. The verification of the shear strength results, with more testing, is described in Chapter 4.

	Temperature = -5 °C			**Temperature = -10 °C**			**Temperature = -15 °C**		
Tube	d_s **[mm]**	**D [mm]**	τ **[kPa]**	d_s **[mm]**	**D [mm]**	τ **[kPa]**	d_s **[mm]**	**D [mm]**	τ **[kPa]**
1	3.5	4	1583.1	2.5	4	5804.7	2	3.5	15921.5
2	4	5	1607.5	5	5.5	817.1	3.5	4.5	2422.8
3	3	8	-	2.7	6	-	3.7	6.5	8242.8
4	6	9	1773.2	7	9.5	1000.8	5	8.5	4262.4

Table 3.3: Shear strength of frozen quartz sand using two different cones and heights for -5 °C, -10 °C, and -15 °C.

CONE Set-Up in Atmospheric Pressure

The CONE set-up in atmospheric pressure is very straightforward. The 10 cm tube was simply held just above the surface of the sample. The cone, also hand-held, was then dropped from just above the 10 cm tube. This would leave a cone-shaped indent in the sample, after which the d_s and D parameters shown in Figure 3.7 were measured from which the shear and compressive strength can be calculated. This step is repeated for as many times as it fit in the container, ranging from 5 to 11 measurements depending on the strength of the sample. Each of these measurements are taken together as one data point, so each data point is the result of one test done.

CONE Set-Up in the Vacuum Chamber

While the CONE set-up in atmospheric pressure is relatively straightforward, the set-up in the vacuum chamber requires a bit more effort. The vacuum chamber used during the experiments is the PISCES vacuum chamber of the Delft Planetary Labs. This is an 80x80x80 cm chamber, pictured in Figure 3.10, that can go to pressures as low as 10^{-1} mbar with the help of a cold finger and even lower to $3 \cdot 10^{-5}$ mbar using a turbo-pump. To perform the strength tests using CONE without access to the chamber as vacuum is turned on requires a semi-automatic process. This is done by using a magnet as a release system for the cone while both the sample container and tube are held up by a tripod, as is indicated in Figure 3.11. A schematic of the same set-up is given in Figure 3.9.

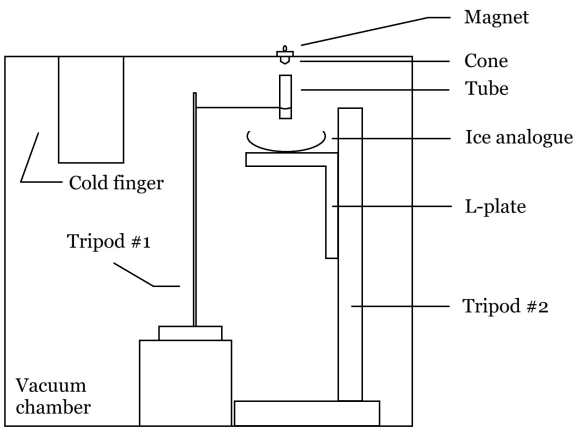

Figure 3.9: Schematic of the CONE method set-up in the vacuum chamber.

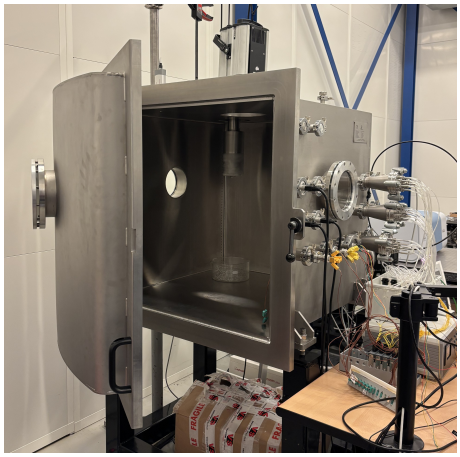

Figure 3.10: The PISCES vacuum chamber of the Delft Planetary Labs used for the ice analogue strength testing in vacuum.

The tests are done in multiple sessions, with one session consisting of three measurements for both the -25 °C and -80 °C ice analogues. The pumps of the vacuum chamber are turned on before the first measurement and only switched off after the last measurement has been done, however the vacuum chamber is pumped down and vented again before and after each measurements. Each time the vacuum chamber is pumping down again, some liquid nitrogen is poured into the cold finger again as well. After 20 minutes of pumping down, when the vacuum chamber has reached its lowest pressure, the magnet is taken off the vacuum chamber and the cone drops onto the sample. Immediately afterwards, the vacuum chamber is vented and the ice analogue is taken out to take the d_s and D measurements. Once that has been done, the sample goes back into the vacuum chamber for another measurement at a different spot on the sample. For each measurement the temperature of the sample is taken as well by inserting a thermocouple into a prepared hole in the sample.

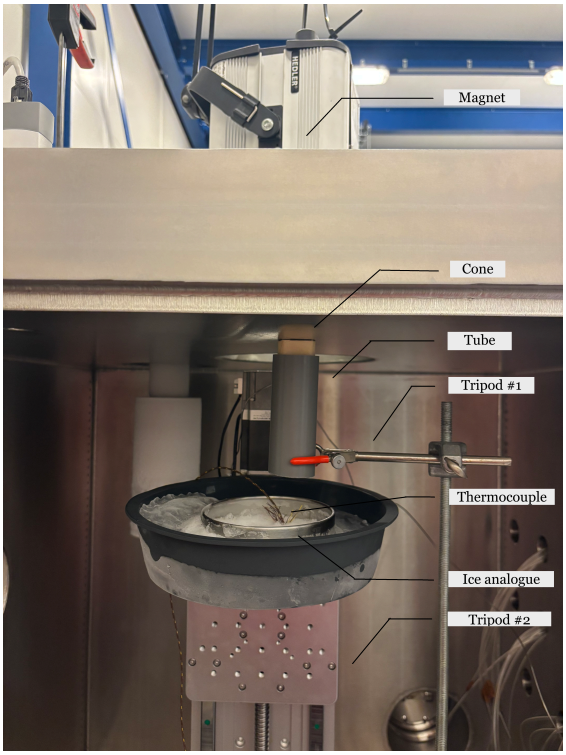

Figure 3.11: The CONE set-up inside the vacuum chamber.

4

Verification & Validation

This chapter consists of the validation of the use of quartz sand as a control material and the verification of using the CONE device as a method to test the shear and compressive strength of the ice analogues. Section 4.1 validates whether the chosen control material indeed behaves as expected from literature. Section 4.2 checks whether the CONE method provides results that are consistent with cone indentation strengths in literature.

4.1. Validation of Control Material

In the preparatory experiments of this thesis, quartz sand is used instead of fine ice grains. The reasoning behind using quartz sand as a control material are described in this section. This is followed by a description of the tools that are used to validate this decision, which measure the shear strength and compressive strength at failure. Then finally, the results of these tests are described and compared to similar tests done in the literature.

4.1.1. Quartz sand as Control Material

There are several reasons for using a control material to both evaluate test methods and verify them. Using the fine ice grains made by spraying water into liquid nitrogen is a time consuming process and would thus take too much time for the number of tests that need to be done for the evaluation or verification of the tests. Additionally, there is no one range for the strength properties of an ice grain surface as the composition is variable and generally not many strength tests have been done on a granular fine ice surface. It is therefore best to choose a control material that is less time consuming to produce and for which the strength range is known. To decide which material is best to use as a control material, the following requirements are taken into account:

1. The shear strength range is known for the material in a frozen state.
2. The compressive strength range is known for the material in a frozen state.
3. The material is granular with a grain size up to 1mm.
4. The material is cost-effective and readily available.

There are a few materials that can be considered; quartz sand, sintered glass beads, and granulated sugar. These are all granular materials with the desired grain size. In Table 4.1, the cost, known shear strength and known compressive strength are indicated for each of these three materials. From this trade-off table, quartz sand is the most desirable outcome and has thus been chosen to use as the control material.

Material	Cost	Shear strength	Compressive strength
Quartz sand	Low	Yes	Yes
Sintered glass beads	High	Limited	Limited
Granulated sugar	Low	Limited	Limited

Table 4.1: Trade-off for the control material

The validation test is done by placing quartz sand in a container, which is then compacted before placed in the freezer. After waiting at least 24 hours to ensure the sample is completely frozen, it is taken out of the freezer. Doing everything as fast as possible, the temperature sensor is placed in the prepared hole, visualised in Figure 4.1. The ice layer around the container helps to keep the sample cool for longer. The pocket tests can then be done using the two pocket tools described in the next section.

Figure 4.1: Set-up of the frozen quartz sand sample with a layer of ice around the container. The sample has a hole in which the thermal couple is placed.

4.1.2. Validation Tools

The validation of the control material is done using two pocket tools, which are borrowed from the Geo-engineering lab of Civil Engineering at TU Delft. The shear strength is determined using a pocket shear vane test and the compressive strength is determined using a pocket penetrometer. These pocket tools are used since they can easily be brought to the Delft Planetary Lab where the experiments are done. The results from these pocket tools are compared to literature using similar materials and tools.

Pocket Shear Vane Test

The pocket shear vane test is, in principle, a simpler version of the shear vane test described in Subsection 2.4.1. The pocket instrument is generally used in geo-engineering to bring to surfaces where the full shear vane test is difficult be brought to due to the terrain. In this case, the reason for using the pocket test over the shear vane test is twofold. The available shear vane test is located too far from where the samples are kept in the freezer and cannot be brought to the Delft Planetary Labs. Bringing the samples to the shear vane test is not possible while keeping them frozen. The second reason is that the pocket instrument can give inspiration for the creation of a test method suitable for operation within the vacuum chamber. The pocket shear vane test that is used in these tests is depicted in Figure 4.2 and Figure 4.3 indicating the front and top view of the instrument respectively.

The pocket shear vane test is performed by pressing the instrument into the surface until the blades are in the surface. Then torque is applied by twisting the orange part at the top of the pocket instrument. This is twisted until the surface fails, at which point the range from start until failure can be read of from the top of the instrument as indicated in Figure 4.3. This value is the shear strength in kg/cm^2, which gives the shear strength in kPa when multiplied by 98.0665.

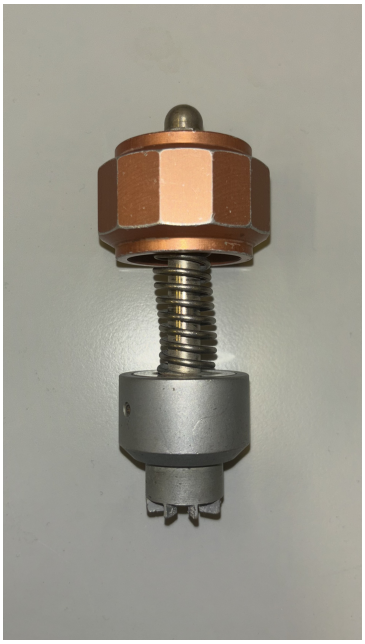

Figure 4.2: Front view of the pocket shear vane test instrument.

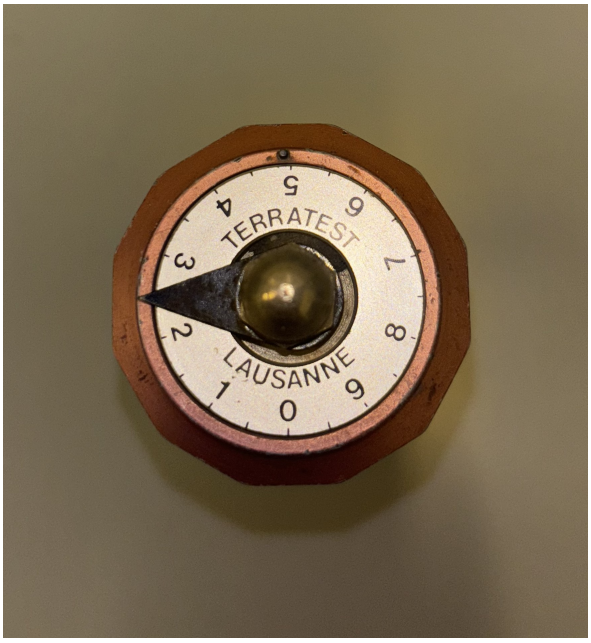

Figure 4.3: Top view of the pocket shear vane test instrument indicating the shear strength values.

Pocket Penetrometer

A pocket penetrometer is a simple handheld device that can be used to easily estimate the unconfined compressive strength of a cohesive soil. It consists of a spring-loaded piston housed in a metal barrel with a calibrated scale in kg/cm^2 that displays the resistance when the piston is pressed into the soil. An image of the pocket penetrometer is shown in Figure 4.4. This pocket penetrometer can indicate a maximum compressive strength of 450 kPa. To use the pocket penetrometer, the flat end of the piston is pressed into the soil, and the reading can be taken directly from the indicator ring. This tool is used as a simple estimate of the compressive strength of the frozen quartz sand analogues.

Figure 4.4: Pocket penetrometer tool used to measure the compressive strength of a soil.

4.1.3. Validation Results

The quartz sand is tested for both shear strength and compressive strength using the pocket tools. For smaller samples of frozen quartz sand around -10 to -5°C the shear strength and compressive strength range from 150-400 kPa and 300-800 kPa in literature respectively (Kim and Lee, 2020, Parameswaran, 1978, Parameswaran, 1980). It is important to note that these values are specifically for obtaining the shear strength from a (pocket) shear vane test and the compressive strength from a (pocket) penetrometer. The validation tests are done at these temperature because the freezer available at the time had a temperature of -15 to -5 °C.

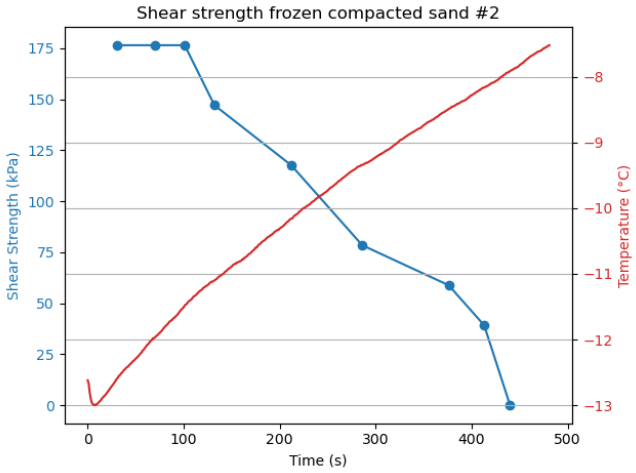

Figure 4.5: Shear strength of frozen compacted quartz sand with temperature against time, test #2

This test is repeated four times for both the shear strength and compressive strength. For the maximum shear strength this resulted in a strength range of 80-200 kPa between the temperatures of -15 to -5 °C. This is partly under and partly within the shear strength range of 150-400 kPa from literature. The reason why the lower range of the tested material is below that in the literature is because the sample warms up quickly, as can be seen, for example, in the shear strength plot of test number 2 in Figure 4.5. The plots of the other tests can be found in Appendix B. Another factor contributing to the difference in shear strength range is that the temperature is measured in one spot, indicated in Figure 4.1, which gives a good indication of the material's temperature although it can vary locally. Nevertheless, these results indicate that the obtained shear strength values at which failure occurs are in a similar range to those in the literature validating the control material for the shear strength aspect.

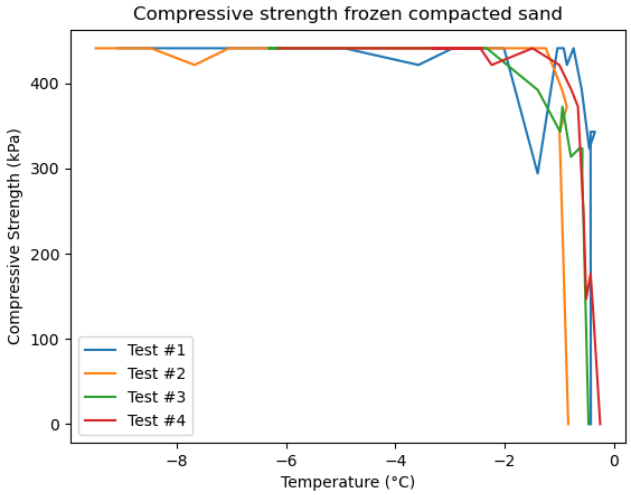

Figure 4.6: The combined compressive strength measurements on frozen compacted sand of four tests.

Compressive strength measurements obtained in similar tests yield values between 300-800 kPa over the relevant temperature ranges (Kim and Lee, 2020, Parameswaran, 1980). Largely, these exceed the maximum compressive strength the pocket penetrometer can measure of 450 kPa, and so it is not possible to validate the material compressive strength directly. Instead, one can make use of the fact that the compressive strength is temperature dependent: at temperatures just below freezing, the compressive strength should rapidly fall into the regime that the penetrometer can actually measure. Figure 4.6 shows that this behaviour is replicated in the sample. With this, it is shown that the frozen quartz sand behaves as expected in terms of both compressive and shear strength.

4.2. Verification of CONE

To ensure that the results of the analogue strength tests are valid, it is necessary to verify the CONE device that will be used. The complete description of this method is described in Section 3.3. This section verifies this method using the quartz sand as a control material by comparing it to literature. It was planned to compare it to tests done using the fall cone instrument at the geo-engineering lab of the Civil Engineering faculty as well, however this was unsuccessful. The available freezer unfortunately only froze the samples up to -5°C, which made the tests invalid as the sand had not frozen together. The CONE method is thus verified only by comparison to literature and the trends seen in the results.

As it was decided that the combination of cone 1 with the 10cm tube was best to use, this is the set combination for these quartz sand tests. These tests entail the use of the CONE test on the quartz sand control material. The purpose of these tests is to validate the CONE test by comparing the results of these quartz sand tests with literature.

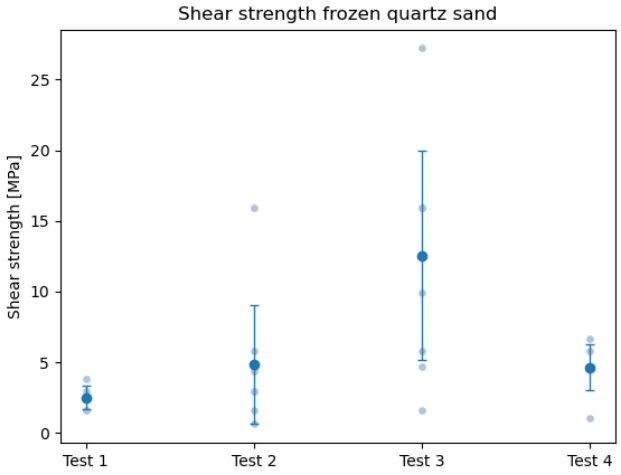

Figure 4.7: The four shear strength measurements on frozen quartz sand using the CONE device.

Four tests were done with each test giving 5 to 9 data points. The shear strength results are shown in Figure 4.7. From this graph it can be noted that the shear strength ranges from ∼1 to ∼20 MPa at temperatures between -13 °C and -5 °C with one outlier at 27 MPa. Although not indicated in this graph, the data shows that shear strength increases with decreasing temperature, which is known for frozen granular materials (McCallum, 2014b). While most literature indicates that the shear strength of frozen quartz sand at these temperatures goes up to ∼20 MPa (Parameswaran and Jones, 1981, Mayne, 2007), McCallum (2014b) does find up to ∼30 MPa tip resistance for frozen sands using a cone penetration method.

To clarify the differences in shear strength magnitude between this test and the pocket shear vane test described earlier, it should be noted that these tests test a different type of shear strength. A shear vane test gives low strength values because it mainly causes the frozen sand to slip and break along weak paths, so it never uses the full strength of the ice-bonded grains. A cone indentation test pushes straight into the material and squeezes it, forcing the frozen sand to resist much more strongly, which leads to much higher strength values. These differences are also mentioned in Chapter 3, but to clarify, the

cone indentation method gives a more reproducible measure of the material's resistance to real-world loading which is eventually the application of these tests. Overall, the shear strength results indicated in Figure 4.7 are in line with shear strength values given for frozen quartz sand in literature between 1 and ∼20 MPa (Parameswaran and Jones, 1981, Mayne, 2007), McCallum (2014b)). The obtained strength values from the CONE test with the frozen quartz sand are repeatable and comparable to available literature, which validates the method for determining the strength of the ice analogues.

5

Mechanical Properties of the Ice Analogues

This chapter shows the results of the mechanical strength tests done on the ice analogues. This starts with a general description of the strength values obtained in Section 5.1, and is followed by the results of different parameters: 1) the time the ice analogues spend in the freezer, referred to as freezer time, 2) the temperature at which the ice analogues are left in the freezer, referred to as origin temperature, and 3) the different pressures at which the tests are done, referred to as pressure effects. The freezer time, origin temperature, and pressure effects on the ice analogues strength are given in Section 5.2, Section 5.3, and Section 5.4 respectively. Each results section is immediately followed by an interpretation of those results. Section 5.5 briefly summarises the results from each prior section to give one complete picture. Chapter 6 will then provide a discussion of these results in the context of future missions to Enceladus.

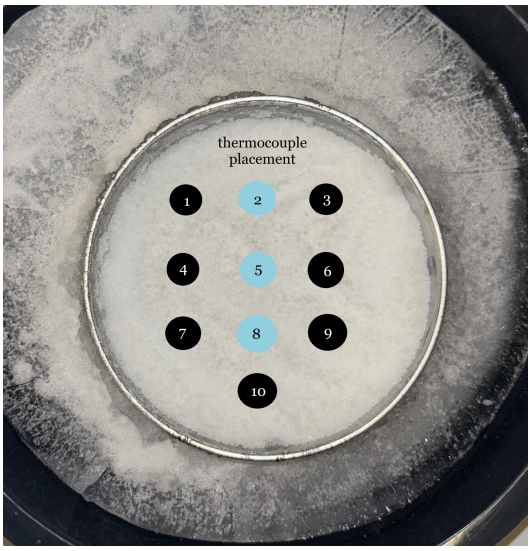

(a) Order of measurements with an indication between the inner (blue) measurements and outer (black) measurements depending on the sample.

(b) An example of what the measurements look like on an ice analogue using the CONE method. This is a -80 °C analogue with 7 measurements.

Figure 5.1: A schematic indication of how the measurements are taken during a test (a) and an example of actual measurements on an ice analogue (b).

5.1. Mechanical Strength of the Ice Analogues

The tests performed to measure the shear and compressive strength of the ice analogues were done using the CONE method in four different environments: in atmospheric (1 bar) and vacuum (0.1 mbar)

pressure with an origin temperature of -25 °C and -80 °C. The shear and compressive strength of each test were calculated following the CONE method described in Section 3.3. Before diving into the general mechanical strength values that were obtained, the test set-up and outline of the results is given.

Besides the CONE method itself, it should be noted how the measurements were taken during a test and what each strength data point indicates. Figure 5.1 shows both a schematic indication (Figure 5.1a) and a physical example (Figure 5.1b) of the test measurements. Figure 5.1b shows a test in which 7 measurements were taken. The mean of these 7 measurements gives one strength data point for that test. The number of measurements done per test depends on how strong the analogue is, and thus how deep the cone penetrates the analogue. Over all tests this number of measurements ranges between 5 and 11 measurements. Figure 5.1a shows a schematic indicating the thermocouple location at the top of the ice analogue and 10 possible measurements either blue or black in circles. During some tests, especially the ones done with a longer freezer time, a difference could be observed between the strength measurements done in the middle (blue in Figure 5.1a) and outer edge (black in Figure 5.1a) of the ice analogue. This result is elaborated upon in the section about the effect of freezer time on ice analogue strength.

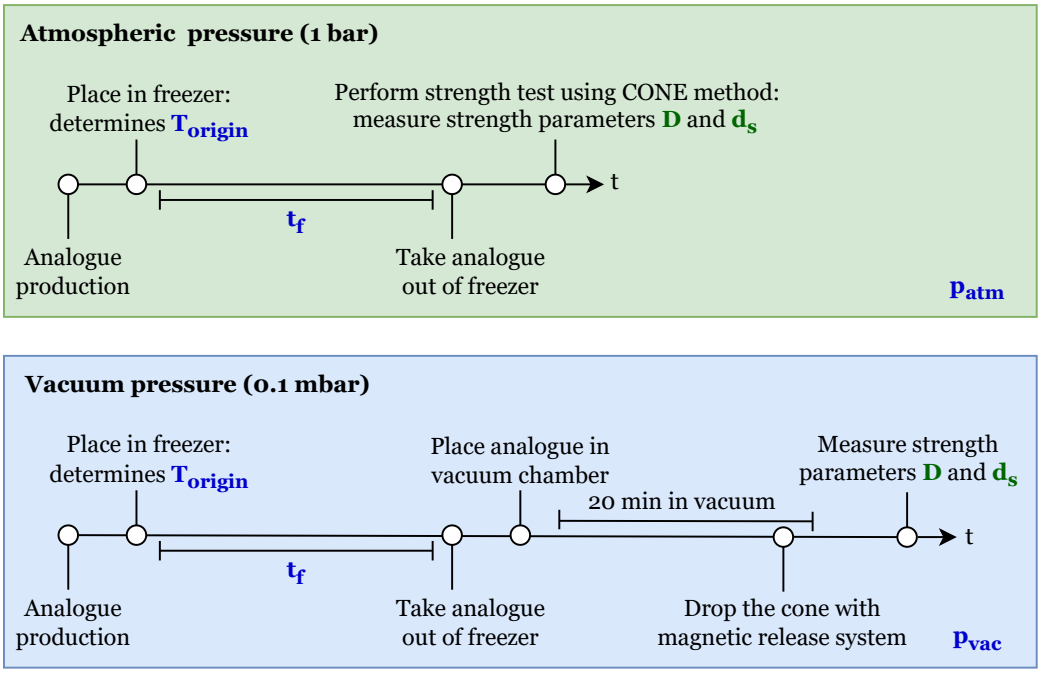

Figure 5.2: A schematic indicating the timeline for the atmospheric tests (top) and vacuum tests (bottom). This includes the input parameters T_{origin}, t_f, and p indicated in blue, the test steps, and the output parameters d_s and D indicated in green.

To have a clearer idea about the procedure of the performed tests, an outline of these tests is given in Figure 5.2. The upper timeline in Figure 5.2 shows the timeline of the tests done in atmospheric pressure. First, the ice analogue is produced after which it is placed in either the -25 °C or -80 °C freezer. This determines the origin temperature of the ice analogue. Afterwards the analogue is left in the freezer for a certain amount of time, the freezer time t_f, before it is taken out for the strength measurements. This entails using the CONE method to get the required parameters d_s and D to calculate the shear τ and compressive σ_c strength of the ice analogue. The bottom timeline shows the test process for the vacuum pressure tests. Up to the strength tests itself the process is identical to the atmospheric pressure tests. After the ice analogue has been taken out of the freezer it is placed in the vacuum chamber. When the analogue has spent 20 minutes in vacuum, the cone is dropped using the magnetic release system. The required strength measurements are then taken once the vacuum chamber has vented, after which the analogue is rotated and placed back into the vacuum chamber to be able to take three measurements during each test.

The results of these tests are given in this chapter by first giving the shear and compressive strength results of the ice analogues in atmospheric pressure and comparing these to other experimental work in Subsection 5.1.1 and Subsection 5.1.2 respectively. This is followed by the results of the effect of freezer time on the ice analogue strength in atmospheric pressure for the -25 °C analogues in Section 5.2. The effect of the origin temperature is then given afterwards in Section 5.3 by including the results of the -80 °C analogues in atmospheric pressure and comparing them to the -25 °C analogue results. Then in Section 5.4 the effect of vacuum pressure compared to atmospheric pressure on the strength of the ice analogues is given. These results are then discussed in the context of Enceladus' surface in Chapter 6.

5.1.1. Shear Strength

The shear strength τ of the ice analogues, calculated using Equation 3.7 in Section 3.3 *Explanation of Test Method*, indicates the shear strength at which the ice analogues fail. Using the CONE method, the shear strength can be determined using the resistance of the analogues to cone penetration. It is this load-displacement response that gives the relation for the shear strength of the surface. Considering all four environments at the same time for now, the shear strength range that was found is between 10 and 220 KPa for ice analogues with a temperature of -25 °C and -80 °C. An example of the obtained shear strength measurements of one test for both a -25 °C and -80 °C is presented in Figure 5.3 showing the shear strength against the temperature of the sample at which the measurements were taken. These two plots show the variation in strength between the inner and outer edge of the sample as indicated in Figure 5.1a. The peaks in Figure 5.3 are taken at the outer edge, pictured black in Figure 5.1a, and the lower strength measurements are taken in the inner edge, picture in blue in Figure 5.1a. This is described in more detail in the next section. These measurements become one mean data point with a spread of all measurements in the plots used later in this chapter to describe different effects on the analogue strength.

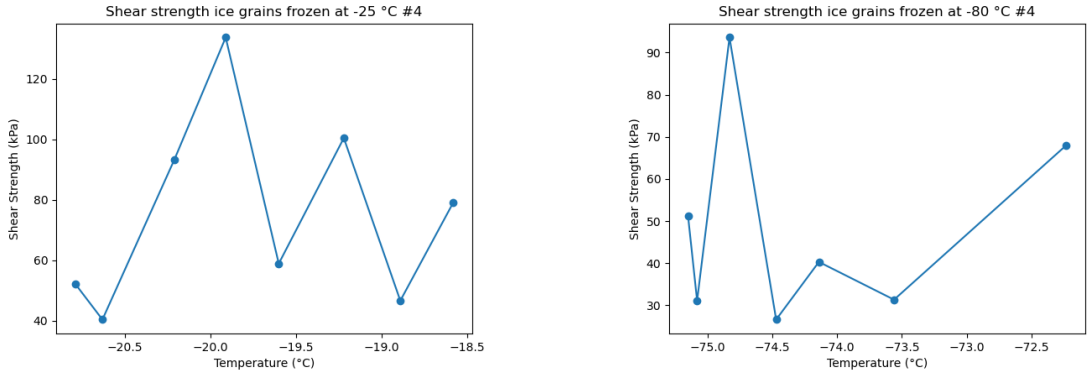

(a) Shear strength of -25 °C analogue

(b) Shear strength of -80 °C analogue

Figure 5.3: The shear strength of a -25 °C (a) and -80 °C (b) analogue tested in atmospheric pressure.

While not much research has been done on the shear strength of fine ice grains at temperatures lower than -15 °C, a comparison with warmer temperatures can be made. Frederking et al. (1988) studied the shear strength of ice at -10°C. Using a simple beam theory to test for shear strength, they found an average shear strength of 600 kPa for their samples. Considering the fact that they tested their ice grains at a warmer temperature, their obtained shear strength is comparable to that found in this work. A warmer, yet still freezing, ice grain temperature results in stronger samples as experienced in this work, which is described in more detail in Section 5.2. The shear strength magnitude is in a similar ballpark of a few hundred kPa, which gives reason to expect that the strength difference comes simply from the temperature difference between the samples. The obtained shear strength of the ice analogues using the CONE method thus follows a similar trend to other shear strength studies.

5.1.2. Compressive Strength

The compressive strength σ_c of the ice analogues is calculated using Equation 3.11 in Section 3.3 *Explanation of Test Method*. This gives the local compressive strength of the ice analogue at the locations of the measurements. Averaged out to one data point, the local compressive strength of the

ice grain surface is determined within a range of 10 to 475 kPa for temperatures of -25 °C and -80 °C. Comparing this strength range to the shear strength range, it can be seen that $\sigma_c \geq \tau$. It is typical for materials, or surfaces, to exhibit a higher compressive strength than shear strength because compression acts uniformly through a material, requiring greater stress to cause deformation. In contrast, shear loading produces sliding along internal planes, which leads to failure at lower stress levels.

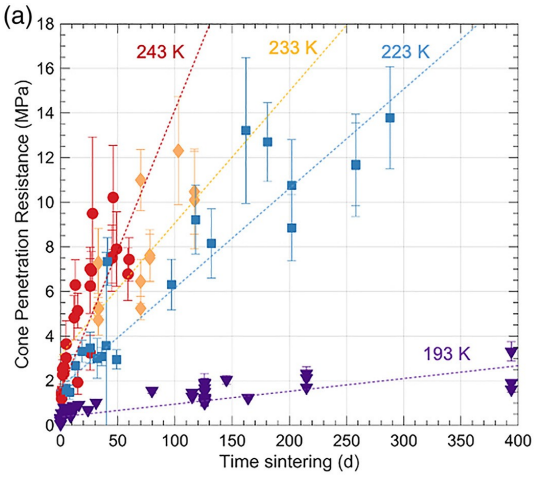

Figure 5.4: Compressive strength evolution against sintering time for ice analogues with an origin temperature of 193 K to 243 K measured by Choukroun et al. (2020).

Choukroun et al. (2020) tested the compressive strength of fine ice grain analogues with temperatures ranging from 193 K to 243 K including sintering. Their tests were only performed in atmospheric pressure, so no comparison can be made for the vacuum pressure results. Having said that, Figure 5.4 shows the strength results against sintering time in atmospheric pressure measured by Choukroun et al. (2020). Only the very first measurements, up to ∼9 days, of Figure 5.4 can be compared to the results obtained in this study. Their range seems to be 1-2MPa for their 243K samples and 0-0.5MPa for their 193K samples. While their strength indications are higher, they do follow a similar trend to the compressive strength results from this study indicated in Figure 5.5. This graph is described in more detail in Section 5.2. The reason for this difference in strength values could be the grain size of the analogues. While the finest ice grains that could be produced in this thesis are up to 100μm, Choukroun et al. (2020) used ice grains with a mean diameter of 12μm. The finer the grains, the higher the surface strength becomes. This grain size difference can thus well explain the compressive strength differences between the ice analogues, especially since the results do show a similar trend in strength increase over freezer time.

Mechanical Strength Results

- The shear strength of the ice analogues ranges between 10 and 220 kPa for both -25 °C and -80 ° C analogues combined. These results are in a similar ballpark to other experimental studies.
- The compressive strength of the ice analogues ranges between 10 and 475 kPa. This range follows a similar, but increased, trend compared to the shear strength as expected.
- There is a difference in strength between the measurements taken on the inner and outer edge of the samples. The outer edge of the analogues is stronger than the middle.

5.2. Effect of Freezer Time on Ice Analogue Strength

This section describes the effect of freezer time on the shear and compressive strength measurements of the ice analogues. Here, freezer time t_f indicates the amount of time an ice analogue has spent in a freezer between production of the sample to taking it out of the freezer to perform the strength tests. As was mentioned before, in this section only the -25 °C analogue in atmospheric pressure is considered.

The hypothesis is that a longer freezer time increases both the shear and compressive strength of the ice analogues.

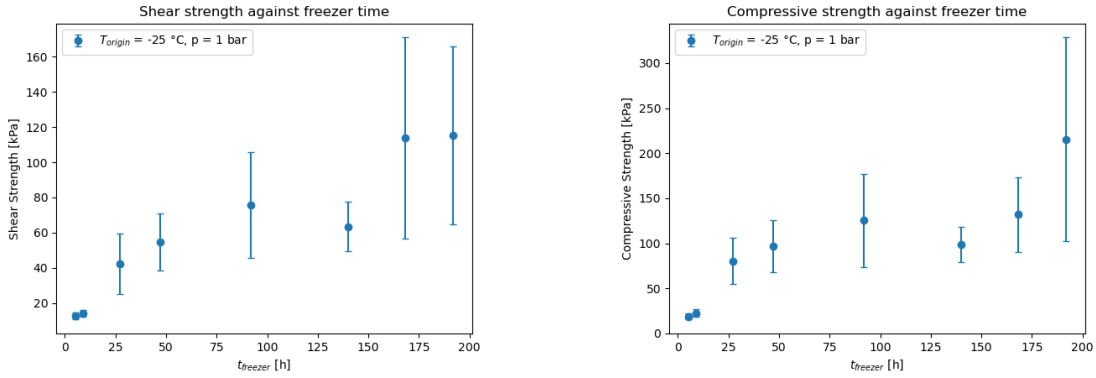

(a) Shear strength

(b) Compressive strength

Figure 5.5: Shear (a) and compressive (b) strength of the -25 °C ice analogues against freezer time in atmospheric pressure.

To study the effect of freezer time on the strength properties of the ice analogues, the samples were left in the freezer for a range between 2 and 200 hours. The tests were done at regular intervals within this range whenever possible. This range was chosen due to both time and lab availability constraints. The results of these tests for the -25 °C analogues in atmospheric pressure were plotted for both the shear and compressive strength against the freezer time, as shown in Figure 5.5a and Figure 5.5b respectively. There are a few observations that can be made from Figure 5.5. First of all, the shear and compressive strength in Figure 5.5a and Figure 5.5b respectively have similar strength against freezer time curves. The only main difference between the two plots is the strength values themselves, which are higher for the compressive strength. As has been explained in Section 5.1, the compressive strength should indeed follow both a similar trend as the shear strength as well as be higher than the shear strength. One more difference between the two plots is the before last point, which has a larger spread for the shear strength than for the compressive strength. All other data points have a comparable spread between the two plots. This difference likely comes from the fact that the shear strength considers both the angular displacement and vertical penetration of the ice grains, whereas the compressive strength is based mostly on the vertical penetration only. This is likely the difference in spread size between the shear and compressive strength for the before last data point.

Second, it can be seen that some data points have a larger spread than others. Each data point in the plots in Figure 5.5 represents all strength measurements taken on one ice analogue sample during one test, as described in Section 5.1. Figure 5.3 shows the strength against freezer time as in Figure 5.5 but including all individual measurements. Figure 5.5 shows an accurate representation of the data at lower freezer times. It can be seen, however, that the data points at longer freezer times, such as t_f = 144 hours, have a larger spread. A hypothesis explaining this is that the measurements of this data point can actually be divided into two sections; one at the higher end of the spread and one at the lower end. This is because a difference in measurement results could be seen between the measurements taken in the outer edge of the container versus the measurements taken in the inner edge of the container, as is shown in Figure 5.1a. This strength difference is less noticeable, although still present, for the data points with a shorter freezer time, but becomes larger for the data points with a longer freezer time. A longer freezer time thus also has an impact on both the shear and compressive strength of the sample relative to where it was tested.

The third observation that can be made from Figure 5.5 is the upward trend for both the shear and compressive strength. This indicates that the strength of the ice analogues increases the longer they spend in the freezer before testing. In Figure 5.5a, it seems that the strength curve is starting to reach a plateau near the end. However, in order to know if that is actually the case more tests have to be done with a longer t_f. Especially since the strength curve in Figure 5.5b shows that the last data point is actually increasing significantly again. To explain why the shear and compressive strength of the ice analogue increases with an increasing freezer time, the sintering of the ice grains is studied.

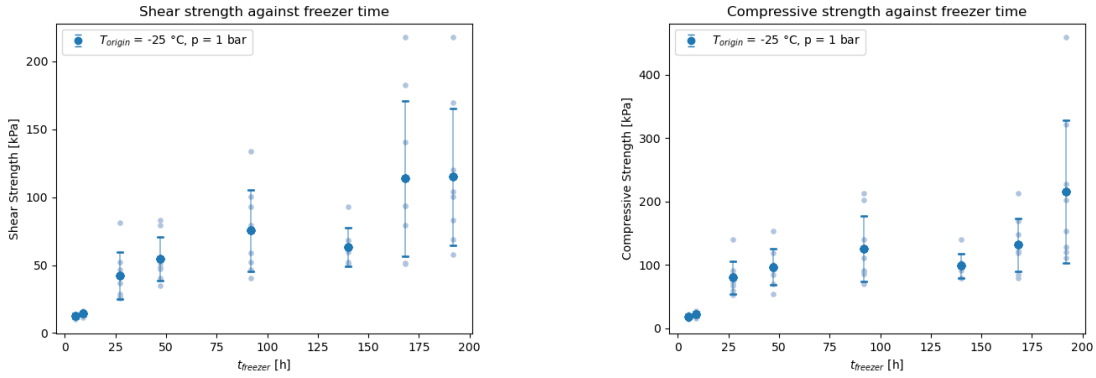

(a) Shear strength

(b) Compressive strength

Figure 5.6: Shear (a) and compressive (b) strength of the -25 °C ice analogues against freezer time in atmospheric pressure including each measurement point as well as the mean with the spread.

5.2.1. Interpretation of Freezer Time Results

There are two aspects of the freezer time effect results that need to be discussed: the effect on the homogeneity of the ice analogues and why the freezer time increases the shear and compressive strength of the samples. To start with the homogeneity of the ice analogues, it was observed that the freezer time has an effect on the homogeneous freezing of the ice analogue sample. The longer the sample has been in the freezer, the larger the difference in homogeneous freezing of the sample. To consider the measurement indications in Figure 5.1a, the blue measurements in the inner part of the ice analogues have a lower strength compared to the black measurements towards the edge of the ice analogues. Since there is a layer of solid ice around the container with the ice analogue, this is likely the reason behind the non-homogeneous freezing of the ice analogues after a certain freezing time. The wall between the ice analogue and the solid ice layer constrains deformation, reducing strain and pore expansion of the ice analogue near the wall. The centre of the ice analogue is less confined, and those grains can thus deform more freely under stress, which would appear as a lower strength. This means that the lower end of the data points should be considered for comparisons between the mechanical strength results and Enceladus' surface for the purpose of future lander missions.

Sintering

The second result of the effect of freezer time is the strength increase with a longer freezer time in atmospheric pressure. This can be explained by the sintering of the ice grains, where the sample grows stronger the longer time it has had to sinter in the freezer. Within a freezing timescale of maximum 200 hours, which is the range in which the ice analogues were tested, stage 1, and possibly stage 2, sintering could be occurring depending on the freezer temperature. During stage 1 sintering neck growth occurs mostly, whereas in the second stage it is densification that is dominant. This is explained in more detail in Section 2.3. Whether or not sintering occurs is dependent mostly on the grain size and temperature of the sample. Molaro et al. (2019) for example show that in an experimental setting with 50µm grains stage 2 sintering with full neck growth is reached in two weeks at -20°C. This example gives a feeling for the timescale in which sintering could occur. However, the grains in the tested ice analogues are double in size and frozen at colder temperatures, so it will take longer before stage 1 or 2 sintering is fulfilled. In ice, the first sintering stage is dominated by surface and vapour diffusion mechanisms out of which vapour diffusion is the most dominant factor. This means that neck growth would occur faster than the densification of the ice analogues (Molaro et al., 2019). For stage 1 sintering calculations, the vapour diffusion mechanism is thus used. More details regarding sintering mechanisms can be found in Section 2.3.

Using Equation 2.4 and Equation 2.2, described in Section 2.3, the sintering timescale for stage 1 sintering can be estimated for the ice analogues. The calculated sintering timescale depends on the estimated neck-growth that occurs during the sintering. These rates can be experimentally determined as well. However, visualising the neck formation is not possible with the available tools, thus an

[1] https://www.engineeringtoolbox.com/air-diffusion-coefficient-gas-mixture-temperature-d_2010.html

Symbol	Unit	Parameter	Value for T=-25 °C	Value for T=-80 °C	Source
T	[K]	Temperature	248.15	193.15	-
p_{sat}	[Pa]	Vapour pressure over ice	63	0.05525	Wexler (1977)
c_∞	$[mol \cdot m^{-3}]$	Vapour concentration	$3.05 \cdot 10^{-2}$	$3.46 \cdot 10^{-5}$	Calculated
γ	$[Jm^{-2}]$	Surface energy	0.077	0.009	Boinovich and Emelyanenko (2014) & Fig.9 in Jabaud et al. (2024)
V_m	$[m^3mol^{-1}]$	Molar volume of ice	$1.96 \cdot 10^{-5}$	$1.96 \cdot 10^{-5}$	-
D_v	$[m^2s^{-1}]$	Diffusivity of water vapour in air	$1.9 \cdot 10^{-5}$	$1.27 \cdot 10^{-5}$	Extrapolation of diffusion table [1]
R	[m]	Particle radius	$5.0 \cdot 10^{-5}$	$5.0 \cdot 10^{-5}$	-
a_0	[m]	Inital neck radius	$1.0 \cdot 10^{-6}$	$1.0 \cdot 10^{-6}$	Assumption

Table 5.1: Parameters required for sintering calculations of ice analogues at -25 °C and -80 °C.

estimation is used instead. A standard assumption for stage 1 neck-growth is 5% of the grain radius for a small neck (a/R = 0.05) and 10% for a larger early neck (a/R = 0.10) (Thomsen et al., 2018). Using these two neck-growth estimations, the parameters given in Table 5.1, and Equation 2.4, the stage 1 sintering timescales can be calculated for both ice analogues. This section focuses just on the -25 °C analogue results, the -80 °C analogue results can be found in Section 5.3 but the data required for its calculations are also included in Table 5.1.

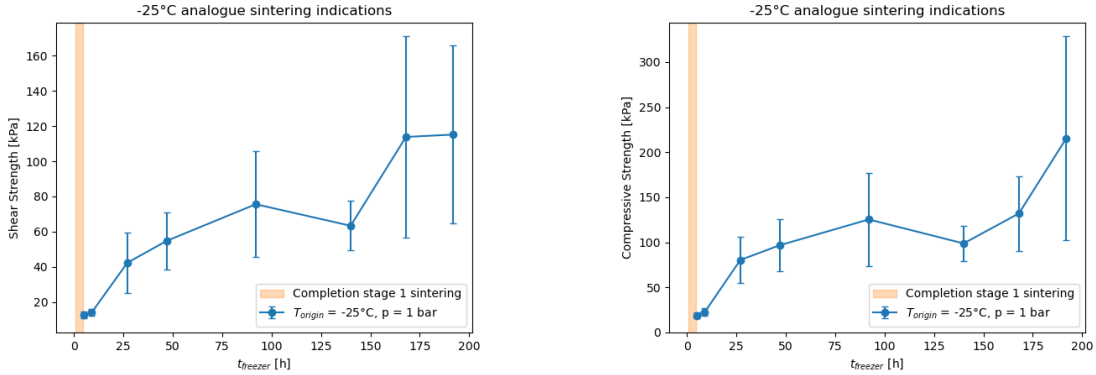

(a) Shear strength against freezer time of -25 °C analogue.

(b) Shear strength against freezer time of -80 °C analogue.

Figure 5.7: The increasing shear (a) and compressive (b) strength of the -25 °C analogue including sintering indications.

For the -25 °C ice analogues, the sintering timescale ranges between 0.55 and 4.66 hours for the two neck-growth ratios respectively using Equation 2.4 and the parameters given in Table 5.1. With the relation by Molaro et al. (2019), a sintering timescale of 0.91 hours is estimated. This indicates that stage 1 sintering for the -25 °C ice analogue is completed after maximum 4.5 hours of freezing already. Such early completion of stage 1 sintering is likely the reason why the shear and compressive strength of the -25 °C ice analogue do only increase as freezer time increases. Comparing this sintering stage evolution with the sintering timescale graph by Kang (2004) in Figure 2.22, the -25 °C ice analogues are well in the second sintering stage, most likely undergoing densification of the samples near the end of the freezer time range. Unfortunately, no weight measurements were taken so this statement cannot be verified with experimental data. Nevertheless, the derived sintering timescale shown with the strength curve of the -25 °C ice analogues in Figure 5.7, does suggest it is well in the second sintering stage as the completion of the first stage has long been passed at the end of the freezer time range in the graph. In Figure 5.7, the orange phase indicates the completion of stage 1 sintering according to the calculations. The data points to the right of the line are thus in stage 2 sintering. Stage 3 sintering is not yet occurring as there is no clear plateau indication as is expected from the sintering timescale graph by Kang (2004) in Figure 2.22. The freezer time of the samples thus increases the shear and compressive strength of the ice analogues in atmospheric pressure due to sintering.

To conclude the results on the effect of freezer time on the shear and compressive strength of the -25 °C ice analogues in atmospheric pressure, both the freezer time and the freezing homogeneity of the sample impact the strength of the analogue. The freezer time increases both the shear and compressive strength in atmospheric pressure due to the sintering of the ice grains. The freezer time also has an

effect on the homogeneous freezing of the ice analogue samples as well leading to two different strength indications in the ice analogues. The solid water-ice layer around the sample is likely a reason for this occurrence due to the wall constraints on the ice grain structure. This gives a larger spread for the data points in the shear and compressive strength plots in Figure 5.5 for a longer freezer time. The lower end of the spread in the plots are thus more indicative of the ice analogue strength.

Effect of Freezer Time Results

- The shear and compressive strength of the -25 °C ice analogues increases with an increasing freezer time.
- The -25 °C analogue reaches the completion of stage 1 sintering within only maximum 4.5 hours. The freezer time of the samples increases the shear and compressive strength of the ice analogues in atmospheric pressure due to sintering.
- The weaker inner circle of the samples gives a more accurate strength indication of the sample as the grains are unconfined as is the case on Enceladus. The lower end of the spread in the plots is thus more indicative for the ice analogue strength.

5.3. Effect of Origin Temperature on Ice Analogue Strength

This section describes the effect of the origin temperature of the ice analogue samples, thus in which freezer they were placed, on the strength of the ice analogues. The difference in shear and compressive strength results between the -25 °C and -80 °C ice analogues in atmospheric pressure is thus given in this section. Before diving into the effect of origin temperature on the ice analogue strength, the ice analogues themselves will be addressed. Figure 5.8 shows three versions of the ice analogue samples: a) a freshly prepared ice analogue sample before it has been put into a freezer, b) an ice analogue left in the -25 °C freezer for 190 hours, and c) an ice analogue left in the -80 °C freezer for 190 hours. Although a close look of the images is necessary, there are clear differences that can be seen between these three ice analogue versions, especially when handling the samples in the lab. The ice analogue in Figure 5.8a has a powder-like consistency as the grains have just been produced. In this version of the ice analogue the cone would simply sink into the sample with barely any resistance from the ice grains. Figure 5.8b shows an ice analogue that has just been taken out of the -25 °C freezer after 190 hours. This analogue has a consistency closer to a solid frozen surface, although it can be seen that the sample origin is made of ice grains. The ice analogue presented in Figure 5.8c has just been taken out of the -80 °C freezer after 190 hours as well. Its consistency is less like a solid frozen surface and it is easier to still see the individual ice grains compared to the -25 °C analogue. Out of the three images in Figure 5.8, the difference between Figure 5.8b and Figure 5.8c can be seen especially. The ice grains of the -80 °C analogue still seem as individual grains, whereas the -25 °C analogue ice grains have already started to grow together, which can already visually be determined from Figure 5.8.

(a) Freshly prepared ice analogue before it is placed into freezer.

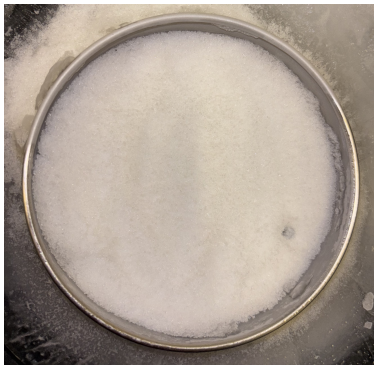

(b) Ice analogue that has spent 190h in -25 °C freezer.

(c) Ice analogue that has spent 190h in -80 °C freezer.

Figure 5.8: Differences in ice analogue surface after a) being freshly prepared, b) left in the -25 °C freezer for 190 hours, and c) left in the -80 °C freezer for 190 hours.

Now that the visual effect of the origin temperature on the ice analogues has been illustrated, its

effect on the actual shear and compressive strength of the analogues is presented. To show this effect, the strength against freezer time plots in Figure 5.5 is now extended to show also the results for the -80 °C analogue in atmospheric pressure. This is given in Figure 5.9, where Figure 5.9a and Figure 5.9b give the shear and compressive strength against freezer time respectively. Both the shear and compressive strength graphs in Figure 5.9 indicate a strength difference between the origin temperature of the ice analogues for the atmospheric pressure. In both plots, the -25 °C ice analogues are between a few and 25 kPa stronger than the -80 °C ice analogues, except for one outlier at $t_f = 144$ hours. The reasoning behind the larger spread has already been given, but for this data point especially the difference is quite large. The more accurate part of this data point is the lower end of the spread, as explained. Considering this lower end instead of the middle or top is in line with the other data points. Going back to the effect of origin temperature, in atmospheric pressure, a warmer origin temperature of the analogues thus results in an increased shear and compressive strength for an equal freezer time. Another apparent outlier is the data point for the -80 °C analogue at $t_f = 160$ hours. The shear strength is less spread out for this sample, although this is expected for longer freezer times. In this case, the sample was particularly weak and only four measurements could be taken. These were all taken somewhat in the middle of the sample, resulting in only weak measurements from the inner part of the sample and no measurements at the edge of the sample. Additionally, it can be seen that the -80 °C analogue curve does not regularly increase over the entire t_f range. The shear and compressive strength curve of the -80 °C ice analogue is thus not yet constant within the tested timescale.

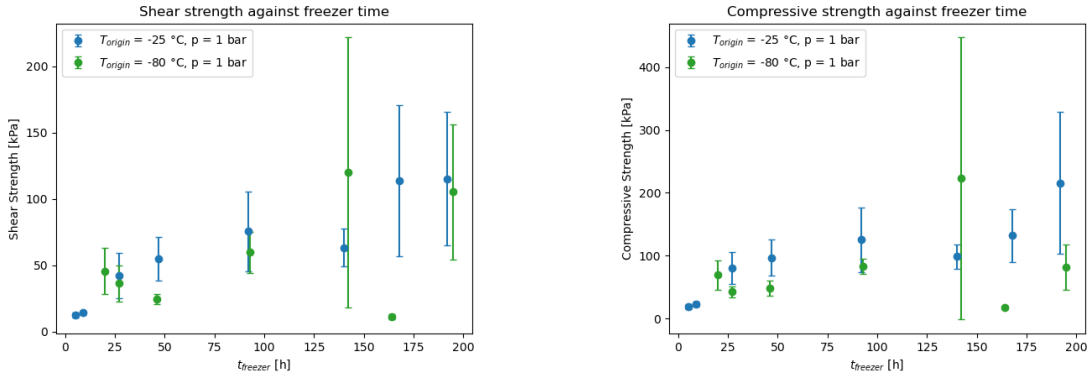

(a) Shear strength

(b) Compressive strength

Figure 5.9: Shear (a) and compressive (b) strength of both ice analogues against freezer time in atmospheric pressure.

To discuss why a warmer origin temperature results in an increased analogue strength, the sintering of the ice grains can be considered once again. First, the sintering timescale of the -80 °C analogue needs to be calculated. For this ice analogue, the sintering timescale range is calculated to be between 202 and 1716 days for the two neck-growth ratios respectively using Equation 2.4 and Table 5.1. With the relation given by Molaro et al. (2019), the estimated sintering timescale is 757 days which is almost evenly in the middle between obtained the timescale range using Equation 2.4. This timescale is a lot longer than what has been tested for the ice analogues. Since the -80 °C ice analogues are thus undergoing no or very early stage 1 sintering, this can explain why there is an irregular increasing trend for the -80 °C ice analogues for an increasing freezer time. The ice grains are not yet regularly growing necks, which results in a more scattered strength versus freezer time plot for the -80 °C analogue. Comparing this with the visual inspection of the samples, where the -80 °C analogues remained relatively loose, it can be concluded that the -80 °C ice analogues are still in the neck formation stage with a slow increase in strength.

As was shown in Section 5.2, the -25 °C analogue reaches completion of stage 1 sintering quite quickly while the -80 °C analogue is not even close to reaching it in the timescale done during these strength tests. Combined with the fact that the -25 °C analogues visually appear stronger than the -80 °C analogues, it is most likely sintering that causes the strength difference between the two analogues. This is also in line with previous literature done on the effects of sintering on the strength of ice samples (Choukroun et al., 2020, Gundlach et al., 2018, Molaro et al., 2019). To conclude the effect of origin temperature on the ice analogue strength, a warmer origin temperature thus has an increased strength

compared to an analogue with a colder origin temperature. This is due to the faster sintering that occurs for the warmer ice analogue samples. The irregular increase in strength for the -80 °C analogues within this t_f range is caused by the lack of sintering that has occurred this far for such a cold sample. The sintering of the samples is thus the real determining factor behind the effect of the origin temperature on the ice analogue strength.

Effect of Origin Temperature Results

- The -80 °C ice analogues are undergoing no or early sintering in the tested freezer time timescale. This results in irregular and weaker shear and compressive strength compared to the -25 °C ice analogues.
- A warmer origin temperature results in an increased shear and compressive strength of the ice analogues. This is due to the faster sintering that occurs for warmer ice analogue samples.
- The difference between the two ice analogues can be inspected visually as well, as the -80 °C analogue still appears as relatively loose grains after spending time in the freezer, whereas the -25 °C analogue presents as a more uniform surface after an equal freezer time.

5.4. Effect of Pressure on Ice Analogue Strength

This section considers the effect of varying pressures on the strength of the ice analogues. The pressures at which the tests were performed are at atmospheric pressure (1bar) and vacuum pressure (0.1mbar). Considering once more the strength against freezer time plots in Figure 5.5, but now adding the vacuum pressure results, the plots in Figure 5.10 are obtained for both the shear and compressive strength in Figure 5.10a and Figure 5.10b. Here, as was stated earlier, it can be seen that for atmospheric pressure both the shear and compressive strength increase with an increasing freezer time. In vacuum pressure however, both the shear and compressive strength show a seemingly constant value against an increasing freezer time. The strength of the ice analogues themselves is also significantly lower for the tests performed under vacuum.

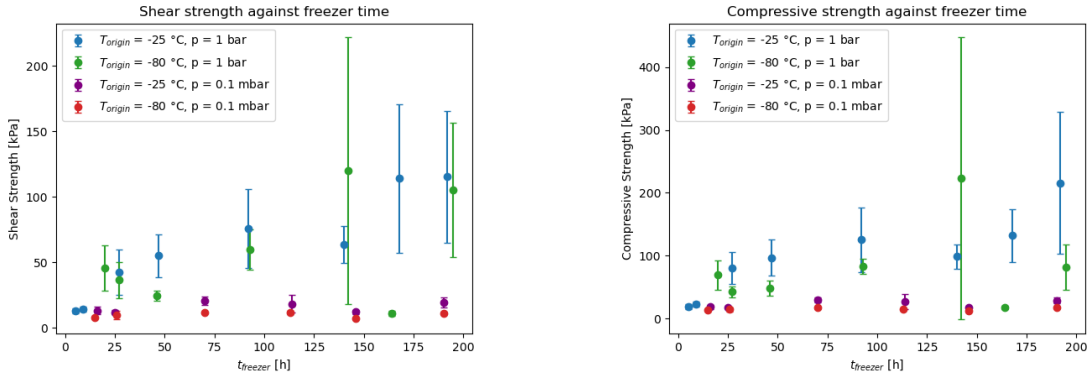

(a) Shear strength

(b) Compressive strength

Figure 5.10: Shear (a) and compressive (b) strength of the ice analogues against freezer time for atmospheric and vacuum pressure with T_{origin} = -25 °C and -80 °C.

5.4.1. Effect of Vacuum Pressure on Ice Analogue Temperature

Looking at Figure 5.10, the vacuum pressure thus seems to have a constant and important effect on the strength of the ice analogues. To understand what could be the reason behind this behaviour, first the effect of the vacuum pressure on the ice analogues is shown in Figure 5.11. The graphs in Figure 5.11 are the result from putting both a -25 °C and -80 °C ice analogue into the vacuum chamber with a thermocouple placed into each sample. A third thermocouple is placed on a tripod to measure the temperature of the environment inside the vacuum chamber. The top graph indicates these three temperatures over time in the vacuum chamber while the bottom graph indicates the absolute pressure

of the vacuum chamber at the same time. In the bottom graph p_1, p_2, and p_3 each measure the same absolute pressure. Lowering the pressure of the vacuum chamber further requires putting LN_2 into the cold finger. The moment at which this is done is indicated in Figure 5.11 through the red dotted line. At around 1800 seconds the vacuum chamber is vented, at which point both the pressure and temperature of the vacuum chamber and the temperature of the ice analogues increases again.

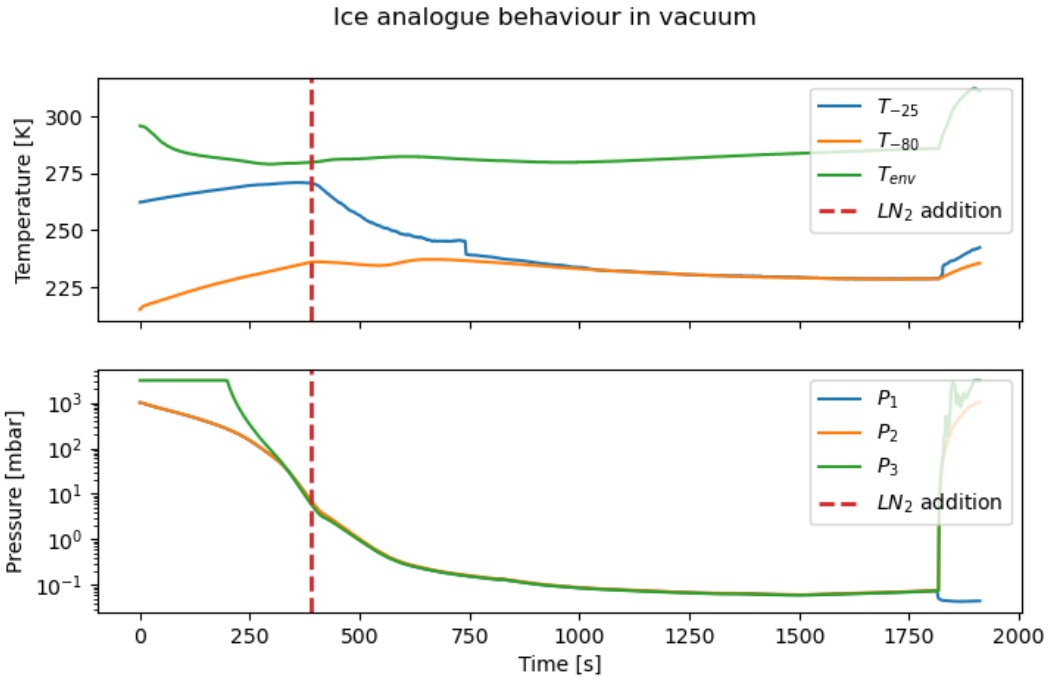

Figure 5.11: The evolution of the temperature of the ice analogues (T_{-25}, T_{-80}) and vacuum chamber environment (T_{env}) from pumping the vacuum chamber to venting it after 30 minutes. The red dotted line indicates when LN_2 was added into the cold finger.

In the top graph of Figure 5.11, it can be seen that the environmental temperature remains about the same throughout the entire vacuum chamber test. The temperature of the two ice analogues does change throughout however. Before the LN_2 is poured into the cold finger, the temperature of both ice analogues is increasing, even while the vacuum chamber is already pumping down. Once the LN_2 has been poured into the cold finger, the temperature of both analogues starts to behave differently from before the LN_2 entered the system. The temperature of the -25 °C (248 K) analogue starts to decrease significantly until it reaches around 228K after 1100 seconds, after which it remains at this temperature. The temperature of the -80 °C (193 K) analogue decreases and increases a bit after the LN_2 was added, but goes towards 228K after around 1100 seconds as well and remains at this temperature too. At a pressure of 0.1mbar the temperature of both the -25 °C and -80 °C ice analogues thus goes to ∼228K and remains at that temperature.

The reason why the temperature of both ice analogues go to 228K after reaching 0.1mbar in the vacuum chamber can be explained by thermodynamics. Considering the water phase diagram in Figure 5.12, it can be seen that the 228K temperature of water ice in 0.1mbar, or 10Pa, corresponds with the equilibrium line of water. As indicated in Figure 5.12, the temperature of the analogues moves towards that equilibrium line as the pressure in the vacuum chamber decreases. The temperature of the ice analogues inside the vacuum chamber can thus not be controlled separately from the pressure. Instead, it is the pressure of the vacuum chamber that determines the temperature of the analogues.

5.4.2. Effect of Vacuum Pressure on Failure Mode

Considering again Figure 5.10, the origin temperature does not have a big impact on the strength of the ice analogues in vacuum pressure at equal freezer times in both the shear and compressive strength plots, in Figure 5.10a and Figure 5.10b respectively. While a small difference in strength can be observed for

[2]https://www.originlab.com/www/products/GraphGallery.aspx?GID=621

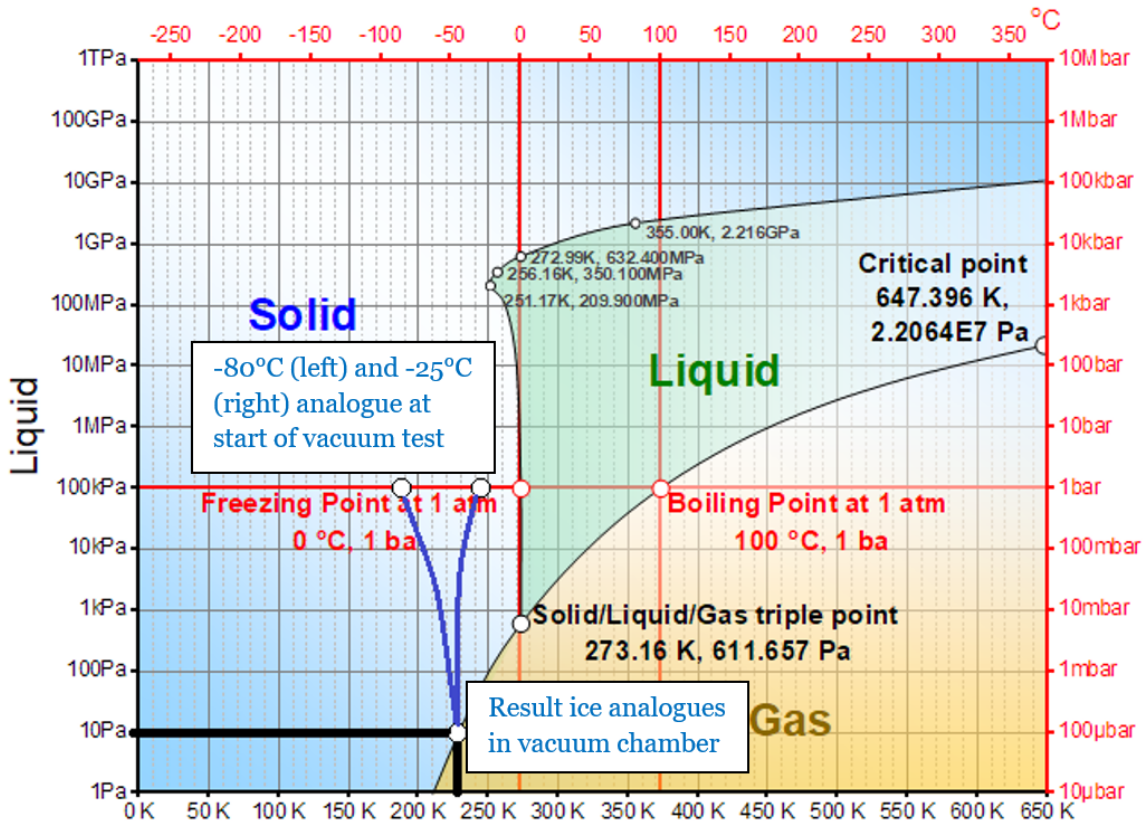

Figure 5.12: The evolution of the temperature of the ice analogues (T_{-25}, T_{-80}) and vacuum chamber environment (T_{env}) from pumping the vacuum chamber to venting it after 30 minutes. The red dotted line indicates when LN_2 was added into the cold finger. Edits are made on top of phase diagram image by OriginLab [2].

all but one of the -25 °C and -80 °C analogues at the same freezer time, this is a difference of just a few kPa. There is one outlier for the -25 °C analogue measurement at $t_f \approx 112$hours, but all other data points indicate the same trend of just a small strength difference between the two analogues with different origin temperatures. Although the effect of the origin temperature on the strength itself of the ice analogues under vacuum pressure is low, the failure mode of the two ice analogues does differ after a certain freezer time. For the last two data points in Figure 5.5, at $t_f = 146$ and 190 hours, a visual difference in failure mode between the -25 °C and -80 °C analogues can be observed, which is shown in Figure 5.13. The -25 °C analogue failed in a brittle manner, which is indicated by the cracks in the surface in Figure 5.13a. The -80 °C analogue, in Figure 5.13b, shows no evidence of cracking or plastic deformation apart from the cone indentation. While there is no other research on the strength testing failure modes of fine ice grains at these temperatures under vacuum, a logical explanation could come from the sintering of the analogues in the freezer before testing. At -25 °C, stage 1 sintering occurs producing larger necks that can make the surface more brittle as it starts to behave more like one uniform surface. At -80 °C, the sintering is extremely slow. This leaves smaller, less rigid contacts which result in a more deformable surface. The effect of the origin temperature in vacuum pressure on the shear and compressive strength is thus low in strength value, but does result in different failure modes between the -25 °C and -80 °C analogues after a freezer time of at least 146 hours.

As was indicated in the strength against freezer time plots in Figure 5.10, the origin temperature has less of an effect on the shear and compressive strength of the analogues in vacuum pressure compared to atmospheric pressure. This effect of the analogue temperature moving towards the equilibrium line due to pressure could explain why this strength difference becomes smaller. There is still a small strength difference, which makes sense since the analogues have spent hours in the freezer sintering beforehand which occurs a lot faster for the -25 °C ice analogues compared to the -80 °C analogues. A clearer effect of the origin temperature on the analogue strength is its failure mode, as was seen in Figure 5.13, where the origin temperature of -25 °C results in brittle failure whereas no plastic deformation is visible for

(a) The -25 °C analogue after strength testing with $t_f = 190$ hours.

(b) The -80°C analogue after strength testing with $t_f = 190$ hours.

Figure 5.13: The a) -25 °C and b) -80 °C ice analogues after strength testing under vacuum pressure with a longer freezer time.

the -80 °C analogue. Thus, even if the origin temperature of the analogues does not have a big effect on the shear and compressive strength itself, it does have an important effect on the failure mode. The implications this has for the surface of Enceladus and potential lander missions is discussed further in Chapter 6 *Lander Missions to Enceladus*.

5.4.3. Sublimation of the Ice Analogues

Now it has been determined that the origin temperature of the ice analogues only seems to have a big effect in failure mode under vacuum pressure and not on the strength itself as the vacuum pressure changes the analogue conditions. As is indicated in Figure 5.10, the strength of both ice analogues in vacuum pressure is more or less constant at a low shear and compressive strength. To understand what could be the reason behind this low and somewhat constant strength, the sublimation of the ice analogues during vacuum testing is considered. Sublimation is the direct phase transition from solid to gas without passing through the liquid state. This occurs in a vacuum because the surrounding pressure is so low that the substance's vapour pressure at a given temperature exceeds the external pressure, allowing the molecules to escape directly from the solid phase into the gas phase (Kossacki et al., 1999). There are two ways to determine whether sublimation is occurring: measuring the weight difference (Δm) of the analogues and analysing the temperature and pressure of the tests using the Clausius-Clapeyron relation. Starting with the weight measurements, a difference of 36g and 10g was measured for the -25 °C and -80 °C respectively before and after the vacuum test. These values can be compared to the expected mass loss using Equation 5.1 for the sublimation rate J and Equation 5.2 for the total sublimated mass ΔM. In Equation 5.1, α is the sublimation coefficient, m the mass of a single molecule, k_b the Boltzmann constant, T the absolute temperature, and p(T) the saturated vapour pressure at temperature T. The sublimation coefficient is 0.15 and 0.98 for the -25 °C and -80 °C analogues respectively, taken from figure 3 in Kossacki et al. (1999). In Equation 5.2, A is the surface area of the analogue and t the time the analogue has spent in the vacuum chamber.

$$J = \alpha \sqrt{\frac{m}{2\pi k_b T}} p(T) \qquad [kg/m^2 s] \quad (5.1)$$

$$\Delta M = JAt \qquad [kg] \quad (5.2)$$

Using Equation 5.1 and Equation 5.2, these calculations result in an expected mass loss of 30g and 1.2g for the -25 °C and -80 °C analogues respectively. For the -25 °C analogue the experimental and calculated value are very similar, although the experimental result is higher than the calculated

result. For the -80 °C analogue, this difference in experimental and calculated results is even higher. This difference can come from the perfect-case assumptions in the calculations versus the reality from experimental testing with slight differences in for example surface area and microstructural aspects of the analogues. Pores or grain boundaries in the analogues can enhance vapour escape in the experimental setting. The -80 °C analogue also visually indicates that the grains are more loose compared to the -25 °C analogues, as visualised in Figure 5.8. These results thus do indicate that sublimation is indeed occurring during the vacuum tests, especially for the -25 °C analogue.

Another method to show that sublimation is occurring is through the Clausius-Clapeyron relation (Luna et al., 2014). This relation describes how the equilibrium pressure between two phases of a substance changes with temperature, which can be written as Equation 5.3 where L is the latent heat of the phase change and ΔV the change in specific volume.

$$\frac{dp}{dT} = \frac{L}{T\Delta V} \tag{5.3}$$

For processes like sublimation, the gas volume is much larger than the solid or liquid volume, so $\Delta V \approx V_{gas} = \frac{RT}{p}$. Substituting this simplifies Equation 5.3 to Equation 5.4.

$$\frac{d(\ln(p))}{d(1/T)} = -\frac{L}{R} \rightarrow \ln(p) = -\frac{L}{R}\frac{1}{T} + C \tag{5.4}$$

Thus, to visualise sublimation using the temperature and pressure measurements from the vacuum test, Equation 5.4 can be used where a linear line should indicate sublimation occurring with a slope of -L/R. Plotting this from the T and p measurements shown in Figure 5.11, the sublimation plot in Figure 5.14 can be created. This plot includes the measurements taken during the pumping down and venting of the vacuum chamber, which is why the start and end of both curves go in any direction. More interesting are the linear lines between ln(p) = 1.5 and -2.5, or between p = 4.482 and 0.082 mbar, for both ice analogues, where the steepness of the lines changes for the -80 °C analogue.

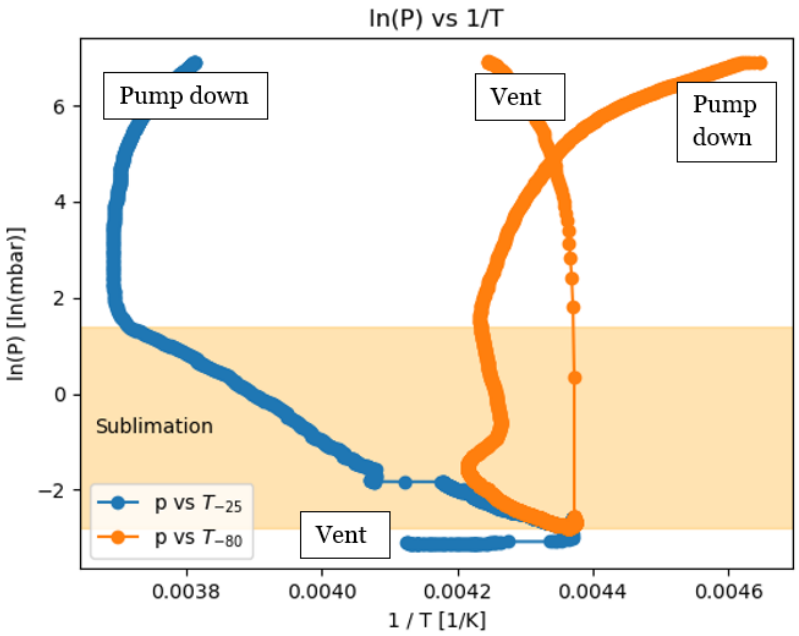

Figure 5.14: Sublimation indications for the -25 °C (blue) and -80 °C (orange) analogues under vacuum testing using the Clausius-Clapeyron relation.

Taking the temperature and pressure plots of the vacuum test in Figure 5.11, the duration of sublimation during the test, obtained from Figure 5.14, can be plotted onto Figure 5.11. This results in the graph shown in Figure 5.15 which shows exactly when sublimation is occurring for both the -25 °C and -80 °C analogues. Figure 5.15 indicates that sublimation begins just after the liquid nitrogen has been poured into the cold finger and lasts for 645 seconds until the analogues have reached a

temperature of 228K. The -25 °C analogue decreases a lot more in temperature compared to the -80 °C. This correlates with the sublimation rate that is visualised in Figure 5.14 where a less steep curve indicates a higher sublimation rate, which is the case for the -25 °C analogue. There is thus sublimation occurring during the vacuum tests, changing the ice analogue conditions, and with that also its shear and compressive strength.

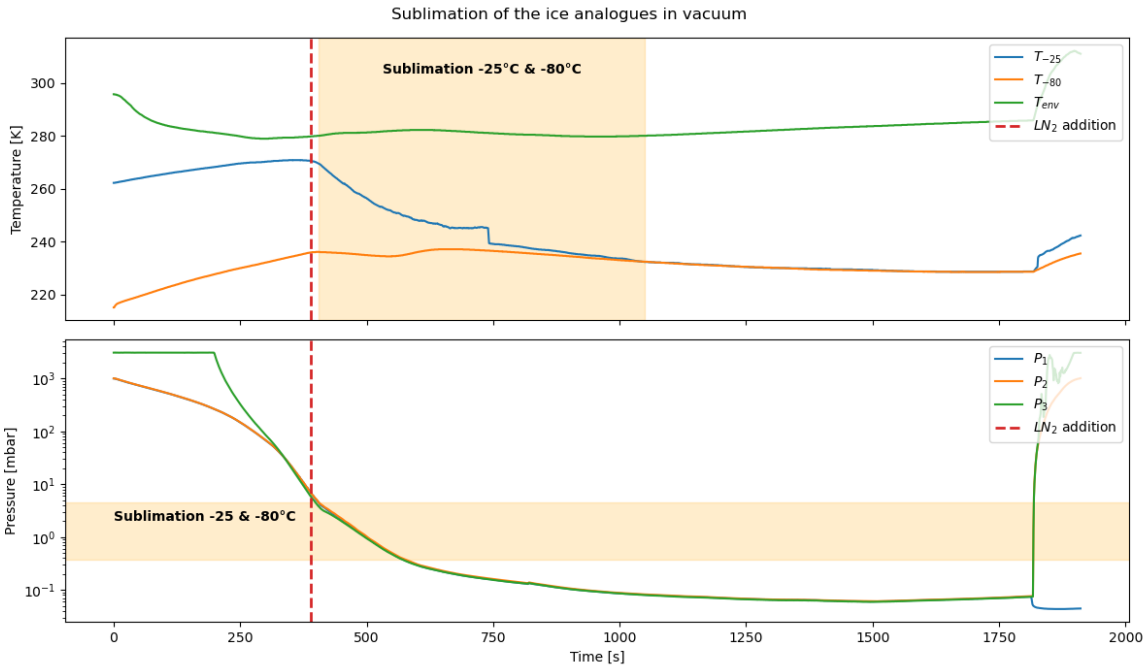

Figure 5.15: Instances when sublimation occurs for the -25 °C (blue) and -80 °C (orange) analogues under vacuum testing.

5.4.4. Interpretation of Vacuum Pressure Results

Now that it is clear that sublimation is occuring, and at the exact moments when, its effect on the strength of the ice analogues can be discussed. Although the analogues were sintered in the freezer before testing, and have therefore already started neck formation, and even densification for the -25 °C analogue, exposing the analogues to vacuum during testing does have an impact on the samples themselves. A hypothesis on why this occurs is that the vacuum environment, through e.g. sublimation, can rapidly change the microstructure of the analogues. Sublimation in vacuum removes material, shrinking or reshaping necks until different samples converge to a similar contact geometry (Morin et al., 2021), leading to a near identical strength for the different analogue tests. If the vacuum condition thus alters the microstructure of the analogues, then all samples will show similar strength despite having different sintering histories. This is valid at least for the sintering stages encountered in this research, which is both stage 1 and stage 2 sintering depending on the analogue.

Even though the strength is similar for all analogues tested under vacuum, the failure modes between the -25 °C and -80 °C analogues are different in vacuum testing, as shown in Figure 5.13. The difference can be hypothesised through sublimation and the effect of vacuum on the microstructure of the ice analogues. At -25 °C, the analogue is near the ice brittle-ductile transition, which means that the analogue would show plasticity under atmospheric analogues, as it does in the atmospheric pressure tests (Schulson, 1979). In vacuum however, with sublimation occurring, the necks between the grains can erode and micro-cracking can occur. This effect would cause a sudden brittle failure once loaded. At -80 °C, a lot less sublimation is occurring, so these vacuum-induced effects are lower. This small difference between the two analogues does seem to have an effect on the failure mode, but not the actual strength of the analogues.

To conclude, the effect of pressure on the ice analogue strength is that the ice analogues themselves undergo different processes under different pressures which has an impact on the strength of the ana-

logues. In atmospheric pressure, the shear and compressive strength increase with an increasing freezer time. In vacuum pressure, the ice analogues undergo sublimation which changes the micro-structural composition of the analogues resulting in a more or less constant lower shear and compressive strength compared to the atmospheric pressure test results. This change in micro-structural composition of the ice analogues under vacuum seems to be equal for the strength indications, but different for the failure modes, which means that the two ice analogues do undergo different micro-structural changes. Nevertheless, the implications of both the strength and failure mode results of the ice analogues in vacuum on Enceladus' surface and future lander missions are discussed in the next chapter.

Effect of Pressure Results

- In atmospheric pressure, both the shear and compressive strength increase with an increasing freezer time.
- The shear and compressive strength of both ice analogues is very low at ∼5 to 30 kPa under vacuum pressure.
- Under vacuum, the temperature of both ice analogues goes towards the same equilibrium temperature of 228 K at 0.1 mbar. During that process sublimation occurs for both ice analogues reducing its strength.
- The freezer time has little effect on the shear and compressive strength of the ice analogues under vacuum as the strength results are nearly constant.
- The sintering of the ice analogues, due to the freezer time, does have an effect on its failure mode. Once the ice analogue is at least well in the second sintering stage, the sample fails in a brittle manner.

5.5. Mechanical Properties of the Ice Analogues

The effect of freezer time, origin temperature, and pressure on the shear and compressive strength of the ice analogues have now been described in detail, but separately. The purpose of this section is to bring all these results together and give a better overview of its findings. This is done by combining the sintering results, in the sense of how much the ice grains have transformed together, with the results of the three effects on the ice analogue strength. To do this, Figure 5.16 shows the transformation the ice grains go through as they pass each sintering stage. From loose grains in stage 0 to neck formation, grain growth, pore coalescene, and its theoretical final stage. Although the ice grains in this work only experience up to the second stage, the other stages are included for completion. The ice grain stages shown here in Figure 5.16 are then used to indicate for each effect what the stage of the ice grains is and how it effects the strength of the analogues.

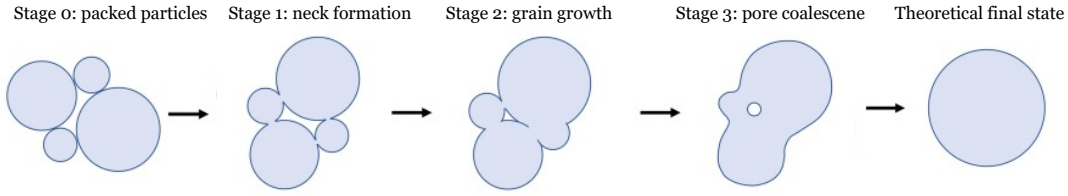

Figure 5.16: A schematic indicating the transformation of the ice grains during the different sintering stages. This image is adapted from Figure 10.4 by Sola and Trinchi (2023).

Starting with the effect of freezer time, depicted in Figure 5.17a, it can be seen that in atmospheric pressure an increasing freezer time results in an increased shear and compressive strength. As the freezer time increases, the ice grains go through each sintering stage until reaching the theoretical final stage at the upper right corner. This curve is line with the sintering stages curve by Kang (2004) given in Figure 2.22. This graph thus shows that it is the sintering together of the ice grains due to the time they spent in the freezer that increases the strength of the analogues in atmospheric pressure.

The second graph, Figure 5.17b, shows the effect of origin temperature on the shear and compressive strength in atmospheric pressure. As indicated in Figure 5.8, the ice grains of the -80 °C analogue remain loose even after 200 hours spent in the freezer. This is because it takes at least 202 days, and likely

much longer, for the ice grains to reach stage 1 sintering at a temperature of -80 °C. At -25 °C however, the ice grains reach the completion of stage 1 sintering quite early at maximum 4.5 hours, which means that after a relatively short freezer time its grains will already be well under way to the completion of stage 2 sintering. As stated before, the more the ice grains have sintered together, the stronger they become. Since the ice grains at -25 °C reach a higher sintering stage than the ice grains at -80 °C in the same time, this shows exactly why the -25 °C analogue is always stronger than the -80 °C analogue for a constant freezer time in atmospheric pressure.

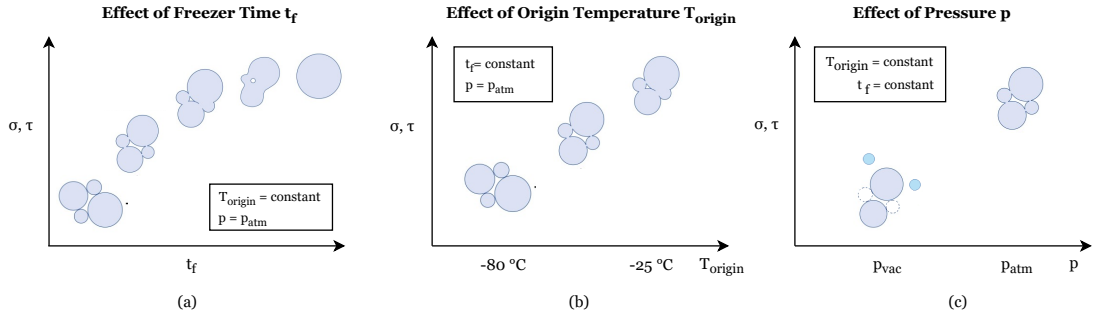

Figure 5.17: A schematic indicating the effect of freezer time (a), origin temperature (b), and pressure (c) on the ice grains themselves and the strength of its analogue. All ice grain stages are shown in Figure 5.16, except for the one in the bottom left corner of (c). Here, the blue circles indicate water vapour originating from the two dotted circles.

The final graph, Figure 5.17c, then indicates the effect of pressure on both the ice analogues and its strength. In atmospheric pressure, the ice grain stage and strength is equal to what is shown in Figure 5.17a and Figure 5.17b for a constant origin temperature and freezer time. For an equal origin temperature and freezer time, the ice grains undergo a different transformation under vacuum however, resulting in a lower strength of the analogues. This transformation is the sublimation that occurs under vacuum as the pressure makes the ice grains transform to the corresponding equilibrium temperature. This sublimation, shown in Figure 5.17c in the bottom left corner, results in some grains transforming directly from its solid state to a gaseous state (indicated as blue water vapour circles in Figure 5.17c). This leaves small gaps in the ice analogue, making the sample more porous and in return weaker. Since the used vacuum pressure is equal for each test, this same procedure happens each time resulting in the similar, weak shear and compressive strength of both ice analogues under vacuum despite having different sintering histories. The difference in failure mode under vacuum between the two analogues after a certain freezer time can be explained using these ice grain stages as well. The 25 °C analogue has ice grains that are undergoing grain growth, whereas the -80 °C analogue still has loose grains. Sticking to the grain depiction in Figure 5.16, if some grains in a stage 2 grain situation sublimate, then the other grains can still have some bonds between them. So, although the analogue becomes porous and weak, it fails in a brittle manner due to these connections. The -80 °C analogue does not fail in a brittle manner since such connections do not yet exist.

To conclude this results chapter, the freezer time, origin temperature, and pressure thus each have a significant effect on the strength of ice analogues. Especially the vacuum pressure test results show how important it is to consider these results for the study of Enceladus' surface as the findings have a significant effect on the strength of the ice analogues. Combined with the results on the effect of freezer time and origin temperature, this work presents important findings for both studying Enceladus' surface as well as future lander missions to Enceladus and other icy moons.

6

Lander Missions to Enceladus

This chapter discusses the results obtained in Chapter 5. First, the ice analogue properties are translated to Enceladus' surface discussing the top layer of the surface, Enceladus' low pressure and gravity environment, and the surface strength indications from the ice analogue test results. This is then followed by a discussion on what these mechanical properties of Enceladus' surface imply for future lander missions.

6.1. Translating Ice Analogue Properties to Enceladus' Surface

The shear and compressive strength tests of the ice analogues were performed to see how the surfaces would respond on strength testing including the effect of sintering, vacuum, and temperature of the ice in order to learn more about what is to be expected on Enceladus. To translate the results obtained in Chapter 5 *Mechanical Properties of the Ice Analogues* to the actual surface on Enceladus, this section will discuss the shear and compressive strength, low gravity and pressure, and top layers of Enceladus surface. This is done by considering both the results in this research, as well as the research from literature.

6.1.1. Characteristics of Enceladus' Top Layer

The geysers erupting from the tiger stripes in the SPT spew large amounts of water from Enceladus' subsurface ocean into space. About ∼10 % of those particles end up in Saturn's E ring, but the rest fall back onto Enceladus' surface as frozen ice grains with a small diameter between 5 µm and 75 µm depending on its distance from the tiger stripes (Kempf et al., 2010, Scipioni et al., 2017). Larger grains, which have a lower velocity, deposit closer to the Tiger Stripes, resulting in a higher average grain size in the SPT (Southworth et al., 2019, Jaumann et al., 2008). This process of ice grains falling back onto Enceladus' surface is visualised in Figure 6.1. Figure 6.1 also indicates the terminology for the surface and icy crust of Enceladus that is used in this thesis, where the icy crust is the whole icy layer on top of the subsurface ocean and the surface is the top part of the icy crust.

These fine ice grains falling back onto Enceladus' surface, or plume deposits, are unlikely to strengthen significantly under typical surface conditions (Choukroun et al., 2020). Closer to the tiger stripes however, where higher temperatures up to 180 K can be found, Choukroun et al. (2020) state that the plume deposits could strengthen up to 10 MPa in around 15 years according to their lab experiments. However, this is the same region where most plume deposits regularly fall back onto the surface. Choukroun et al. (2020) thus also states that the strengthened ice grains would be covered by fresh plume deposits again, which actually gives uncertainty regarding the actual strength of the surface. As indicated in Chapter 5, the sintering of the ice has an important effect on the strength of the analogues. At 80 K, it would take up to 100 Myr for the ice grain surface to become consolidated (Choukroun et al., 2020). That is assuming that the surface is not altered. With constant fresh plume deposits however, the top layer of Enceladus' surface looks more snow-like rather than the ice layer below that. Martin et al. (2023) deduce that this powdery snow layer could be up to 700m thick at certain locations on Enceladus, ranging between 80 and 690m over the entire surface. The deposition of the grains from the plume could rearrange the surface composition, potentially breaking bonds between the already resting

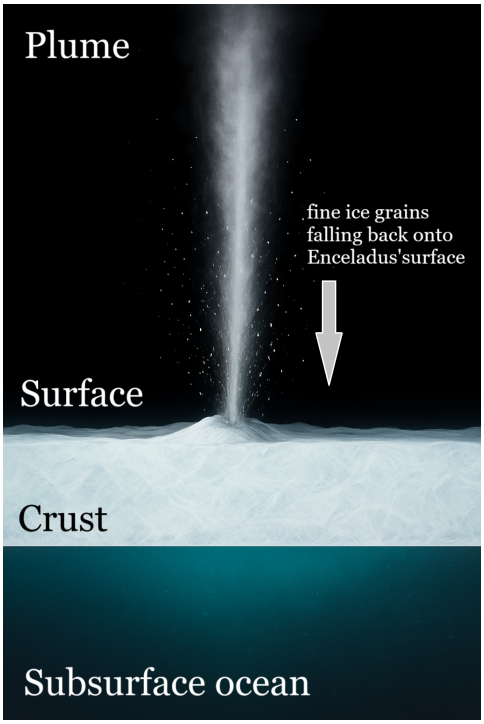

Figure 6.1: A visual representation of Enceladus' subsurface ocean and surface through which geysers spew water into the surrounding space after which frozen ice grains fall back onto the surface. This image is not to scale.

grains. This would depend on the impact velocity of these grains however and more research should be done to see whether that actually re-organises the top layer of the surface. Such re-organisation of the ice grains would reduce the amount of sintering that can occur, which indicates that the surface strength would be lower than calculated based on sintering calculations. Still, the top layer consists of unconsolidated plume deposits. It is thus expected that the top layer of Enceladus, the snowy layer, has a low shear and compressive strength, lower even than the laboratory results given in Figure 5.4 by Choukroun et al. (2020).

6.1.2. Enceladus' Low Pressure and Gravity Environment

Enceladus essentially has no atmosphere, so its surface pressure is extremely low, effectively a near-vacuum. Although this is a well-known aspect of Enceladus' environment, the combination of shear or compressive strength testing on fine ice grain analogues has previously not been performed inside a vacuum chamber. From the test results given in Section 5.4 *Effect of Pressure on the Ice Analogue Strength*, there are multiple findings that give indications that this near-vacuum pressure environment has an important impact on the strength of Enceladus' surface. At these pressures, sublimation seems to dominate over sintering of the ice analogues. This is for the relatively warm temperatures of 193 K and higher of the tested ice analogues. Sublimation of the ice analogues in vacuum in this research resulted in lower shear and compressive strength. The sublimated ice analogues represent the ice grains on Enceladus most, indicating that the surface on Enceladus is indeed quite weak; weaker than what is estimated from strength testing performed in atmospheric pressure.

The vacuum test results also indicated a brittle failure mode for the analogue that had sintered more, an effect that did not occur in atmospheric pressure. So, if enough sintering is occurring between the ice grains this would result in a brittle ice layer. Although it is hypothesised here that the top layer in the SPT is a snowy layer that has not sintered much, the layer just underneath likely has sintered a bit. Whether this amount of sintering would be enough to cause the brittle failure mode observed in the 248 K ice analogue tests is uncertain however. Although more tests should be done to state this with certainty, the 248 K analogue is in early to medium stage 2 sintering for the freezer times at which brittle failure occurs under vacuum testing. Considering temperatures between 130 K and 180 K for the SPT around the tiger stripes, it is feasible for the ice grains below the snowy layer in the SPT to

have reached this stage of sintering within ∼10 years (Gundlach et al., 2018). From the results in this thesis, the hypothesis is thus that the top layer of Enceladus' surface in the SPT closer to the tiger stripes consists of a snowy layer with little sintering occurring covering a layer where more sintering has occurred, resulting in a brittle ice layer.

One other aspect that has not been considered so far is the low gravity environment of Enceladus. The gravity on Enceladus is 0.113 m/s^2, about 1 % of the gravity on Earth. The surface porosity on Enceladus is high because of the low gravity environment. This combination can result in a very low compressive strength of the surface ice grains due to a reduced surface cohesion (Jabaud et al., 2024). This is an effect that has not been incorporated in the tests performed in this research. All analogue tests have been done under Earth gravity. The main impact that has on the results of the ice analogue tests is that the samples compact under their own weight in Earth gravity, which it would not do in Enceladus gravity. This means that the surface on Enceladus would remain porous, which results in a lower shear and compressive strength than has been measured with the ice analogues tested on Earth. This statement is in line with the results of Jabaud et al. (2024).

6.1.3. Strength of Enceladus' Surface

It has been stated already that the surface of Enceladus in the SPT will be quite weak in terms of shear and compressive strength. There is not enough knowledge, however, to use these results for the design of lander missions. To quantify the strength range of the surface, the strength results from this study will be related to Enceladus' surface. The shear and compressive strength of the ice analogues under vacuum is between 10 and 20 kPa, which is very low. Unfortunately, there are no similar tests done in vacuum by other studies, so no direct comparisons can be done to other research. The strength results of the analogues in atmospheric pressure do compare to the results found by other studies, as is described in Chapter 5. This indicates that the CONE method used is valid, and the strength results in vacuum pressure are just low. This also corresponds with the fact that a low strength is expected in vacuum pressure as is stated earlier.

Relating the 10-20 kPa strength of the ice analogues to Enceladus' surface, there are a few factors that would increase or decrease its strength that have not been done in the vacuum tests. The grain size on Enceladus' surface is smaller that that of the used ice analogues, which indicates an increased surface strength compared to the analogue tests. Comparing the analogue tests done in atmospheric pressure in this study with Choukroun et al. (2020), decreasing the grain size by a factor ∼8 results in an increased strength of a factor ∼5. Applying this relation to the vacuum strength results, this would mean that if the tests had been done with a grain size of ∼12 μm, the strength of the analogues would have been 50-100 kPa, which is still low. Additionally, the low gravity and top layer re-organisation due to plume deposits decreases the strength of the surface, as was shown in the prior two sections.

6.2. Enceladus' Surface Implications for Lander Missions

The ice analogue strength results, and their relation to Enceladus' surface, show that a low shear and compressive strength are expected, as well as a snowy top layer of the surface with potentially a brittle ice layer right underneath. These properties imply certain constraints and risks for lander missions. This includes the landing itself, but also the anchoring, mobility or sampling mechanisms of the lander. This section indicates the implication from the ice analogue results for lander missions, as well as a comparison between these experimental results and the numerical results by Harmon et al. (2023), which predict the effect of Enceladus' surface properties for lander missions using a level set discrete element method.

6.2.1. Site Selection

One aspect that all experimental studies regarding Enceladus' surface have in common is that it is difficult to determine the exact characteristics of Enceladus upper surface layers. While an idea exists, with snowy top layers and plume deposits, it is not exactly certain what to expect once a lander does go to Enceladus. It is therefore important to study the behaviour and strength of the ice grains on Enceladus' surface, but also to determine methods to adapt the future lander for the expected scenarios on the surface. Enceladus' topography, as modelled by Park et al. (2024), indicates that Enceladus' surface has a height distribution between -3.6 and 3.4 km with craters and hills. The SPT terrain is almost free of these craters, but does have hills as shown in Figure 2.2 (Spencer et al., 2009, Park et al.,

2024). Harmon et al. (2023) indicated that based on their numerical model the optimal location for landing would be a site with a 15° slope. Their reasoning for this is that the lander is then predicted to come to a rest within two footpad radii to avoid unstable slipping (Harmon et al., 2023). While no experimental research was done on a sloped ice analogue, this 15° slope will be taken as the best case scenario for now.

Harmon et al. (2023) also indicated that a site with stage 2 sintering would be optimal for landing. They state that below this sintering stage, the surface would be too weak, and after this stage it would cause bouncing of the lander. The ice analogues of this research also indicate that stage 2 sintering is preferred over stage 1 sintering. Stage 3 sintering was not incorporated in this research, but is most likely also not occuring on Enceladus, except for perhaps directly next to the vents. Considering stage 2 sintering thus indeed optimal for landing, that would mean the lander needs to land in the vicinity of the tiger stripes where the surface temperature is warm enough for stage 2 sintering to actually occur. This has to be a site with temperatures above 120 K. While temperature maps of Enceladus exist, and such site locations can thus be pre-determined, it would still be extremely useful to be able to detect the temperature of the surface from the lander just before actually landing. It is thus be useful to have some type of thermal imaging instrument on-board that can automatically determine the best local site with a warm temperature of 120K and up and 15° slope.

6.2.2. Landing on Enceladus

For the landing itself, there is one more aspect that needs to be taken account regarding the sintering of the surface. The reasoning of Harmon et al. (2023) to choose a landing site with stage 2 sintering is that the surface at stage 1 sintering is not yet strong enough and in late stage 2 or stage 3 sintering bouncing of the lander may occur. The results from this study however indicate that the top layer of Enceladus' surface may not experience this exact sintering effect. This means that the lander would have to be designed to sink through the top layer a bit before reaching a layer of the ice that has sintered enough. The site selection with stage 2 sintering thus still stands, but the lander will likely first sink through a few meters of unsintered ice grains. The lander thus needs to be designed for sinking before reaching a stable position. Additionally, the results of this thesis suggest that below that snowy top layer will be a brittle ice layer for stage 2 sintering. The lander design should thus incorporate variable penetration: the footpad must work on both the snowy top layer with risk of sinkage and possibly brittle ice. A consideration could be an outer rim that compacts snow before the main footpad takes load, so a two-stage foot. A concentrated load of the lander should be avoided as well as a potential brittle ice layer could crack or fail under such loads. Instead either larger footpads or many small footpads should be used to distribute the load. The leg interfaces should be interfaces with mechanisms like shock absorbers such that the landing impulses are absorbed rather than transmitted into the brittle surface.

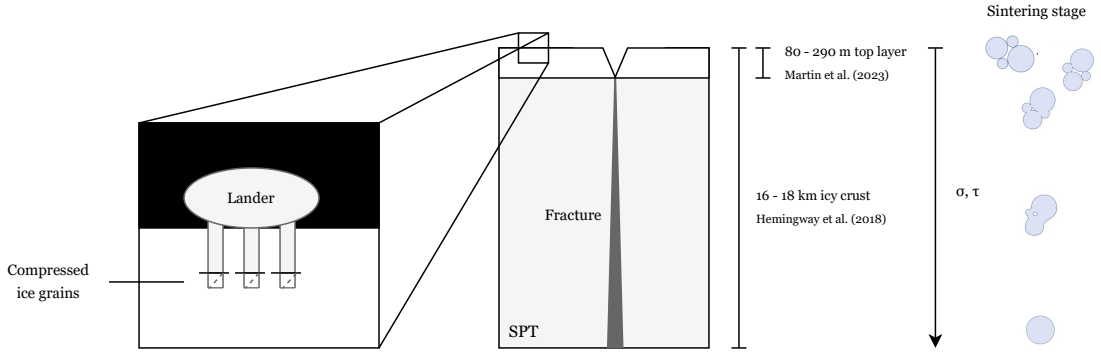

Figure 6.2: A schematic of Enceladus' icy crust and top layer including an indication of the sintering stages and strength throughout the crust. A simple indication of a lander compressing the top layer is included as well.

To provide a visual indication of the landing situation on Enceladus, Figure 6.2 gives a schematic of the height of the icy crust and top layer in the SPT including an estimation of the sintering stages that can be found throughout. Closest to the core, at the bottom of this image, the most sintered

ice grains and thus strength is expected. With the snowy top layer, the lander thus has to land in an unconsolidated ice grain surface. As mentioned before, the footpads of the lander should compress the top ice grains to reach a stronger footing. Compressed snow, or ice grains, is stronger as its compressive strength increases with an increased density (Wang et al., 2021). To give exact details regarding how much the footpads should compress Enceladus' top layer ice grains to reach a stable footing, further research should be done on testing the strength of compressed fine ice grains in cold near-vacuum environments.

Once it has landed, the lander should perform a simple in-situ strength test before continuing with more critical operations. This can be a small penetrometer or fall cone device that can penetrate from the bottom of the lander into the surface to validate the local strength. If this site is deemed too weak, the lander could then still relocate if some type of relocation mechanism is incorporated. Although the site location should be chosen at an optimal spot for strength, it could still occur that it is too weak due to the limited knowledge about Enceladus' surface. Another aspect that should be considered for the landing aspect is Enceladus' low gravity. Low gravity means that modest normal forces can already produce quite significant rebound. Such bouncing could be hazardous depending on the strength of the surface and the weight of the lander. This low gravity aspect also means that for any type of force loading, whether this is for anchoring, sampling, or mobility of the lander, the loading needs to be done in a slow and controlled manner to counteract bouncing or tipping over of the lander. Ultimately, a lander for Enceladus should be capable of touching down softly on brittle ice after penetrating or compacting a snowy top layer using the methods described in this section.

6.2.3. Sampling

The sampling of Enceladus ice requires similar thoughtfulness as for the lander itself. Whether the sampling itself is done using a small rover that can crawl into the crevasse or using a freeze-melt probe that slowly pushes through the ice by heating it, there are a few aspects that need to be taken into account. Similar for the lander itself, a low force method should be chosen to take the samples to reduce risk of ice fractures. Thermal solutions to get to a desired ice section would be preferred over using a drill or hammer for example. Another result from this thesis is the sublimation of the ice that occurs in vacuum. If ice samples are taken from below the top layer of Enceladus' surface, caution should be taken for the manner in which it is contained. An open container with fresh ice samples from below the upper layer of the surface might sublimate once it comes in contact with vacuum pressure. Although the sublimation rate is slower for colder temperatures, as was seen in the sublimation results of this work, it still occurs. A sampling container should thus be closed as soon as possible in a non-vacuum container such that the sample remains intact.

7

Conclusion

In order to give the conclusion of the work performed in this thesis, the research questions stated at the very beginning will be answered using the results and discussion in Chapter 5 *Mechanical Properties of the Ice Analogues* and Chapter 6 *Lander Missions to Enceladus*. This is done by tackling the three sub-research question that together answer the main research question of this thesis:

What are the mechanical properties of Enceladus' surface for the purpose of future landing missions studied through ice analogues?

7.1. How can Enceladus' surface be recreated in a laboratory?

This research question consists of two parts: what are the characteristics of Enceladus' environment and how can ice analogues be produced and tested to resemble that. Enceladus has a low pressure, low temperature, and low gravity environment. In the SPT, where the tiger stripes are present and future lander missions are planning to go, the ice is crystalline with temperatures between 100 and 180 K depending on the closeness to the tiger stripes, where the surface temperature of Enceladus is the warmest (Spencer et al., 2006). The plume on its surface spews water vapour into space, which freezes and partially falls back onto the surface as fine ice grains. These ice grains have an estimated size between 20 and 75 μm surrounding the tiger stripes (Scipioni et al., 2017). Two other important characteristics of Enceladus are the near-vacuum environment and its gravity of only 0.113 m/s^2.

To study the surface of Enceladus experimentally, both the surface and its environment need to be recreated. The surface was recreated by making ice analogues. These were produced by spraying water into a LN_2 dewar using a misty spraying setting. The produced ice grains were then scooped out and sieved, which resulted in fine ice grains with a size up to 250 μm. Two small containers were then filled with these ice grains and left in a -25°C and -80°C freezer. The coldest surface temperature that could thus be achieved was 193 K. In order to simulate Enceladus' low pressure, a vacuum chamber was used that could be pumped down to 0.1 mbar. The low gravity of Enceladus could unfortunately not be recreated in the laboratory, but its potential effect on the results have been discussed. Enceladus' surface has thus been experimentally reproduced using ice grains with a size up to 250 μm with temperatures of 248 K and 193 K and both atmospheric and vacuum pressures.

7.2. What are the mechanical strength properties of Enceladus' surface analogues?

To answer this research question regarding the mechanical strength properties of Enceladus' surface, the shear and compressive strength of the ice analogues are studied. Both the shear and compressive strength of the analogues was determined using the CONE method, which uses cone resistance parameters to determine the strength. In atmospheric pressure, a shear strength of 20 to 220 kPa is found depending on how the analogues had spent in the freezer. The compressive strength of the ice analogue in the same conditions is 40 to 475 kPa. These results are comparable to other experimental studies (Choukroun et al., 2020). To give more meaning to these results, the effect of freezer time, origin

temperature, and pressure on the ice analogues is studied as well.

1. **Effect of Freezer Time**
   After ice analogue production, the ice analogues were put into a freezer for a certain time, the freezer time, before tested for their strength. In atmospheric pressure, an increasing freezer time results in an increased shear and compressive strength for the ice analogues. This is due to the sintering between the ice grains that occurs while the ice analogues are in the freezer. The longer the ice analogues spend in the freezer, the more the samples can sinter together, and thus the stronger they become. The freezer time thus has an increasing effect on the shear and compressive strength of the ice analogues in atmospheric pressure due to the sintering of the ice grains.

2. **Effect of Origin Temperature**
   The ice analogues were left in a -25°C and -80°C freezer to see the effect of the origin temperature on the ice analogue strength. In atmospheric pressure, a small difference in strength can be seen between the two origin temperatures of the ice analogues. The -25°C analogues are always stronger, both in shear and compressive strength, than the -80°C analogues. This is also a result of the sintering of the analogues that occurs in the freezer. In warmer temperatures the ice analogues sinter faster, which was both visually and experimentally determined. The -25°C analogues reach stage 1 sintering after just ∼1.5 hours already, whereas it would take the -80°C analogues ∼757 days, which is a timescale outside the scope of this thesis. The warmer the origin temperature of the ice analogues, the stronger they are in terms of shear and compressive strength in atmospheric pressure due to the sintering of the ice grains.

3. **Effect of Pressure**
   The ice analogues were tested in both atmospheric and vacuum pressure with freezer times ranging up to 200 hours in a -25°C and -80°C freezer. In contrast to the atmospheric pressure results, both the freezer time and origin temperature do not have a big impact on the shear and compressive strength results of the ice analogues. Except for one outlier, all strength results are around 10 kPa regardless of their freezer time. A reason for this could be the fact that the pressure in the vacuum chamber actually determines the temperature of the ice analogues as they go towards the equilibrium temperature of ice. Before the ice analogues reach that new temperature, they sublimate which causes the analogues to become more porous. That results in a weaker shear and compressive strength that is somewhat equal for all analogues.

   However, although the two analogues with different origin temperatures are very similar in results, the -25°C analogue is still always just stronger than the -80°C analogue at vacuum pressure. The sintering of the analogues thus still has an effect on the ice analogue strength, even though its effect becomes quite small in terms of strength under vacuum. In terms of failure mode, the origin temperature has a larger effect in vacuum testing. After a certain freezer time, the -25°C analogues fail in a brittle manner, whereas the -80°C analogues do not after the same freezer time. The amount of sintering that has occurred for the analogues thus impacts their failure mode, becoming brittle if enough sintering has taken place. The effect of vacuum pressure on the ice analogues is thus a change in microstructure due to sublimation causing the shear and compressive strength to be weaker and resistant to the strengthening sintering effect in atmospheric pressure.

7.3. How does the strength of Enceladus' surface impact future landing missions?

The mechanical strength tests of the ice analogues in this study were performed to understand the strength properties of Enceladus' surface in terms of temperature, vacuum, and sintering. By translating these analogue results to Enceladus' conditions, it became evident that the surface in the SPT is mechanically weak and quite variable due to plume deposition. These plume deposits cause a porous, snow-like top layer that is unlikely to sinter significantly. Even in the warmest regions with temperatures up to 180 K, any strengthening due to sintering is likely counteracted by fresh plume deposits. This results in a top layer that remains unconsolidated and weak, as was the result of the ice analogues strength tests, which measured between 10 and 20 kPa under vacuum. Beneath this snowy top layer, partial sintering could produce a brittle ice layer as was found in the ice analogue tests.

These strength results for Enceladus' surface have direct implications for future lander missions. From the results in this study, the lander would encounter a weak snow-like top layer with a brittle ice layer underneath. To ensure stability of the lander, a few large or many small footpads and shock-absorbing legs are recommended to distribute loads and prevent brittle failure. Additionally, in-situ strength measurements after landing is recommended to confirm surface stability. Finally, the sampling methods should use low-force and thermal methods to collect the ice grains. These collected samples should then be sealed as quickly as possible to preserve the sample before too much sublimation occurs. Most important for the lander missions is thus the knowledge that the snowy top layer is weak with potentially a brittle ice layer underneath. The lander mission design should thus be able to tackle these challenges in order to land on Enceladus' surface.

7.4. Concluding the Main Research Question

Having answered each sub-research question, the main research question can be answered:

What are the mechanical properties of Enceladus' surface for the purpose of future landing missions studied through ice analogues?

This question can be answered with the following brief concluding statements:

- Enceladus has a weak and unconsolidated top layer that has a snow-like consistency due to the frequent plume deposits. In this top layer, the sintering effect of the ice grains is likely minimal due to the frequent grain deposition of the surface.
- Below the snowy top layer is likely a brittle ice layer in the SPT. The tested ice analogues have shown that if substantial sintering has occurred the ice surface becomes brittle under vacuum pressure. This is likely the case in the SPT where the surface temperature is warm enough for enough sintering to occur within a relevant timescale for landers.
- Lander missions should prepare for a weak and unconsolidated surface with a distributed low-force footpad design. Following this low-force mindset, thermal techniques can be used to anchor the lander or for sampling rather than drilling. The samples themselves should also be contained quickly to prevent too much sublimation from occurring.

The results from this study suggest that the surface conditions of Enceladus consist of a weak and unconsolidated snowy top layer underlain by a brittle ice layer. This poses multiple challenges for lander missions. A successful mission therefore requires a design that minimises mechanical stress on the surface, uses gentle anchoring and sampling methods, and accounts for potential sublimation of collected samples to ensure both landing stability and good science return.

8

Recommendations

This chapter provides recommendations for further work resulting from this thesis. First, the limitations of the experimental set-up are given. This is then followed by a list of recommendations for the experimental work performed in this thesis. Finally, a few recommendations are given to deepen the scientific understanding of the performed work, including an explanation of how they would contribute to the understanding of Enceladus.

8.1. Limitations of the Experimental Set-Up

While multiple interesting results came from this research, the used experimental set-up does have a few limitations that should be taken into account as well. These limitations, and the effect they might have on the results described in this chapter, are given here:

1. **Grain Size**
   The produced grain size in this work is up to 250 μm. This means that some grains could be smaller, but the used micro-usb camera was not be able to detect that. The average particle size around the tiger stripe region on Enceladus is 75μm with the surrounding area having an average grain size of 30 ± 10 μm to 50 ± 15 μm (Scipioni et al., 2017). The optimal grain size for the analogues is thus between 20 and 75 μm. This difference in grain size has an impact on the obtained strength from the analogues, thus using the grain size that can be found on Enceladus would be preferred. Nevertheless, many useful relations can be drawn from the results with 250 μm size grains regarding the strength of ice analogues with fine ice grains under different environments.
2. **Manual Measurements**
   While the CONE method gives good shear and compressive strength estimates using a simple method, it does have a sensitivity to human error. The cone indentation parameters are taken by eye using a ruler. Although caution is taken to accurately measure the parameters to mm accuracy, there is no way to rule out human error using the CONE method in this form.
3. **Freezer Time**
   The freezer timescale that has been used in this research is relatively short, with a maximum of 190 hours. The reason for this is the limited time available during the study. While many relevant results can be drawn from the measurements done with a maximum timescale of 190 hours, a longer timescale would give more information regarding the evolution of the ice analogues as they undergo sintering.

8.2. Experimental Recommendations

To add to the results presented in this work, several areas for further examination in future research are recommended in terms of the experimental method used for the ice analogue strength tests in this work:

8.2.1. Experimental Set-Up

The following recommendations come from the limitations of the experimental set-up described in the prior section. These recommendations would help to improve the methods used for the experimental set-up.

1. **Smaller Grain Size**
   As already explained in the limitations section, the produced ice grains in this work are larger than the ice grains expected on Enceladus' surface. Since the grain size has a big influence on the strength of an analogue, it would be incredibly relevant to develop a method at the Delft Planetary Labs to produce finer ice grains with a size of 5 μm and higher.
2. **Automatic CONE Method Measurements**
   The CONE method used in this thesis was well-suited to the test requirements: the ability to test the shear and compressive strength both in atmospheric and vacuum pressure. However, as mentioned in the limitations section as well, the strength parameters are measured by hand which introduces potential human error. It would be better if the CONE method can be adapted to remove the human error through some type of automatic measuring device as well. Ideas are to make a device that can be inserted in the cone indentation and reads off the measurements or an imaging system through which the measurements are automatically processed.

8.2.2. Ice Analogue Measurements

Although many relevant findings have come from the ice analogue measurements that have been taken, there are a few parameters that would complement these results if they would have been measured. These parameters are thus recommended for future research on this topic.

3. **Mass**
   Besides the strength measurements, the temperature, pressure, and freezer time were measured for each test. In hindsight, it would have been very useful to have mass measurements as well. Both before and after putting the analogue into the freezer as well as before and after each test. This way it would be possible to track if any mass changes occur during the freezer, but more importantly, it can be tracked how much mass loss occurs during the strength testing. This is especially relevant for the vacuum tests during which sublimation occurs where mass loss is one of its indications.
4. **Volume**
   Measuring the volume of the analogues, by measuring the height differences before and after freezer time and strength tests, could result in interesting findings as well. This measurement, combined with the mass measurement, would help especially in determining whether densification is occurring while the analogues are in the freezer which is an indication of stage 2 sintering. Volume measurements could aid in a better understanding of the behaviour of the ice analogues during testing as well.
5. **Temperature**
   For all ice analogue tests performed in this work, only one thermocouple was placed in the sample near the container wall. One of the findings was a difference in cone resistance between the inner and outer edge of the samples. The hypothesis is that this occurs because the wall provides more support to the ice grains close-by. Having temperature measurements in the middle of the sample as well would help in understanding whether this hypothesis is correct. It is not desired to place a hole in the middle of the sample however, as this is the best spot for accurate strength testing as this is where the ice grains are unconfined by the wall. Perhaps a thermocouple could be frozen with the sample, thus placing it inside of the ice analogue during the analogue production. Additional tests should be done then to ensure this thermocouple placement does not alter the strength test results.

8.2.3. Additional Tests

There are a few additional tests that can be done to have a richer understanding of the findings in this thesis. Due to time limitations these tests have not been done in this work, but they are relevant for future work on understanding Enceladus' surface properties.

6. **Analogue Strength during Sublimation**
   In this work, all vacuum strength measurements were done after the analogues had spent 20 minutes in vacuum. It would be interesting to do a series of tests after varying times spent in vacuum to see if that would have an impact on the strength results of the ice analogues. These tests would determine how the strength depends on the sublimation rate. This is relevant for building on current knowledge of Enceladus' surface as it addresses ice strength changes under vacuum conditions which would help predicting surface stability on Enceladus.
7. **Longer Sintering Timescale**
   The sintering timescale used in this work was a maximum of 200 hours. While this timescale gives interesting results, it would be nice to see the sintering and strength develop beyond the timescale of 200 hours. This would strengthen the relations found in this work. Although multiple studies have been done already on the effects of longer sintering times on the strength of ice analogues, none have been done under vacuum pressure which is highly relevant to understand the effect of sintering on Enceladus' surface strength.
8. **More Pressure Levels**
   The tests in this study were done at 1 bar and 0.1 mbar which gave interesting results, especially under vacuum pressure. It would be interesting to see a strength relation over varying pressures in between these two extremes as well. The pressure on Enceladus is near-vacuum, so the ice analogue tests in 0.1 mbar were very relevant. To better understand the behaviour and strength of ice under varying pressures, tests with more pressure levels would be valuable. Such understanding aids in further understanding of specific cases, like the fine ice grain surface of Enceladus in near-vacuum.

8.3. Scientific Recommendations

Besides the recommendations for the experimental set-up, analogue measurements, and additional tests, there are a few more scientific recommendations. The work done in this thesis, especially the ice analogue strength testing under vacuum, has not been done before. While the results from this thesis already give relevant and important findings, more research is recommended for further understanding certain aspects, such as the micro-structural behaviour of the ice or the strength of compressed ice grains.

9. **Inter-Particle Relation of the Ice Grains during Strength Testing**
   A great addition to the work performed in this thesis would be to have micro-level images of the ice grains before and after strength testing. This could be done through microscopy or spectroscopy for fine grains. This would allow visualisation of the inter-particle relations and sintering behaviour, providing insights into how these micro-structural changes affect the strength of the ice analogues. Such studies have been done already in atmospheric pressure, but not under vacuum pressure. The results could be highly relevant for further understanding Enceladus' icy grains and for lander designs for such surfaces.
10. **Low Gravity Strength Tests**
    One aspect that was not incorporated in this work is the effect of gravity. The gravity on Enceladus is $\sim 1/100$ of the gravity on Earth, which has an effect on the strength of the ice analogues. This can be incorporated in the strength results with a scaling or safety factor, but it would be very interesting and relevant to have experimental data on strength tests done in micro-gravity.
11. **Strength Tests on Compressed Ice Grains**
    A future landing mission to Enceladus will encounter a weak, unconsolidated, snowy top layer. One option to safely land is for its footpads to compress the fine ice grains until it reaches a strong and stable footing. To know how much the grains need to be compressed to reach that state, and thus how long the footpads need to be, further research should be done performing strength tests on compressed ice grain analogues.

Overall, these recommended experiments would be a great continuation of the work performed in this thesis and would provide a fuller understanding of Enceladus' surface. Studying the micro-structural behaviour of the ice grains, the effects of low gravity, and the strength of compressed ice layers would give important insights into the mechanical properties and stability of Enceladus' surface. The results would be highly relevant for future landing missions, helping to predict what a lander will encounter and how to safely land on the surface.

References

Spilker, L. (2019). Cassini-Huygens' exploration of the Saturn system: 13 years of discovery. *Science*, *364*(6445), 1046–1051.

Spencer, J. R., Pearl, J. C., Segura, M., Flasar, F. M., Mamoutkine, A., Romani, P., Buratti, B. J., Hendrix, A. R., Spilker, L. J., & Lopes, R. M. C. (2006). Cassini Encounters Enceladus: Background and the Discovery of a South Polar Hot Spot. *Science*, *311*(5766), 1401–1405.

Porco, C. C., Helfenstein, P., Thomas, P. C., Ingersoll, A. P., Wisdom, J., West, R., Neukum, G., Denk, T., Wagner, R., Roatsch, T., Kieffer, S., Turtle, E., McEwen, A., Johnson, T. V., Rathbun, J., Veverka, J., Wilson, D., Perry, J., Spitale, J., … Squyres, S. (2006). Cassini Observes the Active South Pole of Enceladus. *Science*, *311*(5766), 1393–1401.

Helbert, J., Bründl, T.-M., Haag, M., Lindner, M., Ordoubadian, B., & Wittig, S. (2025). The mission to enceladus–the esa l4 mission. *EPSC-DPS Joint Meeting 2025 (EPSC-DPS2025*, EPSC–DPS2025.

Martin, E. S., Whitten, J. L., Kattenhorn, S. A., Collins, G. C., Southworth, B. S., Wiser, L. S., & Prindle, S. (2023). Measurements of regolith thicknesses on enceladus: Uncovering the record of plume activity. *Icarus*, *392*, 115369.

Gundlach, B., Ratte, J., Blum, J., Oesert, J., & Gorb, S. (2018). Sintering and sublimation of micrometre-sized water-ice particles: The formation of surface crusts on icy solar system bodies. *Monthly Notices of the Royal Astronomical Society*, *479*(4), 5272–5287.

Molaro, J. L., Choukroun, M., Phillips, C. B., Phelps, E. S., Hodyss, R., Mitchell, K. L., Lora, J. M., & Meirion-Griffith, G. (2019). The microstructural evolution of water ice in the solar system through sintering. *Journal of Geophysical Research: Planets*, *124*(2), 243–277.

Gundlach, B., Kilias, S., Beitz, E., & Blum, J. (2011). Micrometer-sized ice particles for planetary-science experiments–i. preparation, critical rolling friction force, and specific surface energy. *Icarus*, *214*(2), 717–723.

Gundlach, B., & Blum, J. (2014). The stickiness of micrometer-sized water-ice particles. *The Astrophysical Journal*, *798*(1), 34.

Musiolik, G., & Wurm, G. (2019). Contacts of water ice in protoplanetary disks—laboratory experiments. *The Astrophysical Journal*, *873*(1), 58.

Choukroun, M., Molaro, J. L., Hodyss, R., Marteau, E., Backes, P., Carey, E. M., Dhaouadi, W., Moreland, S., & Schulson, E. M. (2020). Strength evolution of ice plume deposit analogs of enceladus and europa. *Geophysical Research Letters*, *47*(15).

Brown, R. H., Clark, R. N., Buratti, B. J., Cruikshank, D. P., Barnes, J. W., Mastrapa, R. M. E., Bauer, J., Newman, S., Momary, T., Baines, K. H., Bellucci, G., Capaccioni, F., Cerroni, P., Combes, M., Coradini, A., Drossart, P., Formisano, V., Jaumann, R., Langevin, Y., … Sotin, C. (2006). Composition and Physical Properties of Enceladus' Surface. *Science*, *311*(5766), 1425–1428.

Rhoden, A. R., Hurford, T. A., Spitale, J., Henning, W., Huff, E. M., Bland, M. T., & Sajous, S. (2020). The formation of Enceladus' Tiger Stripe Fractures from eccentricity tides. *Earth and Planetary Science Letters*, *544*, 116389.

Yin, A., & Pappalardo, R. T. (2015). Gravitational spreading, bookshelf faulting, and tectonic evolution of the South Polar Terrain of Saturn's moon Enceladus. *Icarus*, *260*, 409–439.

Park, R. S., Mastrodemos, N., Jacobson, R. A., Berne, A., Vaughan, A. T., Hemingway, D. J., Leonard, E. J., Castillo-Rogez, J. C., Cockell, C. S., Keane, J. T., Konopliv, A. S., Nimmo, F., Riedel, J. E., Simons, M., & Vance, S. (2024). The Global Shape, Gravity Field, and Libration of Enceladus. *Journal of Geophysical Research: Planets*, *129*(1).

Spencer, J. R., Barr, A. C., Esposito, L. W., Helfenstein, P., Ingersoll, A. P., Jaumann, R., McKay, C. P., Nimmo, F., & Waite, J. H. (2009). Enceladus: An Active Cryovolcanic Satellite. In M. K. Dougherty, L. W. Esposito, & S. M. Krimigis (Eds.), *Saturn from Cassini-Huygens* (pp. 683–724). Springer Netherlands.

Iess, L., Stevenson, D. J., Parisi, M., Hemingway, D., Jacobson, R. A., Lunine, J. I., Nimmo, F., Armstrong, J. W., Asmar, S. W., Ducci, M., & Tortora, P. (2014). The Gravity Field and Interior Structure of Enceladus. *Science*, *344*(6179), 78–80.

Newman, S. F., Buratti, B., Brown, R., Jaumann, R., Bauer, J., & Momary, T. (2008). Photometric and spectral analysis of the distribution of crystalline and amorphous ices on Enceladus as seen by Cassini. *Icarus*, *193*(2), 397–406.

Howett, C. J. A., Spencer, J. R., Pearl, J., & Segura, M. (2011). High heat flow from Enceladus' south polar region measured using 10–600 cm $^{-1}$ Cassini/CIRS data. *Journal of Geophysical Research*, *116*(E3).

Choblet, G., Tobie, G., Sotin, C., Běhounková, M., Čadek, O., Postberg, F., & Souček, O. (2017). Powering prolonged hydrothermal activity inside Enceladus. *Nature Astronomy*, *1*(12), 841–847.

Hemingway, D., Iess, L., Tajeddine, R., Tobie, G., et al. (2018). The interior of Enceladus. *Enceladus and the icy moons of Saturn*, 57–77.

McKinnon, W. (2015). Effect of enceladus's rapid synchronous spin on interpretation of cassini gravity. *Geophysical Research Letters*, *42*(7), 2137–2143.

Thomas, P., Tajeddine, R., Tiscareno, M., Burns, J., Joseph, J., Loredo, T., Helfenstein, P., & Porco, C. (2016). Enceladus's measured physical libration requires a global subsurface ocean. *Icarus*, *264*, 37–47.

Čadek, O., Tobie, G., Van Hoolst, T., Massé, M., Choblet, G., Lefèvre, A., Mitri, G., Baland, R.-M., Běhounková, M., Bourgeois, O., et al. (2016). Enceladus's internal ocean and ice shell constrained from cassini gravity, shape, and libration data. *Geophysical Research Letters*, *43*(11), 5653–5660.

Van Hoolst, T., Baland, R.-M., & Trinh, A. (2016). The diurnal libration and interior structure of enceladus. *Icarus*, *277*, 311–318.

Beuthe, M., Rivoldini, A., & Trinh, A. (2016). Enceladus's and dione's floating ice shells supported by minimum stress isostasy. *Geophysical Research Letters*, *43*(19), 10–088.

Waite Jr, J. H., Lewis, W. S., Magee, B. A., Lunine, J. I., McKinnon, W. B., Glein, C. R., Mousis, O., Young, D. T., Brockwell, T., Westlake, J., Nguyen, M.-J., Teolis, B. D., Niemann, H. B., McNutt Jr, R. L., Perry, M., & Ip, W.-H. (2009). Liquid water on Enceladus from observations of ammonia and 40Ar in the plume. *Nature*, *460*(7254), 487–490.

Hansen, C., Esposito, L., Colwell, J., Hendrix, A., Portyankina, G., Stewart, A., & West, R. (2020). The composition and structure of Enceladus' plume from the complete set of Cassini UVIS occultation observations. *Icarus*, *344*, 113461.

Waite, J. H., Glein, C. R., Perryman, R. S., Teolis, B. D., Magee, B. A., Miller, G., Grimes, J., Perry, M. E., Miller, K. E., Bouquet, A., Lunine, J. I., Brockwell, T., & Bolton, S. J. (2017). Cassini finds molecular hydrogen in the Enceladus plume: Evidence for hydrothermal processes. *Science*, *356*(6334), 155–159.

Glein, C. R., Postberg, F., & Vance, S. D. (2018). The geochemistry of enceladus: Composition and controls. *Enceladus and the icy moons of Saturn*, *39*.

Glein, C. R., Baross, J. A., & Waite Jr, J. H. (2015). The ph of enceladus' ocean. *Geochimica et Cosmochimica Acta*, *162*, 202–219.

Villanueva, G., Hammel, H., Milam, S., Kofman, V., Faggi, S., Glein, C., Cartwright, R., Roth, L., Hand, K., Paganini, L., et al. (2023). JWST molecular mapping and characterization of Enceladus' water plume feeding its torus. *Nature Astronomy*, 1–7.

Hansen, C. J., Esposito, L., Stewart, A. I. F., Colwell, J., Hendrix, A., Pryor, W., Shemansky, D., & West, R. (2006). Enceladus' Water Vapor Plume. *Science*, *311*(5766), 1422–1425.

Hedman, M. M., Nicholson, P. D., Showalter, M. R., Brown, R. H., Buratti, B. J., & Clark, R. N. (2009). Spectral Observations of the Enceladus Plume with Cassini-VIMS. *The Astrophysical Journal*, *693*(2), 1749–1762.

Dhingra, D., Hedman, M. M., Clark, R. N., & Nicholson, P. D. (2017). Spatially resolved near infrared observations of Enceladus' tiger stripe eruptions from Cassini VIMS. *Icarus*, *292*, 1–12.

Sharma, H., Hedman, M. M., & Vahidinia, S. (2023). New Insights into Variations in Enceladus Plume Particle Launch Velocities from Cassini-VIMS Spectral Data. *The Planetary Science Journal*, *4*(6), 108.

Hedman, M. M., Gosmeyer, C. M., Nicholson, P. D., Sotin, C., Brown, R. H., Clark, R. N., Baines, K. H., Buratti, B. J., & Showalter, M. R. (2013). An observed correlation between plume activity and tidal stresses on Enceladus. *Nature*, *500*(7461), 182–184.

Waite, J. H., Combi, M. R., Ip, W.-H., Cravens, T. E., McNutt, R. L., Kasprzak, W., Yelle, R., Luhmann, J., Niemann, H., Gell, D., Magee, B., Fletcher, G., Lunine, J., & Tseng, W.-L. (2006). Cassini Ion and Neutral Mass Spectrometer: Enceladus Plume Composition and Structure. *Science*, *311*(5766), 1419–1422.

Sakai, S., Cravens, T. E., Omidi, N., Perry, M. E., & Waite, J. H. (2016). Ion energy distributions and densities in the plume of Enceladus. *Planetary and Space Science*, *130*, 60–79.

Cravens, T. E., McNutt, R. L., Waite, J. H., Robertson, I. P., Luhmann, J. G., Kasprzak, W., & Ip, W.-H. (2009). Plume ionosphere of Enceladus as seen by the Cassini ion and neutral mass spectrometer. *Geophysical Research Letters*, *36*(8), 2009GL037811.

Postberg, F., Clark, R. N., Hansen, C. J., Coates, A. J., Dalle Ore, C. M., Scipioni, F., Hedman, M. M., & Waite, J. H. (2018). Plume and Surface Composition of Enceladus. In *Enceladus and the Icy Moons of Saturn*. The University of Arizona Press.

Postberg, F., Schmidt, J., Hillier, J., Kempf, S., & Srama, R. (2011a). A salt-water reservoir as the source of a compositionally stratified plume on Enceladus. *Nature*, *474*(7353), 620–622.

Porco, C., Dones, L., & Mitchell, C. (2017). Could It Be Snowing Microbes on Enceladus? Assessing Conditions in Its Plume and Implications for Future Missions. *Astrobiology*, *17*(9), 876–901.

Flandes, A., Mirón-Enríquez, P. E., & Ramírez-Cabañas, A. K. (2024). Geysers' dust dynamics inside the hill sphere of enceladus. *Geophysical Research Letters*, *51*(1), e2023GL105298.

Dong, Y., Hill, T., & Ye, S.-Y. (2015). Characteristics of ice grains in the enceladus plume from cassini observations. *Journal of Geophysical Research: Space Physics*, *120*(2), 915–937.

Kempf, S., Beckmann, U., & Schmidt, J. (2010). How the enceladus dust plume feeds saturn's e ring. *Icarus*, *206*(2), 446–457.

Southworth, B. S., Kempf, S., & Spitale, J. (2018). Surface deposition of the enceladus plume and the angle of emissions. *Icarus*, *319*(12).

Spitale, J. N., & Porco, C. (2007). Association of the jets of enceladus with the warmest regions on its south-polar fractures. *Nature*, *449*, 695–697.

Southworth, B. S., Kempf, S., & Spitale, J. (2019). Surface deposition of the enceladus plume and the zenith angle of emissions. *Icarus*, *319*, 33–42.

Ehrenfreund, P., Fraser, H., Blum, J., Cartwright, J., García-Ruiz, J., Hadamcik, E., Levasseur-Regourd, A., Price, S., Prodi, F., & Sarkissian, A. (2003). Physics and chemistry of icy particles in the universe: Answers from microgravity. *Planetary and Space Science*, *51*(7-8), 473–494.

Seo, M., Jang, E., Kim, K., Choi, S., & Kim, J. (2012). Understanding anisotropic growth behavior of hexagonal ice on a molecular scale: A molecular dynamics simulation study. *The Journal of chemical physics*, *137*, 154503.

Belosludov, R., Subbotin, O., Mizuseki, H., Rodger, P., Kawazoe, Y., & Belosludov, V. (2008). Crystal-like low frequency phonons in the low-density amorphous and high-density amorphous ices. *The Journal of chemical physics*, *129*, 114507.

Rosu-Finsen, A., Davies, M. B., Amon, A., Wu, H., Sella, A., Michaelides, A., & Salzmann, C. G. (2023). Medium-density amorphous ice. *Science*, *379*(6631), 474–478.

Tanaka, H., & Okabe, I. (1996). Thermodynamic stability of hexagonal and cubic ices. *Chemical physics letters*, *259*(5-6), 593–598.

Hansen, G. B., & McCord, T. B. (2004). Amorphous and crystalline ice on the Galilean satellites: A balance between thermal and radiolytic processes. *Journal of Geophysical Research: Planets*, *109*(E1), 2003JE002149.

Finney, J. L., Bowron, D. T., Soper, A. K., Loerting, T., Mayer, E., & Hallbrucker, A. (2002). Structure of a New Dense Amorphous Ice. *Physical Review Letters*, *89*(20), 205503.

Salzmann, C. G. (2019). Advances in the experimental exploration of water's phase diagram. *The Journal of Chemical Physics*, *150*(6), 060901.

Stern, J., & Loerting, T. (2017). Crystallisation of the amorphous ices in the intermediate pressure regime. *Scientific Reports*, *7*(1), 3995.

Hemley, R. J., Chen, L. C., & Mao, H. K. (1989). New transformations between crystalline and amorphous ice. *Nature*, *338*(6217), 638–640.

Loerting, T., Schustereder, W., Winkel, K., Salzmann, C. G., Kohl, I., & Mayer, E. (2006). Amorphous Ice: Stepwise Formation of Very-High-Density Amorphous Ice from Low-Density Amorphous Ice at 125 K. *Physical Review Letters*, *96*(2), 025702.

Loerting, T., Bauer, M., Kohl, I., Watschinger, K., Winkel, K., & Mayer, E. (2011). Cryoflotation: Densities of Amorphous and Crystalline Ices. *The Journal of Physical Chemistry B*, *115*(48), 14167–14175.

Jenniskens, P., & Blake, D. (1996). Crystallization of amorphous water ice in the solar system. *The Astrophysical Journal*, *473*, 1104–1113.

Gómez, P., Satorre Aznar, M., & Escribano, R. (2020). Density and porosity of amorphous water ice by DFT methods. *Chemical Physics Letters*, *745*, 137222.

Iriarte-Carretero, I., Gonzalez, M. A., & Bresme, F. (2018). Thermal conductivity of ice polymorphs: A computational study. *Physical Chemistry Chemical Physics*, *20*(16), 11028–11036.

Andersson, O., & Inaba, A. (2005). Thermal conductivity of crystalline and amorphous ices and its implications on amorphization and glassy water. *Physical Chemistry Chemical Physics*, *7*(7), 1441.

Petrovic, J. J. (2003). Review Mechanical properties of ice and snow. *Journal of Materials Science*, *38*, 1–6.

Arakawa, M., & Maeno, N. (1997). Mechanical strength of polycrystalline ice under uniaxial compression. *Cold Regions Science and Technology*, *26*(3), 215–229.

Cao, P., Wu, J., Zhang, Z., Fang, B., Peng, L., Li, T., Vlugt, T. J. H., & Ning, F. (2018). Mechanical properties of bi- and poly-crystalline ice. *AIP Advances*, *8*(12), 125108.

Hessinger, J., White, B., & Pohl, R. (1996). Elastic properties of amorphous and crystalline ice films. *Planetary and Space Sciences*, *44*(9), 937–944.

Gold, L. (1988). On the elasticity of ice plates. *Canadian Journal of Civil Engineering*, *15*(6), 1080–1084.

Palanque, V., Villeneuve, E., Budinger, M., Pommier-Budinger, V., & Momen, G. (2023). Experimental measurement and expression of atmospheric ice Young's modulus according to its density. *Cold Regions Science and Technology*, *212*, 103890.

Schulson, E. (1999). The Structure and Mechanical Behavior of Ice. *JOM*, *51*(2), 21–27.

Schulson, E., & Renshaw, C. (2022). Fracture, Friction, and Permeability of Ice. *Annual Review of Earth and Planetary Sciences*, *50*, 323–343.

Leonard, E. J., Yin, A., & Pappalardo, R. T. (2017). Constraining the Viscosity OF Enceladus's Ice Shell through the Crater. *Lunar and Planetary Science*, *48*.

Weertman, J. (1983). Creep deformation of ice. *Annual Review of Earth and Planetary Sciences*, *11*, 215–240.

O'Callaghan, J. (2023). Scientists made a new kind of ice that might exist on distant moons. *Nature*, *614*, 396–397.

Ostro, S. J., West, R. D., Janssen, M. A., Lorenz, R. D., Zebker, H. A., Black, G. J., Lunine, J. I., Wye, L. C., Lopes, R. M., Wall, S. D., Elachi, C., Roth, L., Hensley, S., Kelleher, K., Hamilton, G. A., Gim, Y., Anderson, Y. Z., Boehmer, R. A., & Johnson, W. T. (2006). Cassini RADAR observations of Enceladus, Tethys, Dione, Rhea, Iapetus, Hyperion, and Phoebe. *Icarus*, *183*(2), 479–490.

Jaumann, R., Stephan, K., Hansen, G., Clark, R., Buratti, B., Brown, R., Baines, K., Newman, S., Bellucci, G., Filacchione, G., Coradini, A., Cruikshank, D., Griffith, C., Hibbitts, C., McCord, T., Nelson, R., Nicholson, P., Sotin, C., & Wagner, R. (2008). Distribution of icy particles across Enceladus' surface as derived from Cassini-VIMS measurements. *Icarus*, *193*(2), 407–419.

McKinnon, W. B., Lunine, J. I., Mousis, O., Waite, J. H., & Zolotov, M. Y. (2018). The mysterious origin of Enceladus: A compositional perspective. *Enceladus and the Icy Moons of Saturn*, 17.

Blackford, J. R. (2007). Sintering and microstructure of ice: A review. *Journal of Physics D: Applied Physics*, *40*(21), 355–385.

Hobbs, P. (1974). *Ice physics*. Oxford University Press.

Kabore, B., & Peters, B. (2020). Micromechanical model for sintering and damage in viscoelastic porous ice and snow. part i: Model and calibration. *International Journal of Solids and Structures*, *185-186*, 324–333.

Kang, S.-J. L. (2004). *Sintering: Densification, grain growth and microstructure*. Elsevier.

Dhaouadi, W., Marteau, E., Kolvenbach, H., Choukroun, M., Molaro, J. L., Hodyss, R., & Schulson, E. M. (2022). Discrete element modeling of planetary ice analogs: Mechanical behavior upon sintering. *Granular Matter*, *24*, 1–20.

Swinkels, F., & Ashby, M. (1981). A second report on sintering diagrams. *Acta Metallurgica*, *29*(2), 259–281.

Labuz, J., & Zang, A. (2012). Mohr-coulomb failure criterion. *Rock Mechanics and Rock Engineering*, *45*, 975–979.

Watson, P., Suemasa, N., & Randolph, M. (2000). Evaluating undrained shear strength using the vane shear apparatus. *International Ocean and Polar Engineering Conference*, *2*, 485–493.

Verwaal, W., & Mulder, A. (2017). *Soil mechanics laboratory manual*. Delft University of Technology.

Mantovani, J. G., Galloway, G. M., & Zacny, K. (2016). ASCE Earth and Space Conference April, 2016 – Orlando, FL.

Zacny, K., Wilson, J., Craft, J., Asnani, V., Oravec, H., Creager, C., Johnson, J., & Fong, T. (2010). Robotic Lunar Geotechnical Tool. *Earth and Space 2010*, 166–181.

McCallum, A. (2014a). Cone penetration testing (CPT) in Antarctic firn: An introduction to interpretation. *Journal of Glaciology*, *60*(219), 83–93.

Whiteley, G., & Dexter, A. (1981). The dependence of soil penetrometer pressure on penetrometer size. *Journal of Agricultural Engineering Research*, *26*(6), 467–476.

Harmon, J. M., Cable, M. L., Moreland, S. J., & Andrade, J. E. (2023). Predicting the effect of surface properties on enceladus for landing. *The Planetary Science Journal*, *4*(8), 150.

Jabaud, B., Artoni, R., Tobie, G., Le Menn, E., & Richard, P. (2024). Cohesive properties of ice powders analogous to fresh plume deposits on enceladus and europa. *Icarus*, *409*, 115859.

Poch, O., Pommerol, A., Jost, B., Carrasco, N., Szopa, C., & Thomas, N. (2016). Sublimation of water ice mixed with silicates and tholins: Evolution of surface texture and reflectance spectra, with implications for comets. *Icarus*, *267*, 154–173.

Ganneau, F., Constantinides, G., & Ulm, F.-J. (2006). Dual-indentation technique for the assessment of strength properties of cohesive-frictional materials. *International journal of solids and structures*, *43*(6), 1727–1745.

Zein, A. K. M. (2017). Estimation of undrained shear strength of fine grained soils from cone penetration resistance. *International Journal of Geo-Engineering*, *8*(1), 9.

Ma, Q.-y., Ma, D.-d., Yuan, P., & Yao, Z.-m. (2018). Energy absorption characteristics of frozen soil based on shpb test. *Advances in Materials Science and Engineering*, *2018*(1).

Kim, S. Y., & Lee, J.-S. (2020). Estimation of shear strength and shear wave velocity for frozen soils with various silt fractions. In *Transportation soil engineering in cold regions, volume 1: Proceedings of transoilcold 2019* (pp. 157–162). Springer.

Parameswaran, V. (1978). Adfreeze strength of frozen sand to model piles. *Canadian geotechnical journal*, *15*(4), 494–500.

Parameswaran, V. (1980). Deformation behaviour and strength of frozen sand. *Canadian Geotechnical Journal*, *17*(1), 74–88.

McCallum, A. (2014b). A brief introduction to cone penetration testing (cpt) in frozen geomaterials. *Annals of Glaciology*, *55*(68), 7–14.

Parameswaran, V., & Jones, S. (1981). Triaxial testing of frozen sand. *Journal of Glaciology*, *27*(95), 147–155.

Mayne, P. (2007). *Nchrp synthesis 368: Cone penetration testing (chapter 5: Cone penetration testing data presentation and geostratigraphy)*. Transportation Research Board.

Frederking, R. M. W., Svec, O. J., & Timco, G. W. (1988). *On measuring the shear strength of ice*. National Research Council Canada, Institute for Research in Construction.

Wexler, A. (1977). Vapor pressure formulation for ice. *Journal of Research of the National Bureau of Standards. Section A, Physics and Chemistry*, *81*(1), 5.

Boinovich, L., & Emelyanenko, A. (2014). Experimental determination of the surface energy of polycrystalline ice. *Doklady Physical Chemistry*, *459*(2), 198–202.

Thomsen, F., Hofmann, G., Ebel, T., & Willumeit-Römer, R. (2018). An elementary simulation model for neck growth and shrinkage during solid phase sintering. *Materialia*, *3*, 338–346.

Kossacki, K. J., Markiewicz, W. J., Skorov, Y., & Kömle, N. I. (1999). Sublimation coefficient of water ice under simulated cometary-like conditions. *Planetary and Space Science*, *47*(12), 1521–1530.

Luna, R., Satorre, M., Santonja, C., & Domingo, M. (2014). New experimental sublimation energy measurements for some relevant astrophysical ices. *Astronomy & Astrophysics*, *566*, A27.

Morin, S., Bittner, A., & Cascajo, M. (2021). The ice-vapor interface during growth and sublimation, 1–28.

Schulson, E. (1979). An analysis of the brittle to ductile transition in polycrystalline ice under tension. *Cold Regions Science and Technology*, *1*(2), 87–91.

Sola, A., & Trinchi, A. (2023). Chapter 10—fused deposition modeling of fully inorganic parts: Shaping, debinding, and sintering (sds). *Fused Deposition Modeling of Composite Materials; Sola, A., Trinchi, A., Eds*, 249–289.

Scipioni, F., Schenk, P., Tosi, F., D'Aversa, E., Clark, R., Combe, J.-P., & Dalle Ore, C. (2017). Deciphering sub-micron ice particles on enceladus surface. *Icarus*, *290*, 183–200.

Wang, E., Fu, X., Han, H., Liu, X., Xiao, Y., & Leng, Y. (2021). Study on the mechanical properties of compacted snow under uniaxial compression and analysis of influencing factors. *Cold Regions Science and Technology*, *182*, 103215.

A

Test Plans

This appendix contains the test plans for all tests that have been done throughout the thesis. This includes the test plans for each aspect of the particle production procedure, the validation of the used control material, the evaluation of the test method, the atmospheric shear and compressive strength tests, and the vacuum shear and compressive strength tests.

A.1. Test Plans for Particle Production

Table A.1: Test Plan: Particle Production - Scooping

Particle Production – Scooping **Experiment ID**: Scoop-d	
Test Description	Test the effects of scoop intervals on the formation of particles (size, clumping, etc.)
Goal	Determine the optimal scooping interval to create fine ice grains.
Required Equipment	Tools used to perform the test: • Dewar with LN_2 • Metal container / Dewar • Scoop • Sprayer • Sieve • Camera

Procedure	Using a constant spraying speed and spraying type (note down):
	1. Scoop at intervals of 5s, 10s, 15s, 20s, 25s, 30s
	2. For each interval:
	  • Take photo of particles
	  • Measure minimum, maximum, and average particle diameter (d)
	  • Note the amount of clumping

Notes	Do three attempts with varying constants to assess repeatability.

Table A.2: Test Plan: Particle Production - Spraying Speed

Particle Production – Spraying Speed **Experiment ID**: V_Spray – d	
Test Description	Test the effects of spraying speed on the forming of particles (size, clumping, etc.)
Goal	Determine the optimal speed of spraying water into the LN_2 dewar to create fine ice grains.
Required Equipment	Tools used to perform the test: • Dewar with LN_2 • Metal container / Dewar • Scoop • Sprayer • Sieve • Camera

Procedure	Using a constant scooping interval and spraying type (note down):
	1. Spray at 10x/15s, 15x/15s, and 20x/15s
	2. For each interval:
	  • Take photo of particles
	  • Measure minimum, maximum, and average particle diameter (d)
	  • Note the amount of clumping

Notes	Do three attempts with varying constants to assess repeatability.

Table A.3: Test Plan: Particle Production - Spraying Type

Particle Production – Spraying Type **Experiment ID**: Type_Spray	
Test Description	Test the effects of spraying types (mist / eject-like) on the forming of particles (size, clumping, etc.)
Goal	Determine the optimal spraying method to create fine ice grains.
Required Equipment	Tools used to perform the test: • Dewar with LN_2 • Metal container / Dewar • Scoop • Sprayer • Sieve • Camera
Procedure	Using a constant scooping interval and spraying speed (note down): 1. Spray using mist and eject-like spray settings 2. For each interval: • Take photo of particles • Measure minimum, maximum, and average particle diameter (d) • Note the amount of clumping
Notes	Do three attempts with varying constants to assess repeatability.

Table A.4: Test Plan: Particle Production

Particle Production **Experiment ID**: Particle-d	
Test Description	Test the combined effects of scoop intervals, spraying speed, and spraying types.
Goal	Determine the optimal method to create fine ice grains.
Required Equipment	Tools used to perform the test: • Dewar with LN_2 • Metal container / Dewar • Scoop • Sprayer • Sieve • Camera
Procedure	Using the knowledge gained in the prior three tests: 1. Use the optimal settings for spraying speed, spraying type, and scooping intervals 2. Take photo of particles, measure the size, and note the amount of clamping
Notes	Do three attempts with varying constants to assess repeatability.

A.2. Control Material Validation

Table A.5: Test Plan: Control Material Validation - Pocket Shear Vane

Control Material Validation - Pocket Shear Vane **Experiment ID**: Pocket_Shear	
Test Description	Measure the shear strength of frozen quartz sand using a pocket shear vane instrument.
Goal	Determine the shear strength of the frozen quartz sand samples for validation of the manually constructed fall cone device
Required Equipment	Tools used to perform the test: • Container with frozen quartz sand • Pocket shear vane instrument • Thermocouple • Freezer
Procedure	1. Place the vanes of the pocket shear vane into the sample until the vanes are fully submerged 2. Twist the pocket shear vane until failure occurs 3. Measure the shear strength on top of the pocket shear vane
Notes	-

Table A.6: Test Plan: Control Material Validation - Pocket Penetrometer

Control Material Validation - Pocket Penetrometer **Experiment ID**: Pocket_Compression	
Test Description	Measure the compressive strength of frozen quartz sand using a pocket penetrometer.
Goal	Determine the compressive strength of the frozen quartz sand samples for validation of the manually constructed fall cone device
Required Equipment	Tools used to perform the test: • Container with frozen quartz sand • Pocket penetrometer • Thermocouple • Freezer
Procedure	1. Place the pocket penetrometer onto the sample 2. Push gradually with the pocket penetromter until failure occurs 3. Read off the compressive strength on the pocket penetrometer
Notes	-

A.3. Evaluation of Test Method

Table A.7: Test Plan: Evaluation Test Method - DIY Sand

Evaluation of Test Method - DIY Sand **Experiment ID**: DIY_Sand	
Test Description	Measure the shear and compressive strength of frozen quartz sand using the manually constructed fall cone instrument.
Goal	Determine the shear and compressive strength of the frozen quartz sand samples using the manually constructed fall cone device.
Required Equipment	Tools used to perform the test: • Container with frozen quartz sand • 10 cm tube • Cone • Thermocouple • Freezer
Procedure	1. Place the thermocouple into the frozen quartz sand sample 2. Drop the cone through the tube onto the sample 3. Measure the D and d_s parameters of the indent 4. Repeat steps #2 and #3 until there is no space left to take measurements 5. Calculate the shear and compressive strength using the measured parameters
Notes	-

Evaluation of Test Method - Tube test	
Experiment ID: Tube	
Test description	Determine the optimal tube height for strength measurements using the CONE method
Goal	Find the optimal tube height
Required equipment	- 5, 10, and 15 cm tube - Cone - Thermocouple - Freezer - Quartz sand - Container
Procedure	1. Place the thermocouple into the frozen quartz sand sample 2. Drop the cone through the first tube onto the sample 3. Measure the D and d_s parameters 4. Inspect visually how the sample failed 5. Repeat steps 2 to 4 for each tube height 6. Calculate the shear and compressive strength using the measured parameters
Notes	-

Table A.8: Test Plan: Evaluation Test Method - Tube test

A.4. Atmospheric and Vacuum Tests

Atmospheric Tests	
Experiment ID: ATM	
Test description	Perform the CONE test on the ice analogues in atmospheric pressure
Goal	Determine the shear and compressive strength of the ice analogues in atmospheric pressure
Required equipment	- 10 cm tube - Cone - Thermocouple - Freezer - Ice analogue
Procedure	1. Place the thermocouple into the ice analogue 2. Drop the cone through the tube onto the sample 3. Measure the D and d_s parameters 4. Repeat steps 2 and 3 until no more measurements can be taken 5. Calculate the shear and compressive strength using the measured parameters
Notes	-

Table A.9: Test Plan: Atmospheric Tests

Vacuum Tests	
Experiment ID: VAC	
Test description	Perform the CONE test on the ice analogues in the vacuum chamber using a magnetic release system to drop the cone
Goal	Determine the shear and compressive strength of the ice analogues in vacuum pressure
Required equipment	- 10 cm tube - Cone - Thermocouple - Magnet - Vacuum chamber - Freezer - Ice analogue - Liquid nitrogen - Two tripods to hold the tube and ice analogue
Procedure	1. Place the thermocouple into the ice analogue 2. Place the ice analogue onto the tripod in the vacuum chamber 3. Pump down the vacuum chamber 4. Add liquid nitrogen in the cold finger 5. Once the lowest pressure has been reached, drop the cone by removing the magnet 6. Drop the cone through the tube onto the sample 7. Vent the vacuum chamber 8. Measure the D and d_s parameters 9. Repeat steps 2 to 7 two more times 10. Calculate the shear and compressive strength using the measured parameters
Notes	-

Table A.10: Test Plan: Vacuum Tests

B

Control Material Validation Tests

B.1. Shear Strength

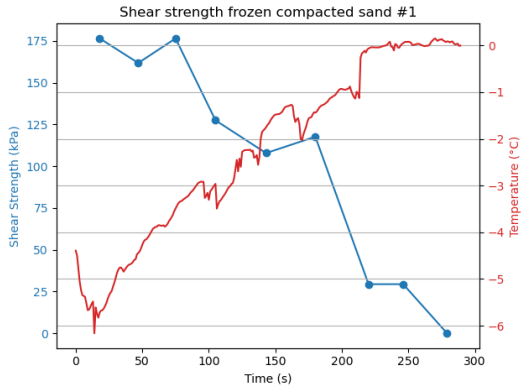

Figure B.1: Shear strength of frozen compacted quartz sand with temperature against time, test #1.

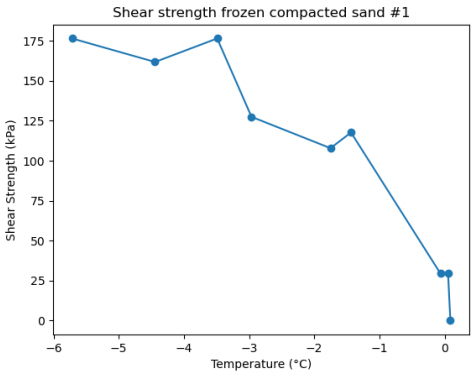

Figure B.2: Shear strength of frozen compacted quartz sand against temperature, test #1.

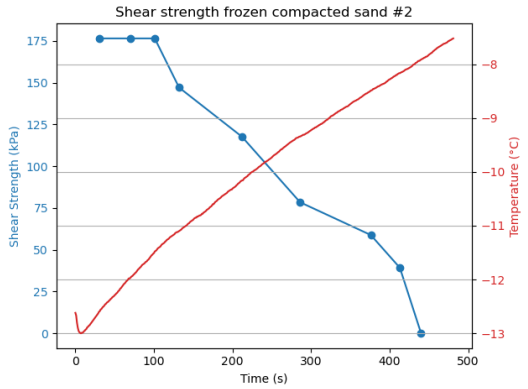

Figure B.3: Shear strength of frozen compacted quartz sand with temperature against time, test #2.

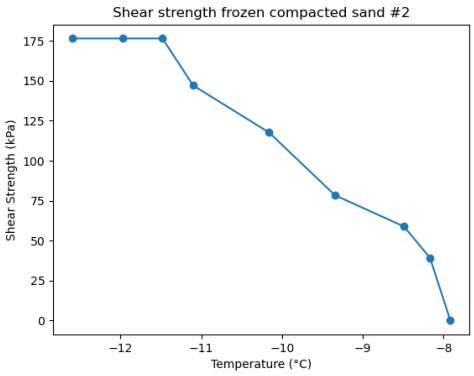

Figure B.4: Shear strength of frozen compacted quartz sand against temperature, test #2.

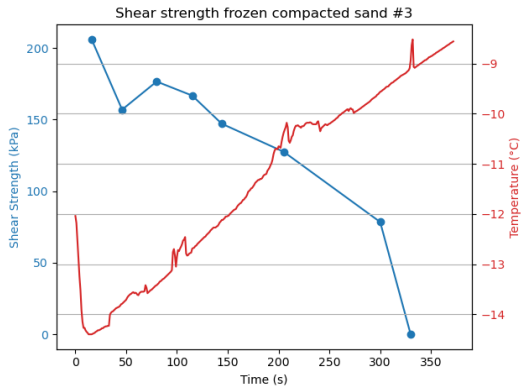

Figure B.5: Shear strength of frozen compacted quartz sand with temperature against time, test #3.

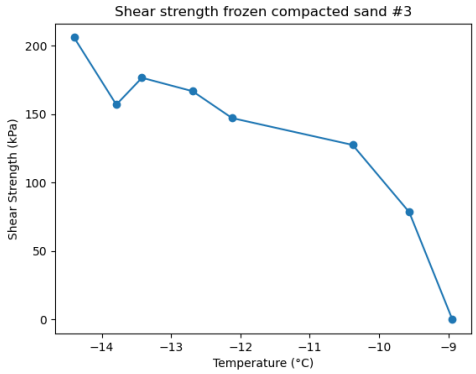

Figure B.6: Shear strength of frozen compacted quartz sand against temperature, test #3.

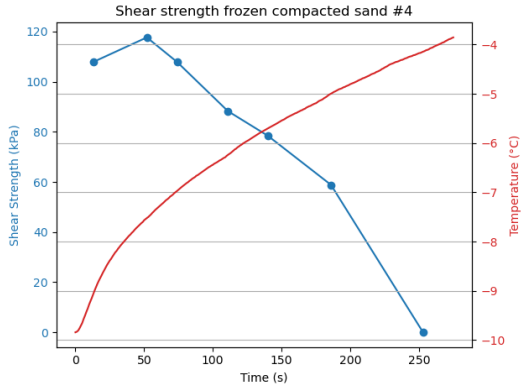

Figure B.7: Shear strength of frozen compacted quartz sand with temperature against time, test #4.

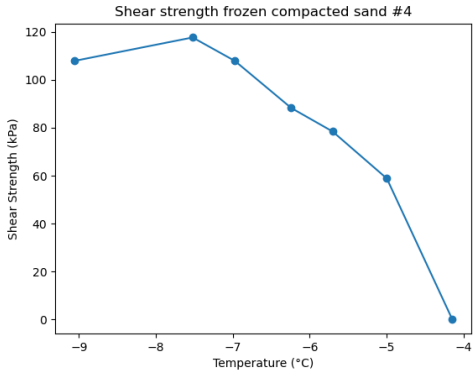

Figure B.8: Shear strength of frozen compacted quartz sand against temperature, test #4.

B.2. Compressive Strength

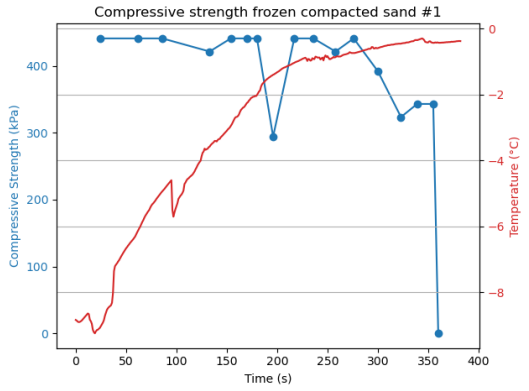

Figure B.9: Compressive strength of frozen compacted quartz sand with temperature against time, test #1.

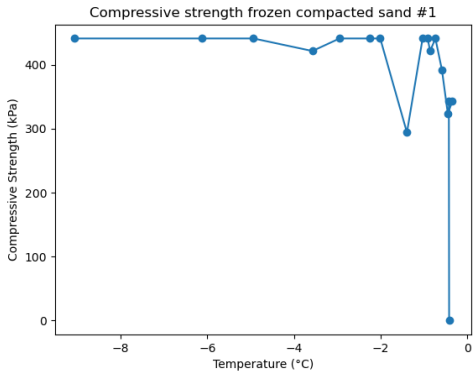

Figure B.10: Compressive strength of frozen compacted quartz sand against temperature, test #1.

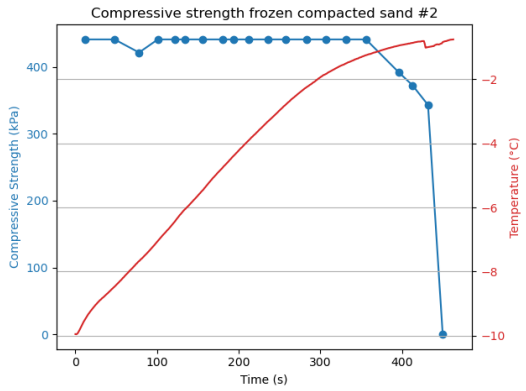

Figure B.11: Compressive strength of frozen compacted quartz sand with temperature against time, test #2.

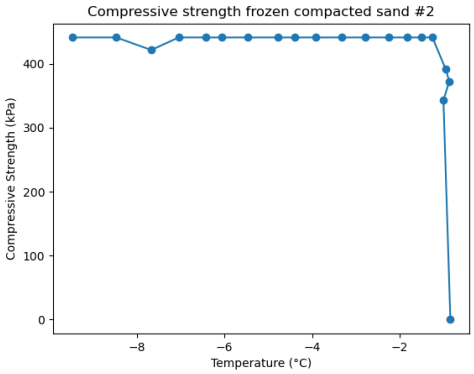

Figure B.12: Compressive strength of frozen compacted quartz sand against temperature, test #2.

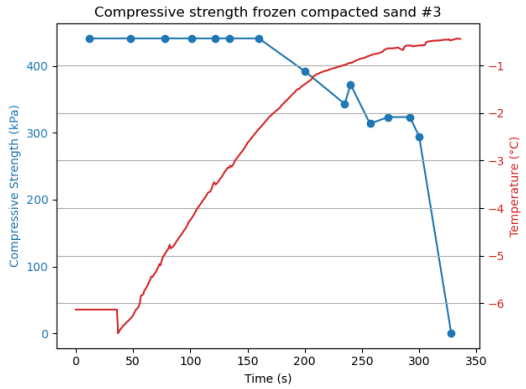

Figure B.13: Compressive strength of frozen compacted quartz sand with temperature against time, test #3.

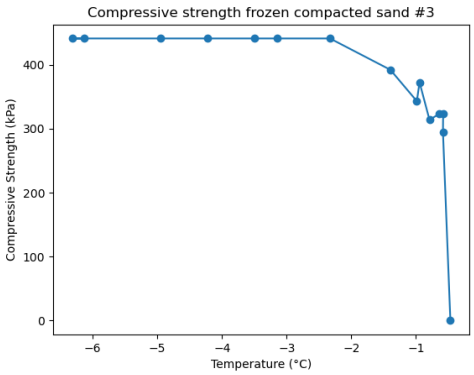

Figure B.14: Compressive strength of frozen compacted quartz sand against temperature, test #3.

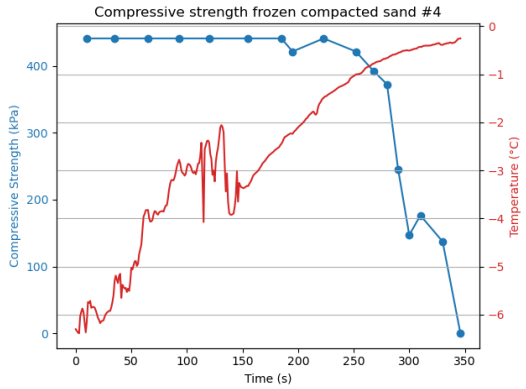

Figure B.15: Compressive strength of frozen compacted quartz sand with temperature against time, test #4.

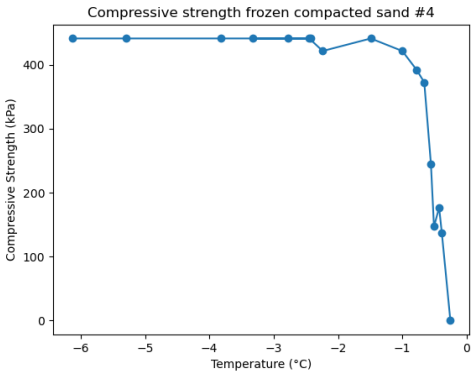

Figure B.16: Compressive strength of frozen compacted quartz sand against temperature, test #4.

C

Logbook

C.1. CONE measurements for T = -25 °C in p = 1 bar

#Experimentnummer	Metingnummer	Vriezertijd	d_s	D
1	1	5	17	18
1	2	5	17	19
1	3	5	19	22
2	1	9	17	16
2	2	9	18	21
2	3	9	17	18
2	4	9	16	18
3	1	27	14	11
3	2	27	14.5	11.5
3	3	27	9.5	9.5
3	4	27	11.5	11
3	5	27	12	11.5
3	6	27	14	12.5
3	7	27	11	11
3	8	27	12.5	11.5
4	1	47	9.5	9
4	2	47	11	10.5
4	3	47	9.5	10.5
4	4	47	11.5	10.5
4	5	47	12.5	13.5
4	6	47	12	12
4	7	47	11.5	10
4	8	47	11	11.5
5	1	92	11	11
5	2	92	12	12
5	3	92	9	10
5	4	92	8	8.5
5	5	92	10.5	11.5
5	6	92	9	8
5	7	92	11.5	11
5	8	92	9.5	11

Figure C.1: CONE measurements for T = -25 °C in p = 1 bar

#Experimentnumme	Metingnummer	Vriezertijd	d_s	D
6	1	140	11	12
6	2	140	10.5	11
6	3	140	11	12
6	4	140	10	11
6	5	140	11	11
6	6	140	9	10
6	7	140	10	11
7	1	168	8	11
7	2	168	9	11
7	3	168	11	11.5
7	4	168	7.5	11
7	5	168	7	10
7	6	168	9	11
7	7	168	9.5	10.5
7	8	168	11	12
8	1	192	9	7.5
8	2	192	8.5	12
8	3	192	11	9
8	4	192	9	8
8	5	192	10	10.5
8	6	192	7	6
8	7	192	7.5	7
8	8	192	9.5	9

Figure C.2: CONE measurements for T = -25 °C in p = 1 bar

C.2. CONE measurements for T = -80 °C in p = 1 bar

#Experimentnummer	Metingnummer	Vriezertijd	d_s	D
1	1	142	11.5	15
1	2	142	7	9
1	3	142	13	13
1	4	142	14	15
1	5	142	6.5	5.5
1	6	142	13	14
1	7	142	7	5.5
2	1	20	11	12
2	2	20	13	17
2	3	20	9.5	11
2	4	20	14	12.5
2	5	20	12	12
2	6	20	13	13.5
2	7	20	10.5	12
3	1	27	12	17
3	2	27	13.5	15.5
3	3	27	13	14
3	4	27	11	16.5
3	5	27	15	17

Figure C.3: CONE measurements for T = -80 °C in p = 1 bar

#Experimentnummer	Metingnummer	Vriezertijd	d_s	D
4	1	93	10	12
4	2	93	12	12.5
4	3	93	11	12
4	4	93	9.5	12
5	1	46	14	11
5	2	46	14	13
5	3	46	16	14
5	4	46	14	15
6	1	164	17	19
6	2	164	19	20
6	3	164	18	18
6	4	164	20	21
7	1	195	11	19
7	2	195	9	13
7	3	195	8	13
7	4	195	12	17

Figure C.4: CONE measurements for T = -80 °C in p = 1 bar

C.3. CONE measurements for T = -25 °C in p = 0.1 mbar

#Experimentnummer	Metingnummer	Vriezertijd	d_s	D
1	1	114	16.5	21
1	2	114	13.5	14.5
1	3	114	18	20
2	1	25	19	20
2	2	25	17	19.5
2	3	25	18	19.5
3	1	16	19	21
3	2	16	16	19
3	3	16	17.5	20
4	1	146	17	21
4	2	146	18	21
4	3	146	19	19
5	1	190	16	18
5	2	190	14	16
5	3	190	16	17
6	1	70	16	18
6	2	70	15	17
6	3	70	14	16

Figure C.5: CONE measurements for T = -25 °C in p = 0.1 mbar

C.4. CONE measurements for T = -80 °C in p = 0.1 mbar

#Experimentnummer	Metingnummer	Vriezertijd	d_s	D
1	1	113	19	22
1	2	113	17.5	22
1	3	113	18	22
2	1	26	23	21
2	2	26	17	19.5
2	3	26	19.5	22
3	1	15	20	21
3	2	15	21	21
3	3	15	22	20
4	1	146	23	22
4	2	146	21	22
4	3	146	21	19
5	1	190	19	19
5	2	190	18	21
5	3	190	18	19
6	1	70	18	22
6	2	70	18	20
6	3	70	19	18

Figure C.6: CONE measurements for T = -80 °C in p = 0.1 mbar